Size Effect in Polymeric Materials: the Origins and the Multi-physics Responses in Ultrasound Fields

Kaiyuan Peng

Dissertation submitted to the Faculty of the
Virginia Polytechnic Institute and State University
in partial fulfillment of the requirements for the degree of

Doctor of Philosophy
in
Mechanical Engineering

Reza Mirzaeifar, Chair
Amrinder Nain
Pinar Acar
Shima Shahab
David L. Safranski

December 10, 2020
Blacksburg, Virginia

Keywords: Size effect, Polymeric materials, Finite element analysis, Molecular dynamics simulation, Thermo-mechanical responses, Ultrasonic fields

Size Effect in Polymeric Materials: the Origins and the Multi-physics Responses in Ultrasound Fields

Kaiyuan Peng

(ABSTRACT)

The size effect in the thermo-mechanical behavior of polymeric materials is a critically important phenomenon and has been the subject of many researches in past decades. For example, polystyrene (PS), a widely used polymeric material, is brittle at the bulk state. When the dimensions decreases to the nanoscale, such as PS in nanofibers, their ductility becomes orders higher than their bulk state. In recent years a number of diverse applications, such as scaffolds in tissue engineering, drug delivery devices, as well as soft robotics, are designed by utilizing the unique properties of polymers at nanoscale. However, the inside mechanism of the size dependency in polymeric materials are still not clear yet. In this dissertation, systematic computational and experimental studies are made in order to understand the origins of the size effect for one- and two-dimensional polymeric materials. This framework is also expanded to investigate the size-dependent multi-physics response of functional polymeric materials (shape memory polymers) which are actuated by high-intensity focused ultrasound (HIFU). Our computational studies are based on molecular dynamic (MD) simulations at the atomistic scale, and experimentally-validated finite element models at the bulk level. From bottom-up direction, molecular dynamics can reveal the mechanisms of the size effect in polymers at molecular level, and help predict properties of the bulk materials. In this research, MD simulations are performed to track the origins of the size-effect in the mechanical properties of PE and PS nanofibers. In addition, the size-dependent thermal response of functional polymeric films is also studied at the atomistic scale by utilizing molecular

dynamics simulations to predict the thermal properties and actuation mechanisms in these materials when subjected to HIFU fields. From top-down direction, experiments and finite element analysis, are also conducted in this research. An experimentally-validated finite element framework is built to study the mechanical response of shape memory polymers (SMPs) triggered by HIFU. As an external trail towards application fields, a SMP composite with enhanced shape memory ability and also a two-way SMP are synthesized. A smart gripper and also a self-rolling structure are designed by using these SMPs, which approves that these SMPs are good components in designing soft robotics. Finally, The influence of evaporation during fiber forming process is investigated by molecular dynamics simulation. It is found that the formation of the microstructure of polymeric fibers at nanoscale depends on the balance of stretching force and evaporation rate when the fiber is forming.

Size Effect in Polymeric Materials: the Origins and the Multi-physics Responses in Ultrasound Fields

Kaiyuan Peng

(GENERAL AUDIENCE ABSTRACT)

Thermomechanical properties of a thin fiber, a thin film and a cube made of a polymer are significantly different. Although, based on the extensive research that has been performed in recent years our understanding of this size-dependency is advanced to a great degree in the past decades, there are still many unanswered basic questions that can only be addressed by performing computational and experimental investigation at different length scales, from atomistic up to bulk level in polymers. In this research we target exploring some unknown aspects of the size dependency in the thermomechanical properties of polymers by investigating their deformation mechanisms at different length scales. As the first step, we will investigate the mechanical properties of polymeric fibers. For these fibers, the mechanical properties are strongly connected to the fiber's diameter. The prevailing hypothesis is that this size dependency is closely related to the thickness of the surface layer of the nanofibers. Our results show some unknown origins behind the size dependency of the mechanical properties in polyethylene (PE) and polystyrene (PS) nanofibers, which originate from the deformation mechanisms at the atomistic scale. In addition, not just the mechanical properties, the thermal properties and response of functional polymers subjected to an external stimulation are also related to their size. For example, the thermal conductivity of a fiber, a sheet and a cube may be significantly different. Our study shows the thermal responses of different polymers triggered by ultrasound are also different. The size and the type of the polymers will both have influence on the final temperature in the polymeric materials, when the polymeric

materials are heated by same ultrasound source. We also have applied our computational and experimental frameworks to investigate this phenomenon. In addition, we also used a new shape memory polymer composite and a two-way shape memory polymer on designing soft robotics-like structures. Overall this research indicates that both mechanical response and thermal responses of polymers are highly related to their dimension. Taking advantage of these unique size effects, and by tailoring this property, diverse devices can be made for being used in a broad range of applications.

Dedication

To my parents for always loving and supporting me.

Acknowledgments

There are many thanks for people I meet in Virginia Tech who have ever guided, inspired or helped me. I apologize for that I cannot mention everyone. However, I would express my sincerest thanks for the people who bring me to this point that I am able to write this dissertation and earn my PhD degree here.

First and most importantly, I want to thank my advisor, Dr. Reza Mirzaeifar who help me grow to a better researcher from a freshmen in the academic journey. With his patient and meticulous guidance in all aspects, I am able to become not only a better graduate in professional fields, but also a better man for being enthusiastic and curious to all the interesting things in the daily life. Because of his great planning for my academic study since four years ago when I just joined the group, I am able to have a good work and life balance, and always be in a good mood during research time. His open door policy makes me can ask almost any questions, even it is very tiny or primitive sometimes, at almost any time. His amiable guidance make me not be afraid of failure, and always have a creative attitude towards challenges.

Next, I want to thank all my committee members: Dr. Amrinder Nain, Dr. Pinar Acar, Dr. Shima Shahab and Dr. David Safranski. I had many lengthy discussions with Dr. Nain who gave me many valuable suggestions. I enjoyed working with Dr. Shahab and her group's members who were always very kind and patient to me. I thank Dr. Acar and Dr. Safranski for their insightful advice and helpful suggestions on this dissertation.

I also want to thank all my labmates: Fatemeh, Mohamad, Sachin, Matthew, Yao, Ryan, Arpit, Jonathan, Juanita, Jiaxin and Ravi. They always spared no effort to help me when I face difficulties. A special thank to Ryan and Yao who helped me on technique writing a lot.

Financial support from the NSF CMMI grant 2016474 is gratefully acknowledged.

Last but not the least, I thank my parents, Daisheng Peng and Xiaoling Yang, for their selfless love and constant encouragement. Having their companionship is the sweetest thing in my life.

Contents

List of Figures

List of Tables

List of Abbreviations

ϵ The strain

μ_a The shear modulus of the amorphous phase

μ_g The shear modulus of the glassy phase

Ψ_a The stored energy for the amorphous phase

Ψ_g The stored energy for the glassy phase

σ The stress

F_{k_a} The deformation gradient in amorphous state

F_{k_g} The deformation gradient in glassy state

HDPE High density polyethylene

HIFU High intensity focused Ultrasound

KZK equation Khokhlov-Zabolotskaya-Kuznetsov equation

LDPE Low density polyethylene

MD Molecular dynamics

PS Polystyrene

RSMPs Reversible shape memory polymers

SMPs Shape memory polymers

UMAT User material subroutine

Chapter 1

Brief Introduction

In this chapter, an overview of each topic in this dissertation is provided. Started with investigating the origins of the size effect of polymeric nanofibers, polyethylene (PE) and polystyrene (PS) nanofiers are simulated by molecular dynamics. The mechanisms of the size effect of PE and PS nanofibers are found differently, although similar aspects also exist. Next, our methodology is then applied to investigate the size-dependent thermomechanical response of functional polymers subjected to an external stimulus (high-intensity focused ultrasound (HIFU) in this case). In chapter 3, an experimentally-validated finite element framework is developed to study the thermal response of functional shape memory polymers (SPMs) under ultrasound field. This computational framework at macroscale helps the design of the controlled drug delivery (CDD) systems. Moreover, the mechanisms of the thermal effect of polymers in HIFU Fields are then studied at molecular level. It is found the viscoelastic response under specific vibrating frequency is a vital point associated with the thermal effect of polymers under HIFU. In additions, a shape memory polymer composite with enhanced shape recovery ability and also a two-way shape memory polymer are synthesized. A smart gripper and a self-rolling structure are designed, which shows SMPs are good candidates in engineering fields. Finally, the influence of the evaporation during nanofiber formation process in chapter 7. The detailed introductions for every topic are followed.

1.1 Size effects in the mechanical properties of PE and PS nanofibers

Mechanical properties of ultra-fine polymeric nanofibers are highly size-dependent and the mechanisms for causality of the size dependency is still not quite clear. To unravel the unknowns, we investigate the origins of this size dependency at the atomistic level. By using molecular dynamics (MD) framework, for PE nanofibers, two fabrication methods are utilized in this study to prepare non-drawn and hot-drawn fibers, in order to investigate the two distinguished mechanisms for size dependency in PE nanofibers. One is rooted in the effect of surface chains which is intrinsic to low dimensional materials and the other is the chain alignment induced by drawing during fiber fabrication process. Our results show that the size dependency is not chiefly attributed to the effect of surface polymeric chains, but rather strongly relates to the chain alignment in nanofiber's microstructure. The atomistic study shows that non-drawn nanofibers have a dense core covered by a less dense shell layer, but interestingly, our investigations reveal that the core-shell structure itself will not result in the remarkable increase of modulus and strength when diameter of the fiber drops down. By testing the hot-drawn fibers, we found the size dependency mainly originates from the chains alignments. In addition, by examining the energy evolution associated with the bond lengths, bond angles and dihedral angles at the atomistic scale, our results show that the dihedral angles play a vital role in the size-effect. Our results also show the the orientation-induced crystallization is monitored on hot-drawn fibers at 300 K, which makes the semicrystalline fibers become stiffer but less ductile.

Unlike the semicrystalline PE nanofiber, PS nanofibers are usutally amorphous. Here, we investigate the role of chain alignment and backbone bond length on the diameter dependence of individual amorphous polystyrene (PS) by molecular dynamics (MD) simulation. For the

first time, the diameter of the modeled nanofibers in MD can be directly comparable to the experimental scale. We observed a linear increase of ultimate strength and an exponential increase of Young's modulus when reducing the nanofiber diameter to a certain onset value. The increase of ultimate strength is found to be more related to the linearly increased chain alignment while the variation in Young's modulus is directly attributed to the exponentially increased backbone bond length. The parameter "normalized diameter" is also introduced to evaluate the extent of chain confinement in nanofibers. Finally, MD simulation is validated by comparing with experimental results, and a annealing model demonstrating the evolution of molecular structure with diameter is proposed.

1.2 Shape memory polymers in HIFU fields

As mentioned, the size effects in polymeric materials are not limited to the mechanical response, in an external stimulus fields, the thermal response of SMPs is also size-related. In chapter 3, we present an experimentally-validated acoustic-thermoelastic framework for modeling the high-intensity focused ultrasound (HIFU)-induced thermal actuation of shape memory polymers (SMPs). The feasibility of using SMPs stimulated by HIFU for designing controlled drug deliver (CDD) systems is also investigated. SMPs represent a new class of materials that have gained increased attention for designing biocompatible devices. These polymers have the ability of storing a temporary shape and returning to their permanent or original shape when subjected to external stimuli such as heat. In this work, HIFU is used as a trigger for noninvasively stimulating SMP-based systems. HIFU has a superior capability to localize the heating effect, thus initiating the shape recovery process only in selected parts of the polymer. The multiphysics model optimizes the design of a SMP-based CDD system through analysis of a filament as a constituting base structure and quantifies

its activation under HIFU. Experimental validations are performed using a SMP filament submerged in water coupled with the acoustic waves generated by a HIFU transducer. The modeling results are used to examine and optimize parameters such as medium properties, input power and frequency, location, geometry and chemical composition of the SMP to achieve favorable shape recovery of a potential drug delivery system.

1.3 Polyethylene in HIFU fields

Experiments and the macro-scale computational model in chapter 4 show that high-intensity focused ultrasound (HIFU) is a promising stimulus which has a superior and unique capability to induce localized heating and achieve temporal and spatial thermal effects in the polymers, noninvasively. When polymers are subjected to HIFU, they heat up differently compared to the case they are subjected to heat sources directly; however, the origins of this difference are still entirely unknown. We hypothesize that the difference in the macroscale response of polymers subjected to HIFU strongly depends on the polymer chains, composition, and structure, i.e., being crystalline or amorphous. In this work, this hypothesis is investigated by molecular dynamics studies at the atomistic level and verified by experiments at the macroscopic scale. The results show that the viscoelasticity, measured by stress-strain phase lag, the reptation motion of the chains, and the vibration-induced local mobility, quantified by the root mean square fluctuation (RMSF) contribute to the observed difference in the HIFU-induced thermal effects. This unravels the unknown mechanisms behind stimulating the polymers by HIFU, and paves the way in front of using this method in future applications.

1.4 A SMP composite with enhanced shape recovery ability

As mentioned, shape memory polymers have received extensive attention to be used as actuators in a broad range of applications such as medical and robotic devices. Their ability to recover large deformations, and their capability to be stimulated remotely have made SMPs a superior choice among different smart materials in various applications. In chapter 5, a ductile SMP composite with enhanced shape recovery ability is synthesized. This SMP composite is synthesized by a mixture of acrylate-based crosslinkers and monomers, as well as polystyrene (PS) with UV curing. The composite can achieve almost 100% shape recovery in 2 seconds by hot water or hot air. This shape recovery speed is much faster than typical acrylate-based SMPs. In addition, the composite shows excellent ductility and viscoelasticity with reduced hardness, which can lead to good thermic response when the composite is remotely actuated by high intensity focused ultrasound (HIFU). Besides, molecular dynamics (MD) simulations are performed for understanding the curing mechanism of this composite. With the combination of the experimental and computational works, this study paves the way in front of designing and optimizing the SMP devices.

1.5 A two-way shape memory polymer for soft actuator applications

Chapter 6 explore the potential applications for SMPs. In this chapter, the SMPs with reversible shape recovery property (two-way shape memory) are highly desired. In chapter 6, a crosslinked poly(ethylene-co-vinyl acetate) (cPEVA) based two-way shape memory polymer

is synthesized using dicumyl peroxide (DCP) as the crosslinker. Moreover, the influence of the DCP concentration on the mechanical properties and the two-way shape memory properties is systematically studied. More importantly, soft actuators made by cPEVA with an optimal DCP concentration can perform gripping and self-rolling movements, indicating that the resultant cPEVA SMP is capable of producing large output force and recovering from large deformation. Additionally, finite element simulations are also conducted to further understand the underlying mechanisms in the complex behavior of actuators based on cPEVA SMP. This work provides important insights in designing smart materials with external stimulus responsive programmable function for soft actuator applications.

1.6 The effect of evaporation during nanofiber formation process

Polymeric nanofibers are unique one-dimensional materials formed by the solidification from viscous polymeric solution. Their continuous structure, nanoscale dimension and relative ease of preparation process make them valuable materials in many engineering applications. However, the investigation on the inner microstructure of nanofibers by direct experimental methods is still challenging. There are still contradictory views on the core-shell structure of the nanofiber. Some researchers found the nanofibers have a dense core with less dense shell area, Some other researchers found the core area is less dense. In chapter 7, we use molecular dynamics simulation to investigate the roles of evaporation rate and the stretching forces. The results indicate that the formation of the network structure of nanofibers are because of a balance of evaporation and stretching. When the evaporation is dominant, nanofibers tend to form a tabulated structure will less dense core area. When the stretching is dominant, there is a compacting phenomenon, and the fiber will have a denser structure.

Chapter 2

The origins of size dependency of polymeric nanofibers

2.1 Size effect of PE nanofibers

2.1.1 Introduction

In the field of polymer engineering, the technology of polymeric nanofiber fabrication has received extensive attention during the past two decades, mainly because of the unique features of nanofibers, and the low cost of production process for these fibers [1–4]. As a new class of one dimensional materials, polymeric nanofibers can be used in diverse applications, such as scaffolds in tissue engineering, drug delivery devices, and polymer carbon nanotube composites [5–7]. Particularly, with diameters ranging from 10 to 500 nm, polymeric nanofibers exhibit high surface area to volume ratios, high tensile strengths, reduced glass transition temperatures, as well as unique size-dependent mechanical responses. These remarkable properties, which are closely related to polymeric nanostructures, have been widely studied by different experimental and computational methods in the past few years [8–15].

To elucidate the nanostructures and corresponding mechanical properties of polymeric nanofibers, a broad range of experimental works and molecular dynamics (MD) simulations have been reported recently. Pisignano and co-workers [16] evidenced that a core-shell structure is

formed with a dense core and less dense shell, due to the dominant stretch rate during the fiber formation process. Barber et al. [17] studied the elastic modulus of individual electrospun polyvinyl-alcohol (PVA) fibers. Their results indicated an increase in the elastic modulus, as the fiber diameter decreases. A bead-spring model for generic glassy polymers has been developed by Shan Tang, et al. [18], by which the core-shell system consisting of a dense core embedded in a less dense polymeric shell has been successfully simulated. However, the size-dependent mechanical properties are still needed to be quantitatively studied by that model. More recently, Cai et al. investigated the microstructure and mechanical properties of PAN/SWNTs nanofiber, their results showed the hot-drawing approach can enhance the alignment of the polymeric chains and SWNTs in nanofiber [19].

Based on the reported experimental and computational investigations, multiple explanations have been reported to explain the size-dependency of elastic modulus and tensile strength in polymeric nanofibers. Among these, two justifications are prominent and compatible with some experimental observations; (i) the effect of core-shell structure, in other words, the effect of surface chains which is intrinsic to low dimensional materials and (ii) the effect of chain alignment, which are both related to the size as discussed in the following.

The core-shell justification relates the fiber's size dependency to the size of core and shell in the fiber's cross section. As the fiber size decreases, the energy at the core area increases [20], and consequently the surface-to-core ratio changes in the fiber. This explanation considers this ratio being the origin of the observed size dependency in the parameters. Although this explanation is supported by some theoretical calculations, experiments have claimed that the surface effect cannot explain the dramatic increase in the elastic modulus by itself [21, 22]. More recently, it has been suggested that the chain alignment which stems from the processing induced size-dependent microstructure might attribute to the size dependency and enhancement in the mechanical performance [19, 23]. Based on this idea, it is sug-

gested that the hot-drawing process during fabrication of polymeric fibers acts as a critical step for creating high performance nanofibers [24]. For instance, when a hot polyethylene (PE) filament is drawn at very high hot-drawing ratios from the solution, the amorphous PE filament re-orients in the drawing direction and solidifies after cooling down [25]. By theoretical analysis, this kind of well-orientated nanofiber could reach a very high tensile strength [26]. However, although the interaction of chain alignment and size dependency has been observed in multiple experimental works, many of the fundamental mechanisms behind this interaction are still highly unexplored.

In this section, we adopt MD to study the interaction between the effect of surface polymeric chains (core-shell structure), the chain alignments and the size dependency in polyethylene nanofibers at the atomistic level. In order to investigate the mechanisms for size dependency, a verified united atom model is utilized and two fabrication methods (fiber with hot-drawing and without hot-drawing) are used to prepare two types of nanofibers that have differently initial microstructures. Diverse structural characteristics of these two structures, such as density profile, chain orientation, internal energy evolution and orientation-induced crystallization, as well as the mechanical properties, are studied to find the relationship between the fiber's internal microstructure and the related mechanical response.

2.1.2 Models and methods

We use the united atom model to generate the studied nanofibers. The interatomic potential we employed in this chapter is based on a united atom model for PE which was proved to accurately capture the physical properties of PE melt and PE crystallization process [27, 28]. This interatomic potential has two contributing components: bond interactions and non-bond interactions. The bond parts consisting of bond stretching, bond angle and dihedral

angle are represented as follows:

$$E_{bond}(r) = k_b(r - r_0)^2$$

$$E_{angle}(\theta) = k_\theta(\theta - \theta_0)^2$$

$$E_{dihedral}(\phi) = \sum_{i=0}^{3} C_i(cos(\phi))^i$$

where, for PE, $k_b = 350\ kcal/mol$ is the harmonic bond stretching coefficient, $r_0 = 0.153\ nm$ is the average bond length. $k = 60\ kcal/mol/rad^2$ refers to the stiffness constant for the bond bending (angle) interaction, $\theta_0 = 1.911\ rad$ is the equilibrium angle. The dihedral angle equation is described as a multi-harmonic format with four constant coefficients as $C_0 = 1.553$, $C_1 = 4.06$, $C_2 = 0.867$, $C_3 = -6.48\ kcal/mol$. ϕ is the dihedral angle. The non-bonded interaction is given by a Lennard-Jones potential as,

$$E_{LJ}(r) = 4\epsilon[(\sigma/r)^{12} - (\sigma/r)^6]$$

where $\epsilon = 0.401\ nm$ and $\sigma = 0.112\ kcal/mol$. All the simulations are performed by using a large-scale atomic/molecular massively parallel simulator (LAMMPS), a widely used molecular dynamics code from Sandia National Laboratories [28]. The motion equation is integrated by Velocity-verlet algorithm with a time step $t = 1\ fs$. A Nose-Hoover thermostat and barostat is used to control the system temperature and pressure.

Before creating the initial structure and performing mechanical test for PE nanofibers, to test the validity of the ability of this united atom model to capture the mechanical behavior of PE polymer, first we compared the results obtained from this united atom interatomic potential with the results obtained from a model with a PCFF force field, a classical potential force filed for the full atomistic model, separately to run simple tensile tests on a cubic PE

system as verification purpose. The initial chain structure of this cubic system is constructed by amorphous cell section based on the PCFF force field. The constructed structure is a bulk disordered systems containing carbon and hydrogen atoms in pre-equilibrium conformation mimicking realistic amorphous PE polymer. The well-constructed structure with periodic boundary conditions is then equilibrating at 600 K under zero pressure in the NPT ensemble and subsequently cooling down to 100 K. After the temperature quenching down to 100 K, a glassy state is obtained and finally the uniaxial tensile test is implemented to predict the stress-strain relationship. For the comparison of mechanical properties between full atomistic model and united atom model, another bulk cubic structure is also generated by deleting all the hydrogen atoms in the previously constructed amorphous structure. Every bead in the new structure is regarded as the hydrogen atoms are combined with the carbon atoms to which they are attached, which is exactly the same as the definition of the united atom model. Following the same simulation procedures, a stress-strain curve is obtained at the end.

The stress-strain curves for the bulk PE system deformed at 100 K based on united atom model and full atomistic model are compared in Figure 2.1. As shown in Figure 2.1a, the full atomistic bulk PE system contains 6,000 carbon atoms and 12,040 hydrogen atoms with a total number of 18,040 atoms. Figure 2.1b shows the united atom bulk PE system with 6,000 atoms in total, since a methylene or methyl group are treated as a united atom. From Figure 2.1c, noticeable fluctuation in stress-strain curve can be seen for full atomistic model while the curve for united atom model arises and proceeds more smoothly. The reason may come from the well-known fact that the thermomechanical properties might be altered in the united atom model due to the altered dynamics and loss of degree of freedom. It is evidenced that the results predicted by the two models match within an acceptable accuracy. The discrepancy of the stress-strain responses are within acceptable range, particularly, if

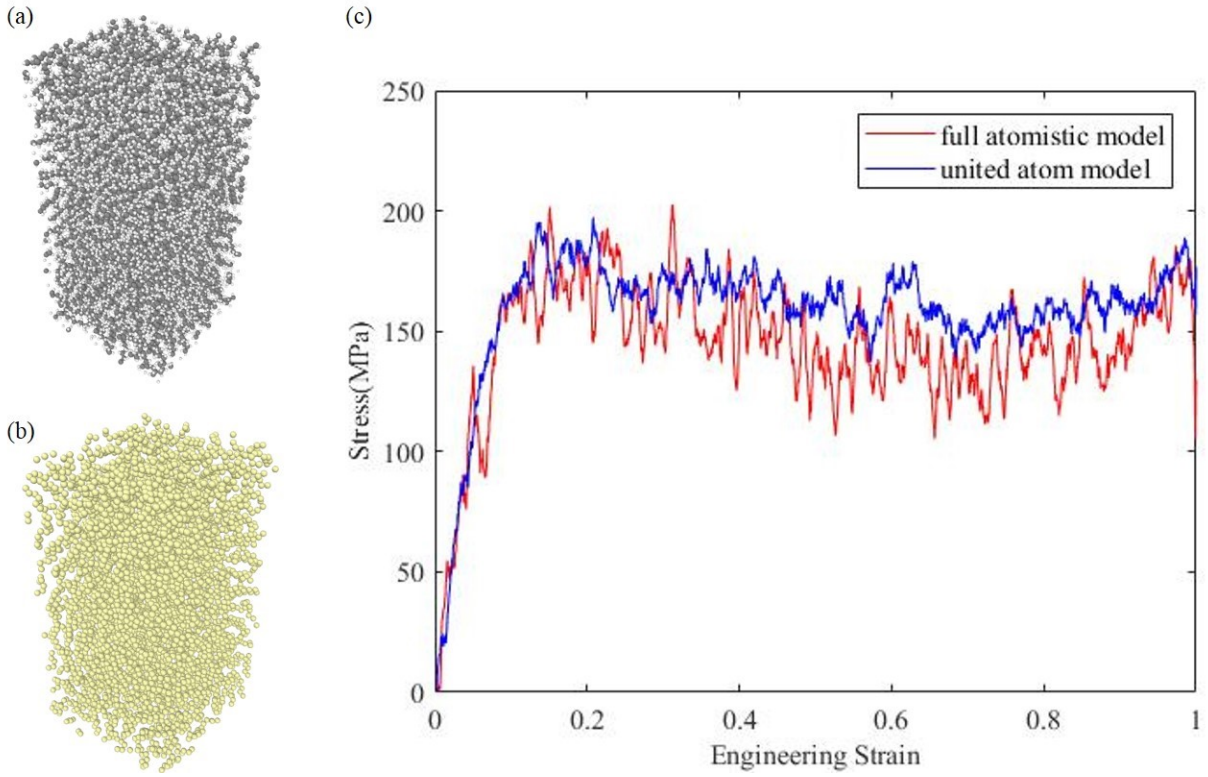

Figure 2.1: Stress-strain response of polyethylene (PE) deformed in uniaxial tension at 100 K. (a) Schematic representations of full atomistic PE system and (b) united atom PE system. (c) Stress-strain response of bulk PE polymer based on these two models.

we are focusing on the young's modulus and yield strength, which are the key features for comparison of nanofiber's size-effect.

The PE nanofibers are fabricated by the following method. First the initial structure is built by a self-avoiding random walk method [29, 30]. The randomly orientated polymer chains are placed inside a cylinder volume with the periodic boundary condition only in z direction (the fiber axial direction). Non-periodic boundary conditions are applied along x and y directions of the simulation box (the box dimensions in x and y are two times larger than the diameter of the constructed fiber). Under these conditions, the nanofiber can keep its cylindrical shape upon further equilibrium.

The nanofiber systems are then treated by two different methods, without hot-drawing and

with hot-drawing. For the first method (without hot-drawing), the cylindrically shaped nanofiber is relaxed and equilibrated following a sequence of steps. Initially, the fiber is equilibrated at 500 K in the NVT ensemble for 1 ns, which the temperature is above the melting temperature of PE. Next, a NPT dynamics is followed to decrease the temperature from 500 K to 100 K under zero pressure in z direction. During this cooling step, the fiber is allowed to adjust its density by changing the length and the radius. After the glassy PE nanofiber obtained, a NPT ensemble is run to remove its internal stress in z (the axial) direction before uniaxial deformation is performed. Upon this fabrication method, the fiber systems consisting of 20 to 4200 chains with the same chain length (301 monomers per chain) in a total of 6,020 to 1,264,200 united atoms are prepared for the purpose of modeling differently sized amorphous nanofibers. The results of the diameters of nanofiber systems are ranging from 5 nm to 30 nm. Then, the stress-strain relationship is obtained by a uniaxial tensile test along z-direction, when the simulation box is deformed at a constant engineering strain rate under NVT ensemble.

As for the second fabrication method, hot-drawing is applied when fiber is forming to emulate the procedure of making hot-drawn fibers in the experiments. The initial structure is composed by 700 polymer chains with 301 monomers per chain and thus 210,700 united atoms contained in the nanofiber system. An equilibrium process is firstly performed at 500 K similar to the first method. Thereafter, a linear increased force is added to all atoms in the simulation system along fiber axial direction. Traditionally, by giving an additional push to atoms in a specific direction, this method is usually used to emulate the fluid flow in a channel. Here, we employ this method to simulate the hot-drawing process, which the as-spun fiber were stretched by hanging weights in a furnace [19]. A cylinder wall is implemented at the mean time to help the decrease of the nanofiber size and regulation of nanofiber shape. The conformations of the hot-drawn structures are saved at different hot-drawing ratios as

initial structures for the further cooling step. By this method, at low strains, larger diameter fibers are obtained, while increasing the strain results in smaller diameter fibers. Thus, after hot-drawing, nanofibers will have different sizes. Uniaxial tensile test simulations are then performed on these differently sized fibers at 100 K. Decreasing the temperature from 500 K to 100 K in NPT ensemble for 500 ps, the final state of hot-drawn fibers have a diameter of 10, 12, 12.5 and 19 nm. Finally, the mechanical tests are performed on these differently sized fibers under 100 K.

After testing the mechanical response for non-drawn and hot-drawn fibers at 100 K, the effect of temperature on stress-strain behavior was further investigated. The 10 nm fibers are deformed at 300 K and then the results are compared with the corresponding results at 100 K. Additionally, in order to monitor the crystalline structure inside fiber, two fibers which are both prepared by the hot-drawing method but have different hot-drawing ratios are running under npt ensemble for another 10 ns at 300 K. Finally, the tensile tests are performed on the fibers at 300 K similar to previously mentioned procedure.

2.1.3 Comparison of non-drawn and hot-drawn fibers

The results presented in this section reveal the structural deference and corresponding pronounced mechanical property change of nanofibers prepared by the two different fabrication methods. In Figure 2.2a, representative snapshots of final structures of 10 nm PE fibers prepared by both methods are displayed for comparison. Different chains are displayed using different colors. Without hot-drawing, Chains are randomly orientated and distributed in the system. The random molecular jumble lacks the long-range order, thus the nanofiber is in amorphous state. However, treated by the hot-drawing, it can be seen clearly the PE chains are well ordered along fiber's axial direction.

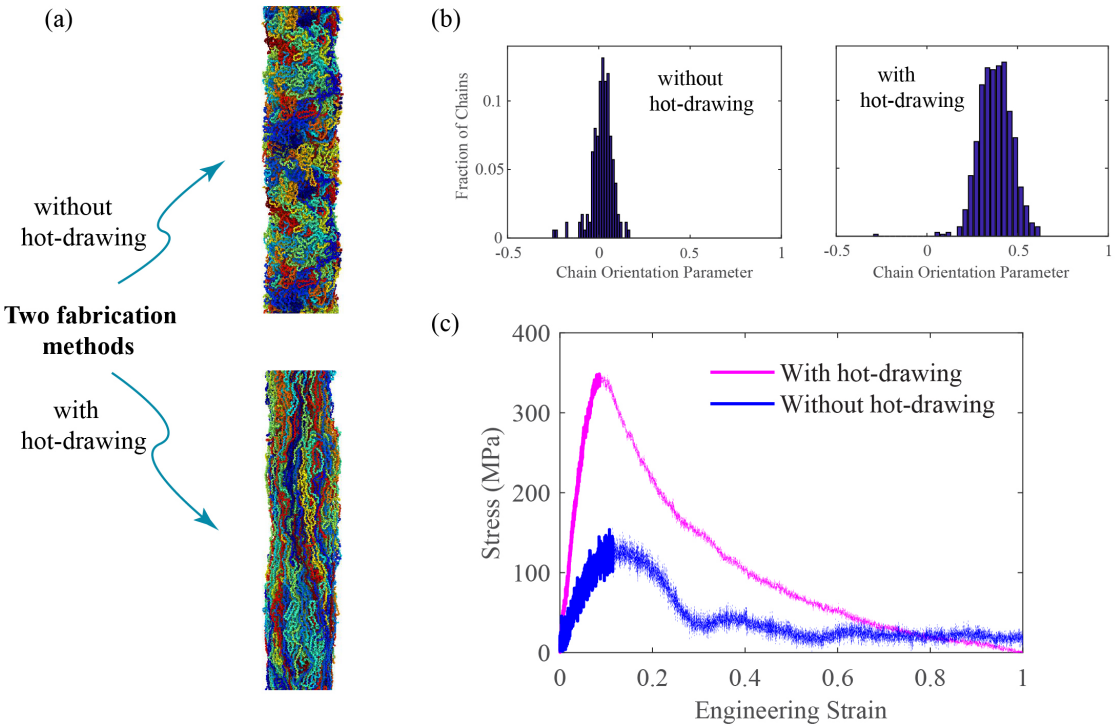

Figure 2.2: (a) Representative snapshots of the 10 nm polymeric nanofiber with and without hot-drawing and (b) the distribution of the chain orientation parameter P of 10 nm nanofiber without hot-drawing and with hot-drawing. $P_{2z} = 1$, $P_{2z} = 0$ and $P_{2z} = -0.5$ refer to perfect alignment in the z-direction, no significant alignment and normal to z-direction (see text for details). (c) Stress-strain response of uniaxial tensile test for 10 nm non-drawn and drawn nanofiber at 100 K. The post-peak curves are shown in dash line because the curves after the maximum load cannot be captured experimentally which is an instable state for the nanofiber.

To quantitatively evaluate the chain alignment of the nanofiber, a chain orientation parameter P_{2z} is introduced and calculated by the following equation [23, 30, 31],

$$P_{2z} = \frac{3}{2} cos(\theta_i)^2 - \frac{1}{2}$$

where θ_i is the angle between z-direction and the vector from atom $i-1$ to nearby atom i+1 alone the same chain. In this manner, the results of $P_{2z} = 1$,$P_{2z} = 0$ and $P_{2z} = -0.5$ refer to the well alignment along z-direction, lack of significant orientation and perpendicular to z-direction, respectively. The histograms of the distribution of the chain orientation along

fiber axial direction (z-direction) for both systems are shown in Figure 2.2b. Without hot-drawing, chain orientation parameters for all chain segments fall in a range from -0.25 to 0.2, with a peak value around 0 in the histogram, reflecting insignificant alignment in the fiber structure. With hot-drawing, a range from 0 to 0.6 with a peak value around 0.4 for the parameter P_{2z} can be seen from the histogram, which indicates chains have aligned orders along z-direction. This observation shows that the hot-drawing treatment can lead to a strong alignment in fiber's microstructure.

Having conducted the structural analysis on the two systems, uniaxial tensile test is then performed to measure the stress-strain behavior at a strain rate of $5 \times 10^9 \quad s^{-1}$. The results are displayed in Figure 2.2c. Surprisingly, not only the young's modulus increases significantly, but also a threefold increase of the yield strength of hot-drawn fiber is observed compared to that of non-drawn fiber. Interestingly, since the diameter of fibers for both systems are around 10 nm, by neglecting the slightly density change, this threefold increase is largely attributed to the enhanced chain alignment.

2.1.4 Non-drawn fibers with different sizes

Known that the chain orientation plays an important role in determining fiber's mechanical properties, the question to be answered in this sections, is what the reason behind fiber's size-effect is. In section 2.1.4, fibers are fabricated by the first method, fibers with diameters range from 10 to 30 nm are made without hot-drawing.

First, we examine the inner structure of the fiber, the nanofibers are divided into 25 to 150 cylindrical layers for the diameters of fibers ranging from 10 nm to 30 nm, in which each layer has identical thickness of 0.1 nm. The numbers of the atoms in each layer are counted and then divided by the corresponding shell volumes which can be defined as the number

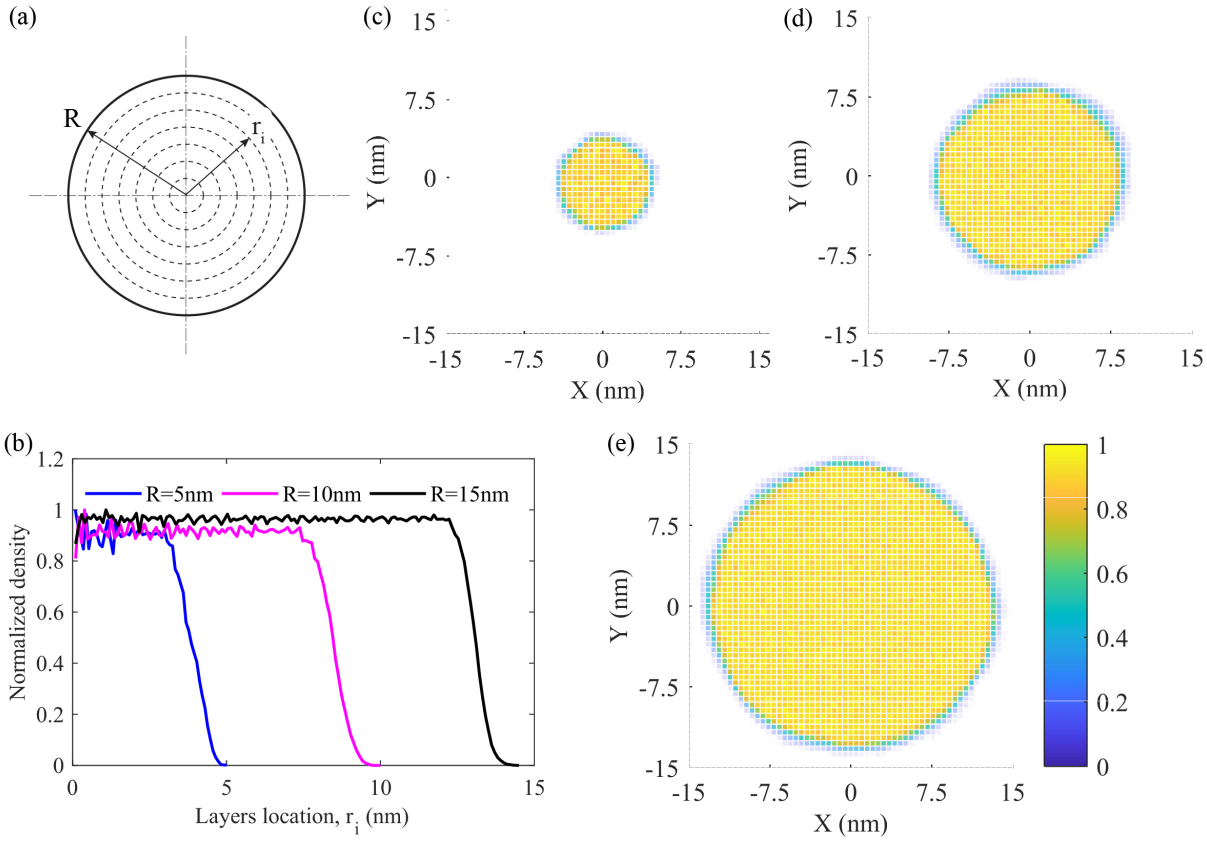

Figure 2.3: (a) The schematic graphs shows the nanofiber is divided into multiple concentric layers. (b) Normalized density of PE nanofiber at T=100 K, along the radial direction from the center to surface and normalized density distribution on the fiber's cross-section with diameters equal to (c) 10 nm (d) 20 nm (e) 30 nm. In each case a dense core and less dense shell structure is shown (the color bar shows the normalized density).

density of polymer beads. Figure 2.3 shows the normalized number densities along radius for differently sized fibers. As shown, the densities of inner layers spontaneously fluctuate around a constant value that refers to the bulk density of PE. Due to the surface tension of the nanofiber, clearly, the density in the inner area is higher than the outer area, which can be regarded as a core-shell structure (For nanofibers made with polymer-solvent system, some experimental results show that the constructed fibers may have soft core embedded with hard shell structure, since solvent molecule will be trapped inside due to fast solvent evaporation on surface. However, when evaporation rate is not dominant, experiments show

fibers have a higher polymer density in the center which results in a dense core, and less dense shell structure).

For fibers with 10 nm diameter, the density remains constant up to $\frac{r}{r_{max}} = 0.6$, beyond this point, the density drops down quickly which can be defined as the shell (surface) area. As the diameter of the fiber increases, the shell to core ratio decrease. Similar results are reported by Shan Tang et al. [18], they use a bead-spring model to emulate a glassy nanofiber system, the core volume fraction is increasing from 57.76% to 84.64% for fibers with increased diameter from 19.78 to 98.36 in reduced LJ units.

To illustrate the cross-sections of the fibers in a more straightforward way [32], density profiles of the fiber systems are demonstrated in Figures 2.3c-e. Clearly, the core area become dominant with increase of the fiber size, while the thickness of the shell layers are not varied significantly.

Mechanical tests are also performed on these fibers to investigate the effect of surface chains on fiber size dependency. Fibers in three different sizes, with diameters 10, 20, and 30 nm are deformed at 100 K with a constant strain rate $5 \times 10^9 \quad s^{-1}$ and the results are compared in Figure 2.4. Need to note that for all tensile tests performed in our study, we keep the same strain rate. It is observed that young's modulus and the yield strength of differently sized fibers do not change significantly. It can be noticeable that by using the first method, the resultant polymeric fibers are under close chain alignment level but with different diameters. Thus, the effect of surface chains is isolated and investigated in the section. The result reveals that for different diameter fibers of similar chain alignments, although the ratio of core-to-shell area changes, this structure change itself will not result in a significant enhancement in fiber's young's modulus and ultimate strength.

The potential energies associated with the non-bonded interaction, bond stretching, bond

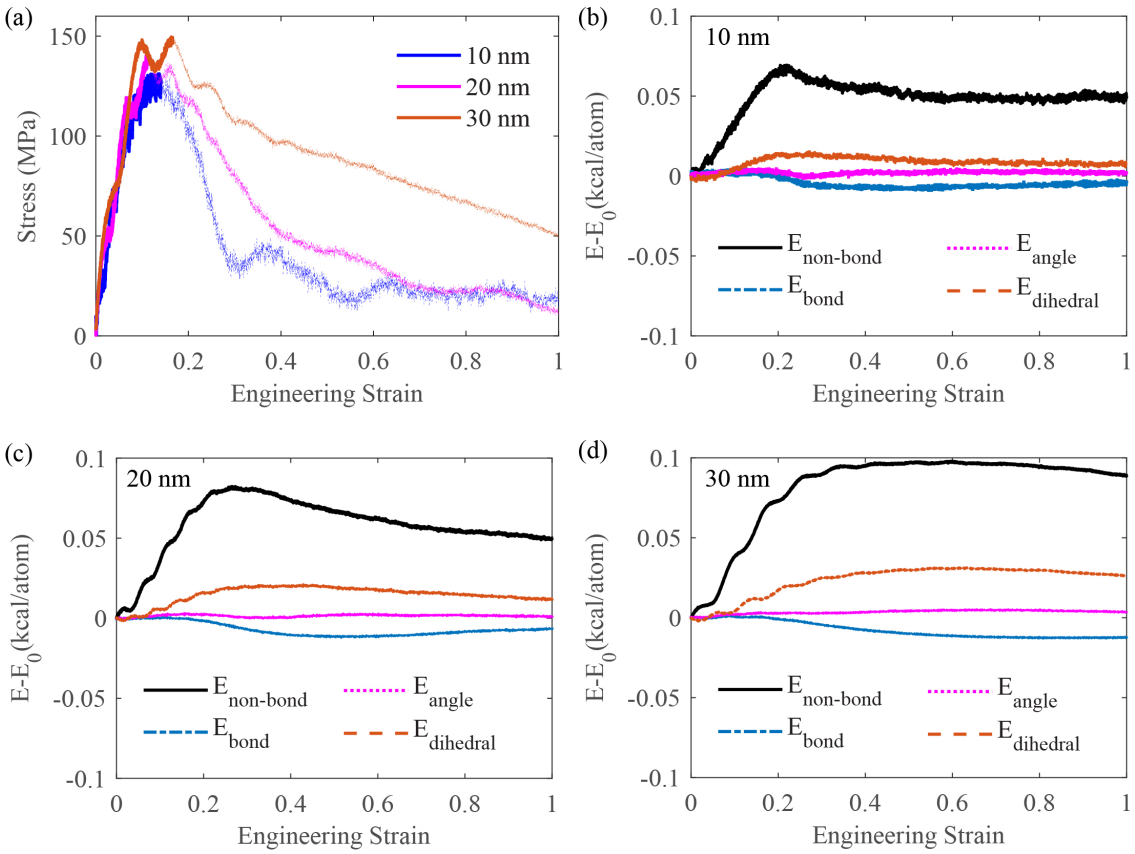

Figure 2.4: (a) Stress-strain response of amorphous PE fibers with diameters of 10, 20, and 30 nm at 100 K temperature. (b), (c) and (d) shows the energy decomposition of non-drawn PE fiber with different diameters. The majority of increase in total energy is associated with the increase in non-bonded energy.

angle and dihedral angle for the above four fiber systems are shown in Figures 2.4b-d. From a general view, the energy decomposition curves follow a similar trend in the energy evolution progress. The major increase of the total energy comes from the increase of non-bonded interaction energy, while others play a less important role, particularly in elastic region. As the bond angles stay near the equilibrium value of 109.5°, the angle energy remains nearly constant. The bond energy slightly decreases as the bond lengths move towards the equilibrium length. The dihedral energy increases slightly after the elastic regime and then decreases when the necking begins because of the transformation of global minimum trans

conformation to local minimum $guache^+$ conformation.

Focusing on the elastic region, the increase in non-bonded energy of fibers with smaller diameters are slightly lower than that of with larger diameters due to the core-shell ratio. However, such kind of variations cannot quantitatively explain the pronounced size effect that observed in the experiments. Further discussions will be provided in the following sections to reveal the correlation between the size-effect and fiber internal structure.

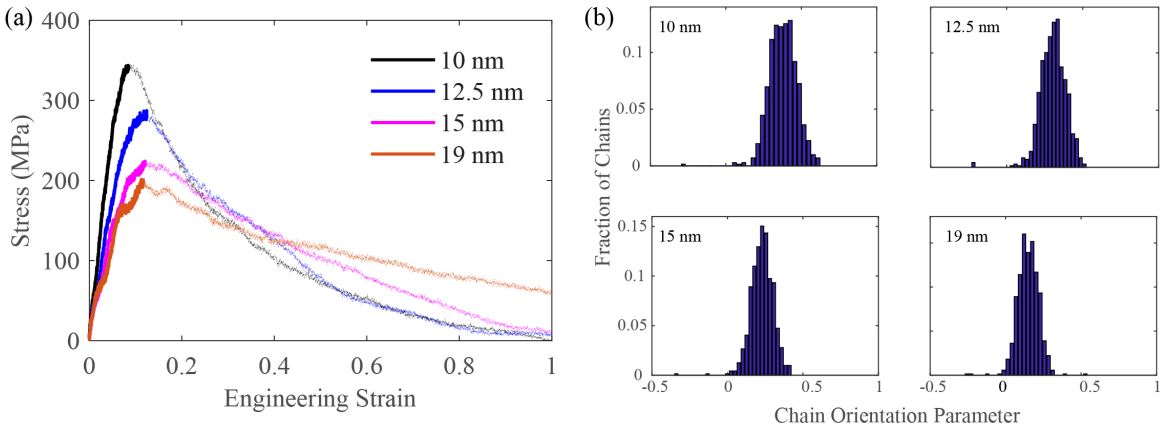

Figure 2.5: (a) Stress-strain curve for 10, 12, 15, and 19 nm hot-drawn nanofibers and (b) chain orientation parameter of hot-drawn nanofibers.

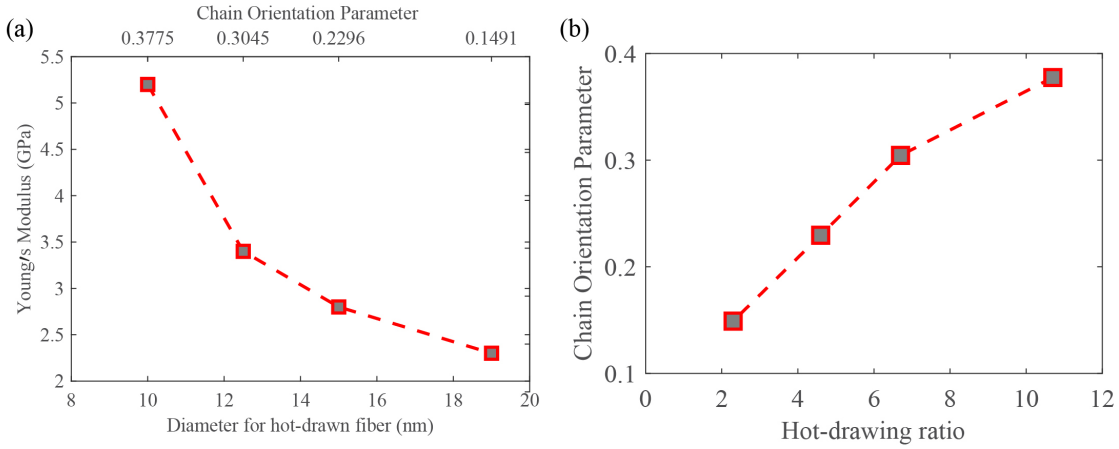

Figure 2.6: Young's modulus versus diameters and corresponding chain orientation parameter for hot-drawn fiber. (b) Chain orientation parameter as a function of hot-drawing ratio.

2.1.5 Hot-drawn fibers with different sizes

To confirm the correlation between the dependency of properties to the size and the inner chain orientation, the prepared nanofibers which are hot-drawn to different strain levels are deformed by uniaxial tensile tests. The stress-strain curves are provided in Figure 2.5a. It is clearly shown that with decreasing the fiber diameter (increasing the hot-drawn ratio), the young's modulus and the yield strength increase rapidly. Comparing the results for 10 and 19 nm fibers, a nearly triple increase of corresponding properties is observed as shown in Figure 2.6a.

As shown in Figure 2.5b, Figure 2.6a and Figure 2.6b, nanofibers with increasing hot-drawing ratio have decreasing diameter and increasing chain orientation parameter. In other words, higher hot-drawing ratio leads to formation of thinner fibers with more aligned polymeric chains in the microstructure. In figure 2.5b the corresponding distribution of chain orientation parameter for all chain segments in each fiber is shown. The majority of the values of orientation parameter are ranged from 0.15 to 0.6 (for 10 nm fiber), 0.1 to 0.5 (for 12.5 nm fiber), 0 to 0.4 (for 15 nm fiber) and 0 to 0.3 (for 19 nm fiber). Not surprisingly, on average, the chains tend to align when the fiber is drawn to higher strain level. The average values of chain orientation parameter obtained in our results are relatively lower compared to the Herman orientation factor obtained from experiments on hot-drawn nanofibers [19]. The reason is that the nanofiber size and the length of chains used in MD simulation are limited. To reach a higher Herman orientation, system needs to be large enough to provide enough entanglements in amorphous phase resulting in polymers with longer chain lengths having higher degree of alignment [30]. In addition, the method used to calculate the chain orientation parameter in MD simulation is slightly different from the method about Herman orientation parameter calculation obtained from experiments [19, 33]. The size dependency of nanofibers can also be described by normalizing the diameter by the characteristic length

scale of the material [34]. In this study, since all nanofibers are composed by same length polymeric chains (same molecular weight), there is a positive linear correlation between the actual diameters and normalized diameters for the fibers.

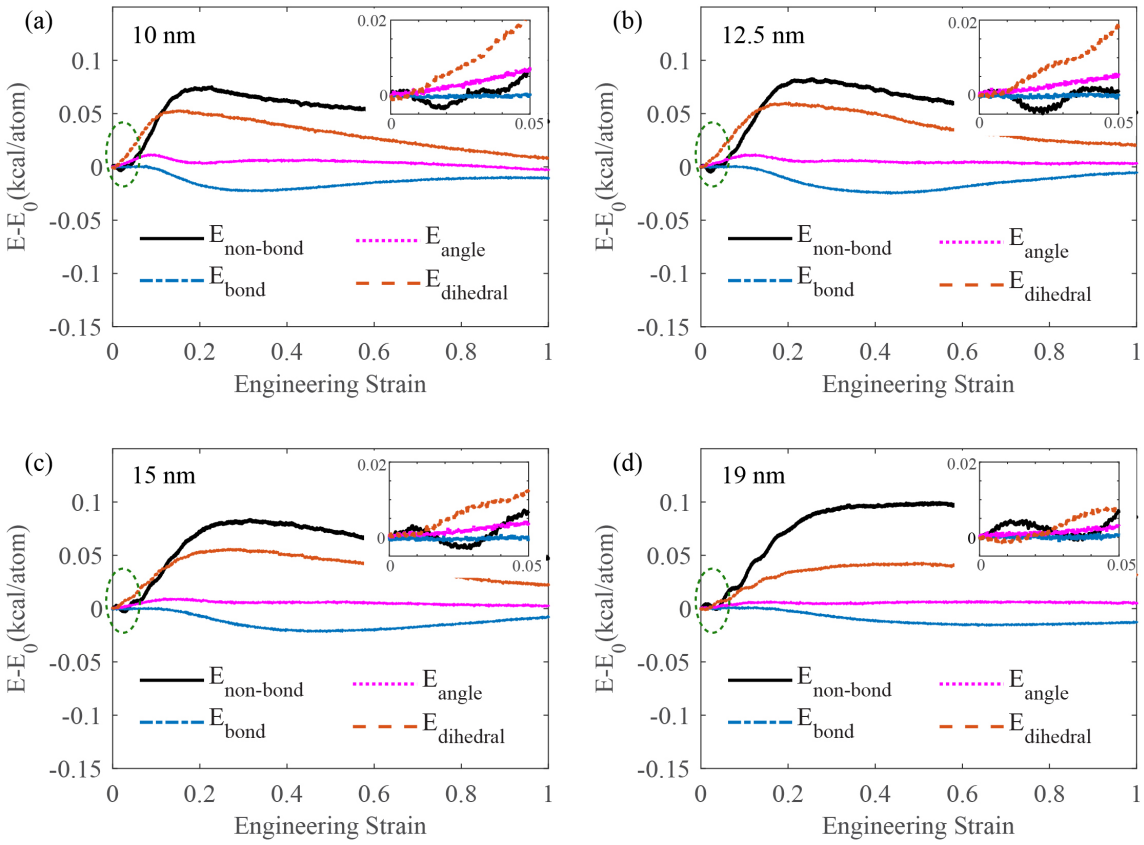

Figure 2.7: Young's modulus versus diameters and corresponding chain orientation parameter for hot-drawn fiber. (b) Chain orientation parameter as a function of hot-drawing ratio.

The evolution of fiber internal energies during the tensile test is also analyzed. According to Figure 2.7, the energies associated with the non-bonded interactions follow a similar trend when strain evolves. For a thinner fiber, dihedral energies have a sharper rising gradient, and the angle energies also curve up when the tensile test starts. The bond energies exhibit pronounced decrease at elastic region as the length of the bonds approaches its equilibrium value. For thicker fibers, the curves of dihedral energies remain flat at small strains, bond energies decrease steadily and angle energies keep almost unchanged during the whole strain

evolving process. Focusing on elastic regime (up to 0.05 strain), as zoom-in figures are displayed at the top right corner on each subplot, it is noticeable that the dihedral energy plays a vital role in the elastic regime. Note that the dihedral potential chosen in the present work has three staggered positions, one trans and two gauche states. The global minimum of the dihedral potential is at 0°(trans) and two local minima are located at -120°($guache^-$) and 120°($guache^+$), respectively. The trans-guache barrier in this potential is 3.3 kcal/mol while the cis barrier is at 5.0 kcal/mol [27]. In the hot-drawing process, the drawing force can help the conformations with a dihedral angle between 0° and 60° bypass the trans-guache barrier and finally reach the 120°($guache^+$) conformations. The dihedral angles further keep increasing when the tensile test is beginning and have a trend of approaching the much higher energy conformation states of dihedrals angle between 120° and 180°, that's why for the hot-drawn fibers, the dihedral energy curves up immediately at the elastic regime.

Normalized density distribution of the cross-section of the hot-drawn fiber is also obtained and shown in Figure 2.8. From Figure 2.8, it can be seen the hot-drawn fibers have core-shell structures as well, but apparently this is not the main reason behind its size dependent properties. Based on the results shown in Figures 2.5, 2.6 and 2.7, we can conclude that the size-effect of nanofibers is closely related to fiber nanostructure of chain orientations, particularly, the dihedral angle has a significant role in accounting for the enhanced mechanical properties of PE nanofibers when the fiber size decreases.

Interestingly, a lot of experimental studies also show a three-fold increase in young's modulus of thin nanofibers compared to that of bulk polymer [22, 35, 36]. Naraghi et al. [15] reported the mechanical properties of polyacrylonitrile (PAN) produced under different electrospinning conditions. For fibers with a diameter larger than 400 nm, their experimental work shows a value of about 2 GPa for the fibers, which are close to the value of bulk PAN polymer. When the diameter of the fiber decreases to 200 nm, young's modulus increases

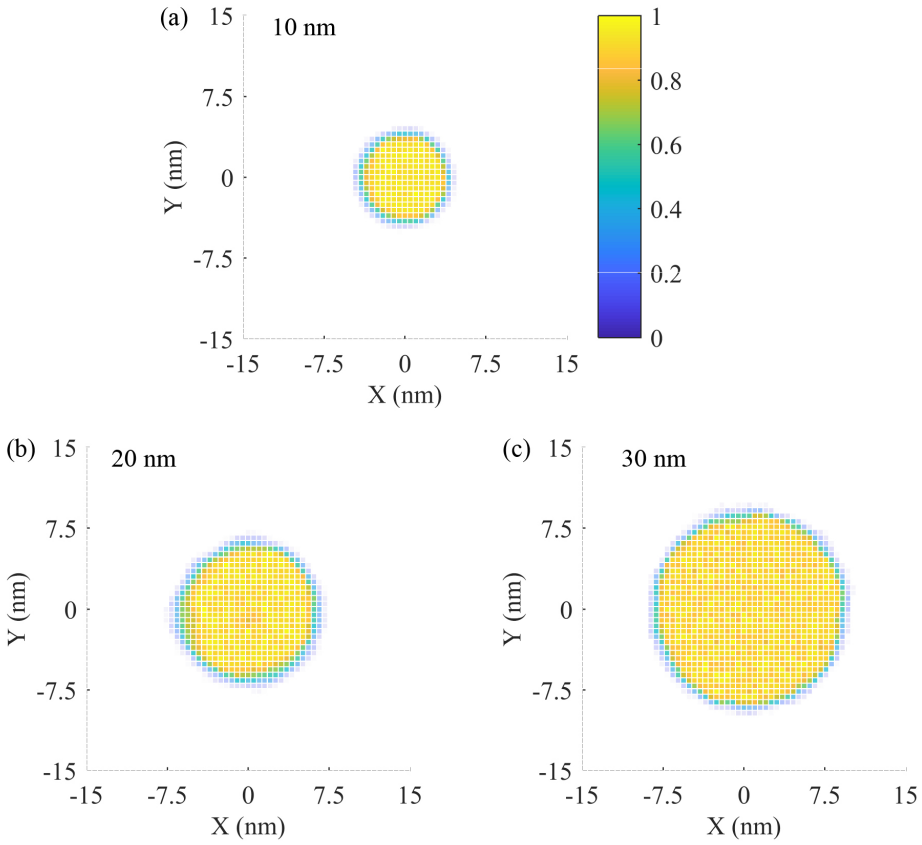

Figure 2.8: The density distribution of the cross-section of the hot-drawn fibers with different diameters

to 6 GPa. Another example for PAN fiber is reported by Dimitry Papkov et al. [37], where the results of tensile tests show dramatic increase when nanofiber is finer than 200 – 500 nm as the yield stress is about 200 MPa for a fiber with diameter of 260 nm but increases to about 500 MPa for a 138 nm fiber. These observations are compatible with our findings, although our simulations are investigating fibers with smaller diameters. Considering smaller diameters in this study is due to the inevitable limitations on MD simulations because of computational cost. We adopt relatively short polymeric chains and only up to 30 nm diameter fibers can be reached, while in experiments fibers are comprised of larger molecular weight polymeric chains and finally have larger diameters. However, from another perspective, in our simulation when drawing is applied in order to form thinner fiber,

the chain orientation evolution process resemble the mechanism that polymeric chains are aligned when hot-drawing approach is utilized in experiments [19]. We find the trend shown in our results is comparable to the experimental observations, and for the first time, the results shed light into the importance of the dihedral angle on PE fiber size effect by MD simulation.

2.1.6 Temperature dependence

The effect of changing temperature on the mechanical properties of polymeric fibers has been extensively studied. However, the interactions between core-shell structure, chain alignment, mechanical properties, and temperature are still highly unexplored. In this sections, we study the effect of changing the temperature on the mechanical properties of non-drawn fibers with a core-shell structure, and also fibers with highly aligned chains, fabricated by hot-drawing.

Figure 2.9a shows the corresponding stress-strain curves at 100 K and 300 K for a 10 nm non-drawn fiber, which indicates the mechanical property of this nanofiber has a clear dependence on the temperatures. At 100 K, the stress curves rise up nearly linearly with increased strain before reaching the yield point. The stress then undergoes a decrease because of necking and fiber breakage. However, no apparent stress decrease is observed for the stress-strain curve at 300 K.

Figure 2.9b shows the representative snapshots of the 10 nm amorphous PE nanofiber (without hot-drawing) deformed under 100 K and 300 K temperatures, respectively. At 100 K, necking starts to form on the surface of the nanofiber at strain 0.4 and propagates over the surface upon further deformation, as shown in the figure corresponding to strain 0.6. The necking phenomenon is much less pronounced at 300 K, compared to the case of 100 K when the geometries of fibers are compared at the same strain levels. This phenomenon is reason-

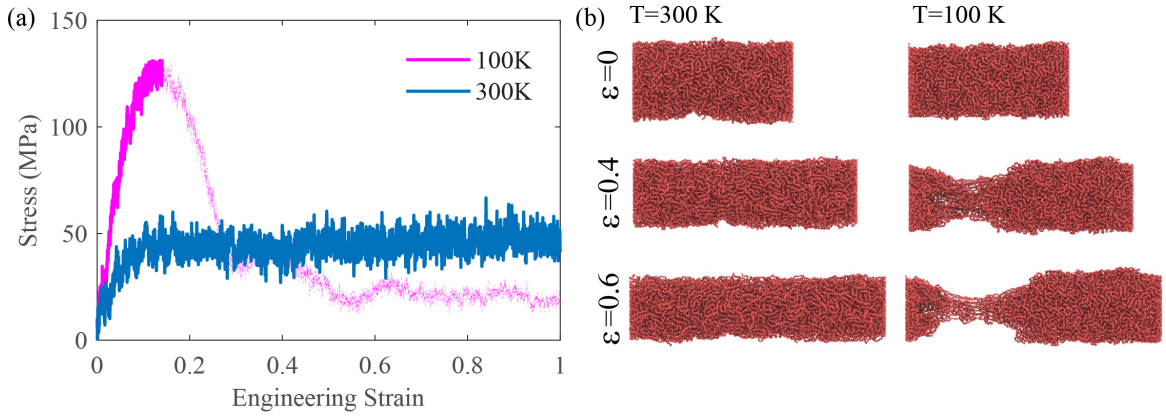

Figure 2.9: (a) Stress-strain curve for 10 nm non-drawn PE nanofiber at different temperatures and (b) representative snapshots of the hot-drawn PE nanofiber during the uniaxial tension at various engineering strains.

able because the material becomes soft and ductile when temperature increases. Moreover, Sezen et al. [20] reported that the glass transition temperatures are around 150 K for amorphous PE nanofiber by using the same force field, so actually one of the fibers is deformed below glass transition temperature while the other is above glass transition temperature in our case.

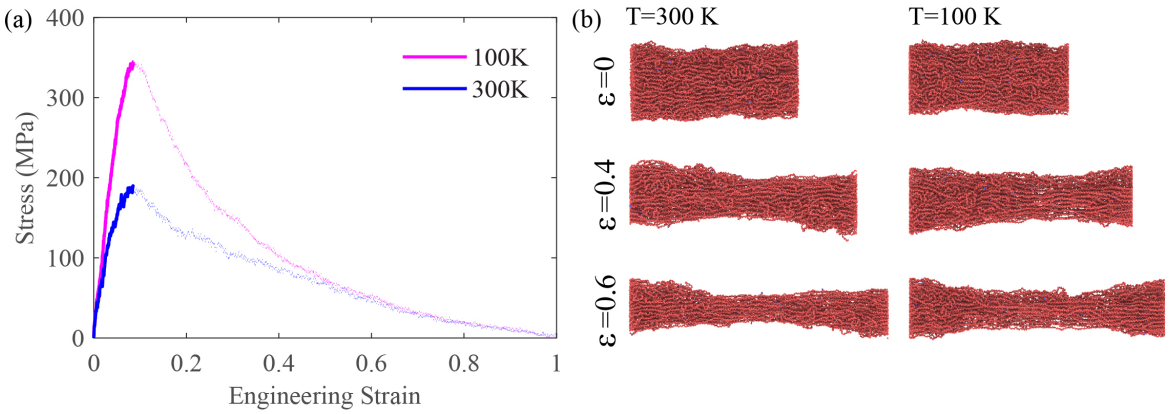

Figure 2.10: (a) Stress-strain curve for 10 nm hot-drawn PE nanofiber at different temperatures and (b) representative snapshots of the non-drawn PE nanofiber during the uniaxial tension at various engineering strains.

Temperature dependence is also investigated for a 10 nm hot-drawn fiber as shown in Figure

2.10. Not like the amorphous 10 nm fiber, the drawn fibers reach their yield point at strain 0.1 both for 100 K and 300 K. Although the values of yield strength are different at 100 K and 300 K, the stress evolution curves have similar patterns in general. Looking at the snapshots in Figure 2.10b, stable necking can be observed for both cases, and we find the neck length become longer compared to the neck of amorphous 10 nm fiber at 100 K. Comparing Figures 2.9 and 2.10, it shows that changing the temperature has a more significant on the mechanical properties of amorphous fibers as it significantly affects the stress-strain response and also the deformation in the fiber. While in fibers with aligned chains, although the strength is changed by temperature, the overall deformation mechanisms remain similar at low and high temperatures.

2.1.7 Effect of hot-drawn induced crystalline structure

In addition to the results of the increase of strength and modulus for hot-drawn fiber in section 2.1.5, another interesting part is the toughness change due to the hot-drawing. Some recent studies have explored the relationship between the nanofiber's microstructure and the toughness of the corresponding fibers. For instance, Cai et al. prepared nanofibers by hot-drawing approach experimentally and they found fibers with large drawing ratio to have high strength but low ductility, thus toughness was relatively low compared to the as-fabricated fibers [19]. To investigate the microstructural evolution and toughness of the hot-drawn fibers at room temperature, we tested two fibers with hot-drawn ratio of $\lambda = 1$ and $\lambda = 6.7$ at 300 K (close to the room temperature).

For fiber with the hot-drawing ratio of 1, it means the fiber is not drawn and the inside chains are almost disordered which is similar to the microstructure of the fiber prepared by the first fabrication method (without hot-drawing). It can be seen from Figure 2.11a, the non-drawn

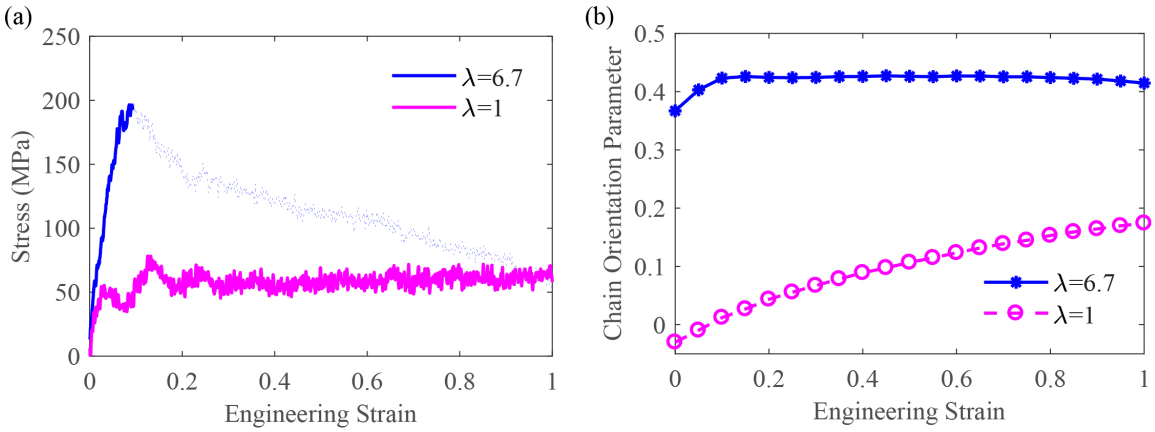

(c)

Hot-strain ratio, λ	Fiber's diameter (nm)	Crystallinity (%)
1	30	0.14
6.7	12.5	35.75

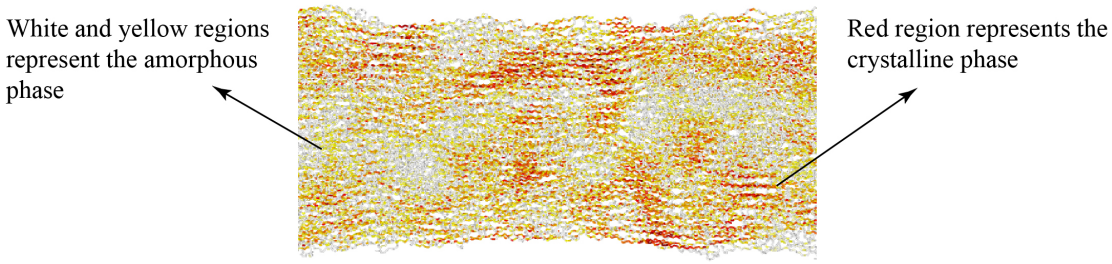

Figure 2.11: (a) The stress-strain curve for fibers with $\lambda = 1$ and $\lambda = 6.7$ at 300 K. (b) The evolution of chain orientation parameter for these two fibers during tensile test. (c) The diameters and corresponding crystallinities of these two fibers and the representative snapshots shows the crystalline phase and amorphous phase for the fiber with $\lambda = 6.7$.

fiber demonstrates the elastic-perfectly plastic property to engineering strain of 1. On the other hand, by hot-drawing, the fiber becomes stiffer while the ductility is lost. Comparing these two stress-strain curves, it is interesting to notice that increasing the hot-drawing ratio does not enhance the toughness of the nanofiber. Non-drawn fiber is amorphous prior to tensile loading for which the orientation parameter is zero. During loading, the orientation parameter increases steadily as the chains tend to align along tensile loading direction. For fiber with hot-drawing ratio of 6.7, chains are already in an aligned state before loading, and the orientation parameter grows within the first 0.1 engineering strain and then almost keeps flat for the post-peak regime. Analyzing the stress-strain curve, the stress of the hot-drawn

fiber will increase sharply in the first 0.1 strain regime and then start to drop down, which refers to fiber fracture or instability in the experiment. While the orientation parameter curve has a plateau after 0.1 strain, we note that one of the possible reasons might be that the aligned chains start to slide between each other, thus any further tensile loading cannot lead to more aligned chains.

Another reason for the loss of ductility of hot-drawn fiber may come from the crystalline structure in the fiber. From the table in Figure 2.11c, we can easily find that the hot-drawing induces the formation of crystalline structure. A representative snapshot of nanofiber with $\lambda = 6.7$ is also shown in Figure 2.11c. The crystalline region is represented in red while the yellow and white atoms refer to the amorphous region. More details about the method on the calculation of crystallinity can be found in Ref [23]. Although crystalline regions are not very thick, they distribute heterogeneously inside the fiber. The mobility of the polymeric chains in the crystalline domain will reduce which finally causes the loss of ductile for hot-drawn fiber.

2.1.8 Conclusions

MD simulations are performed by utilizing a united atom model to study the microstructure and corresponding mechanical properties of PE nanofibers. The united atom model is first validated by comparing the results of this model against a full atomistic simulation for uniaxial tensile tests. To investigate the origin of nanofibers size-dependent mechanical properties, nanofibers are formed by two methods; with hot-drawing, and without hot-drawing. Amorphous PE nanofibers can be formed without hot-drawing and thus lead to a core-shell like structure after cooling down to 100 K. Regardless of the increased fiber size, the thickness of the shell layers vary slightly which results in the discrepancy in the fraction

of the core and shell regions for differently sized polymeric nanofiber systems. Interestingly, even with such core-shell structures, the results of the tensile test cannot capture the size-effect feature when the axis-direction deformation are applied on differently sized fibers. Therefore, we can conclude that the core-shell structure (the effect of surface polymeric chains) is not the main reason for nanofiber's size dependent mechanical response. A hot-drawing process is then utilized for fiber's preparation. Comparing the structure of the non-drawn and hot-drawn fibers after cooling down, our results show that the alignment of the chains is significantly enhanced after drawing. With fiber's diameter decreasing, the hot-drawn nanofibers show a dramatic increase in young's modulus and yield strength. The corresponding energy evolution plots demonstrate that the dihedral angles play the most important role in this size-dependent mechanical response.The results show that the size dependency is not chiefly attributed to the core-shell structure, but rather strongly relates to the chain orientation in the nanofiber system as well. In addition, the formation of the crystalline structure is observed for hot-drawn fiber around room temperature, the results show the hot-drawn fiber become stiffer while their ductility become lower.

2.2 Size effect of PS nanofibers

2.2.1 Introduction

The hot-drawn PE nanofibers contains orientation-induced crystalline structure when fibers cool down and solidify. In other words, PE nanofibers are usually considered as semi-crystalline nanofibers. As an another commonly used polymer, most polystyrene (PS) is amorphous and have brittle mechanical response at their bulk state. When the size of the polymer scales down to nanometer, like PS nanofiber, the mechanical responses change dis-

tinctly. Unlike PE nanofibers, PS nanofibers are usually fabricated at room temperature, and the final as-spun fiber is in an amorphous state. PS nanofibers behave ductile with enhanced modulus and strength when their diameters drop down below the certain "onset" dimension, which might be closely related to the molecular weight of their composite chains. Such an ability of improving ductility and mechanical behavior simultaneously makes nanofibers a promising composite for functional materials, such as armor fabrics and scaffolds in tissue engineering [38–40]. From another perspective, with the understanding of the "onset" mechanism, one can use nanofibers to design applications for target properties from a bottom-up manner with the choices of proper raw composite and external environment [41, 42].

In general, the mechanism and the corresponding structure variation when the size of the nanofiber drops are still not quite clear. The foremost hypothesis about this diameter dependence is the change of inside polymeric chain orientation, the layered core-shell structure in nanofiber, as well as the crystallinity degree of the fiber [43, 44]. For orientation, Saeed et al. found the signs of anisotropy (5% - 20%) along the electrospun PS fiber axial direction through small-angle neutron scattering (SANS) technique [45]. Arinstein et al. observed a linear increase of orientation degree of crystallites for Nylon 6.6 nanofibers [46]. Papkov and his co-workers reported simultaneously strong and tough polyacrylonitrile (PAN) nanofiber which the major property improvement is observed under ultrafine diameter (< 250 nm).[47] Regarding fiber core-shell structure, contrary models have been proposed to describe the density and chain orientation distribution. The results by Urszula et al. indicated the oriented polymer chains are majorly located in the shell area of the fiber [48], while Andrea and their co-workers showed the nanofiber might have a dense core with aligned chains [49]. In addition, the pioneering work by Vao-soongnern et al. reported the structural properties at the molecular level of polymer chains inside nanofibers [50, 51]. On the other hand, the

morphology of the fiber (whether they have crystalline or amorphous microstructure), also plays an important role in their mechanical properties. For crystalline or semi-crystalline nanofiber, typically, the modulus and strength can be enhanced after annealing since the polymer chain re-orient and form crystal structure when the fiber is heat treated [45, 52].

Due to the ultrafine dimension of the nanofiber, bundles of nanofibers are usually needed for examining the microstructure, including chain orientation and crystal structure. The limitation of requiring bundles is the relatively high noise-to-signal ratio. In addition, when examining the alignment, it is hard for the experimental technologies to distinguish between the orientations of the inside polymeric chains and the orientation of nanofibers itself. Additionally, with the bundle, an average value of nanofiber diameter is utilized while the actual values might be dispersed, which may result in most of the signals come from thick fiber and thus lead to a biased result [53].

To evaluate the degree of nanofiber crystallinity experimentally, the typical method is X-ray diffraction (XRD) which relies on the specific diffraction pattern generated by the interaction of X-ray with crystal structures. However, for amorphous nanofibers, such as fibers fabricated using atactic polystyrene (PS) solution, although the PS backbone is oriented when nanofiber formed, the overall amorphous structure cannot show significant pattern under X-ray. As far as we know, there are a few emerging technologies that might be able to capture the backbone orientation. However, no single technologies currently could provide a comprehensive understanding of the onsite mechanism in ultrafine amorphous nanofibers.

Furthermore, the final state of electrospun or drawing suspended nanofibers remains non-equilibrium due to the fast solvent evaporation [54, 55]. Because of the stretching force during fabrication, the length of bonds on the backbone may have some tiny elongations and then are locked when fibers solidify. Since the deformation of the covalent bonds can supply a very strong force which is orders higher than van der Waals forces, the pre-elongated bonds

in the as-spun nanofibers would result in a significant variation in the modulus. However, to the best of our knowledge, so far present experimental technologies cannot directly perceive this type of slight elongation at covalent bond level.

The experimental dilemmas make molecular dynamics simulation an excellent alternative way to investigate the nanofiber structure and mechanism [56, 57]. As a broadly used computational tool in nanoscale, molecular dynamics simulation can track the position of every atom during the entire simulation time, which makes the evaluation of chain orientation and local morphologies in nanofiber much painless compared to experimental methods. Moreover, although the molecular dynamics simulation have difficulties on reaching very large system size which is attributed to the limited computational resources, by using the coarse-graining (CG) model and implementing periodic boundary condition in fiber axial direction, we are able to simulate PS nanofiber with diameters comparable to the actual experimental scale.

In this chapter, we study the diameter dependence and corresponding onset mechanism of individual nanofiber of atactic PS via molecular dynamics simulation. A recently developed CG potential force field [58], which is thermomechanically consistent and temperature transferable, is used to emulate PS nanofibers with diameters ranged from 150 nm to 300 nm. From our model, we observed the exponential increase of young's modulus and linear increase of ultimate strength when fiber diameters decrease. The effect of the molecular weight of the PS chain on diameter dependence is also investigated. We further extract the chain orientation parameter and average backbone bond length and then disassemble the effect of them on the modulus and strength. Finally, after comparing with experimental results, we propose a schematic model describing the onset mechanism on diameter dependent mechanical response of amorphous nanofibers.

2.2.2 Simulation method

All simulations are performed by using the open-source molecular dynamics package, LAMMPS [59]. We implement the recently developed two-bead type CG methodology to build our PS nanofiber systems. Unlike the traditional one-bead type CG method, this mapping scheme distinguishes the backbone beads and side-chain beads. As shown in Figure 2.12a, the backbone bead (in magenta) is centered at the alkyl carbon bonded to the phenyl ring, while the center of the side-chain bead (in cyan) is located at the center of mass of the phenyl ring. In this way, the bond structure is more similar to the full atomistic model and provides a physically consistent molecular orientation when the fiber is forming. Detailed methodology and the functional form of the potential force field can be found in Ref [58].

As shown in Figure 2.12b, the PS nanofibers are made through the following steps. First, the initial structure is built by a self-avoiding random walk method within a rectangular box. The dimensions of the box (side lengths) are carefully chosen in order to make all long polymeric chains have enough space to walk randomly without overlap. Here, we utilize the concept of normalized diameter D_{norm}, defined as the ratio of fiber diameter to the root mean squared end-to-end distance of a single unperturbed polymer chain at bulk state R^*_{ee} [60, 61], to help with the selection of the size of the initial rectangular box. Noted that at melt state, R^*_{ee} is positively proportional to the molecular weight (MW) of individual polymeric chain, $R^*_{ee} \propto MW^{1/2}$. We take $D_{norm} > 13$ for the criteria that amorphous bulk-like state occurred. In this study, the nanofibers are composed of atactic PS chains with MW of 300,000 (1333 chains in the system) and 600,000 g/mol (667 chains in the system), separately. To meet the criteria, the side length of rectangular boxes is required no less than 500 nm for the MW of 300,000 g/mol and 700 nm for 600,000 g/mol. Next, the randomly orientated polymer chains inside the rectangular volume with the periodic boundary condition in x, y and z-direction are equilibrated at 750 K for 4 ns, followed by two annealing process (each takes 1 ns) from

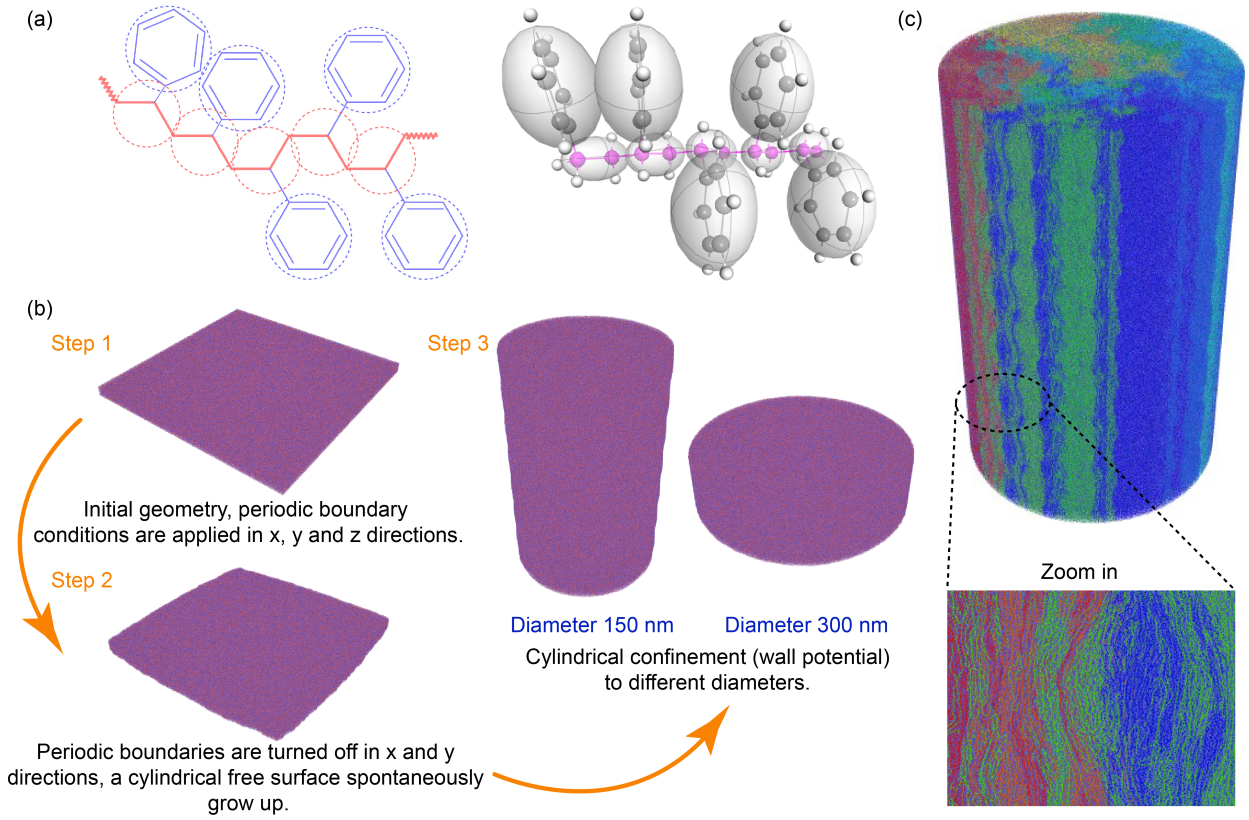

Figure 2.12: Schematics of (a) Polystyrene atomistic to coarse-graining mapping scheme, (b) the fabricating procedure of PS nanofibers with different diameters via molecular dynamics simulation, (c) the rendered nanofiber showing the morphology of chain distribution of modeled nanofiber.

750 K to 300 K.

Second, the periodic boundary condition is turned off in x and y directions. In the meantime, the simulation box expands twice in these directions compared to the original one, such that the molecules no longer interact with their counterparts in the expanded directions. Now, the periodic boundary condition is only applied in the z-direction (nanofiber axial direction). Under these conditions, the temperature firstly increases from 300 K to 750 K, and then the nanofiber is equilibrated at 750 K for 4 ns. A cylindrically free surface would spontaneously grow up upon further equilibration. After the cylindrical shape formed, the nanofibers are

cool down to 300 K again.

Third, to control the final diameters of the nanofibers, a cylindrical wall potential is applied. As started, the temperature is increased back to 750 K, and then an NPT ensemble is followed to maintain the temperature at 750 K with zero pressure in the z-direction. During this NPT dynamics, the diameter of the cylindrical confinement slowly decreases down to different values while the nanofiber is allowed to adjust their density by changing the length in the z-direction. After the temperature drops down to 300 K, the glassy nanofibers with different diameters are obtained and the wall confinement is removed. An NVT ensemble is then performed at 300 K for 1 ns. Subsequently, an NPT ensemble is run to remove the internal stress in the fiber axis before the uniaxial tensile test is performed (The density profiles of every nanofiber system are in Figure 2.13). Last step, the stress-strain relationship of the nanofibers is obtained by tensile tests along z-direction that the simulation box is deformed at a constant engineering strain rate under the NVT ensemble of 300 K. The engineering rate is $2.5 \times 10^9\ s^{-1}$ and the temperature damping factor is 400 fs. For the calculation of stress in the nanofiber, per-atom stress tensors are firstly calculated and summed for all atoms, since per-atom array values are in the form of pressure*volume, the values are divided by the volume of the nanofiber to get actual stress in the nanofiber along the z-direction. For every nanofiber system, the entire simulation procedures (including steps 1, 2 and 3) take around 154 hours on 384 CPUs.

There might be slight concern about the geometry of the nanofibers in Figure 2.12b, since the 300 nm nanofiber looks rather short than a continuously long fiber. The reason is due to the limited computational resource, the maximum simulation system we can achieve contains 8,000,000 beads which lead to an upper limit on the volume of the system. For 300 nm nanofiber, the rather large diameter constrains the length of the fiber we could carry out. In theory, periodic boundary condition on axis means that nanofibers are infinitely long. To

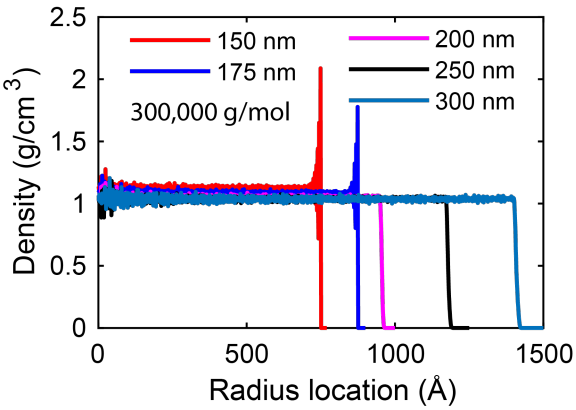

Figure 2.13: Density vs. radius profile from the center to the edge of the nanofiber with the molecular weight of 300,000 g/mol. For 150 nm and 175 nm nanofibers, the density oscillation at the edge is because of the confinement. The increased fluctuation in density near r 0 is a consequence of poorer statistical sampling.

validate there is no influence on the stress-strain response, fibers with the same diameter but different lengths are tensile tested under the same strain rate. The result (in Figure 2.14) shows that the length of the fiber doesn't affect the stress-strain response as long as the periodic boundary condition in the z-direction is applied.

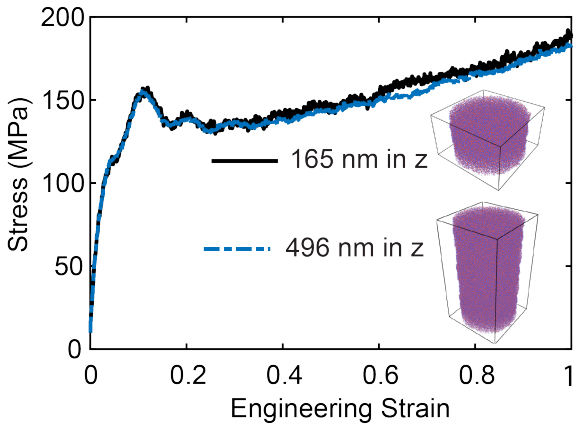

Figure 2.14: Stress-strain response for amorphous PS nanofiber of 165 nm and 495 nm long in the z-direction with the representative snapshots of 30 nm amorphous PS nanofiber in different lengths inserted.

In Figure 2.12c, different PS chains are rendered by different colors, we found that chains have a trend of orienting parallel to the fiber axis. It is worth mentioning that the degree

of orientation is closely associated with nanofiber diameters. Detailed results and discussion will be provided in the next section.

2.2.3 Normalized diameter

The nanofibers with polymer chains of MW of 300,000 g/mol and diameters ranged from 150 nm to 300 nm were molded. The fibers with the chains of 600,000 g/mol and diameters ranged from 210 nm to 300 nm were also prepared as a comparison. Figure 2.15 and Table 2.1 show the stress-strain curves and corresponding mechanical properties of the nanofibers.

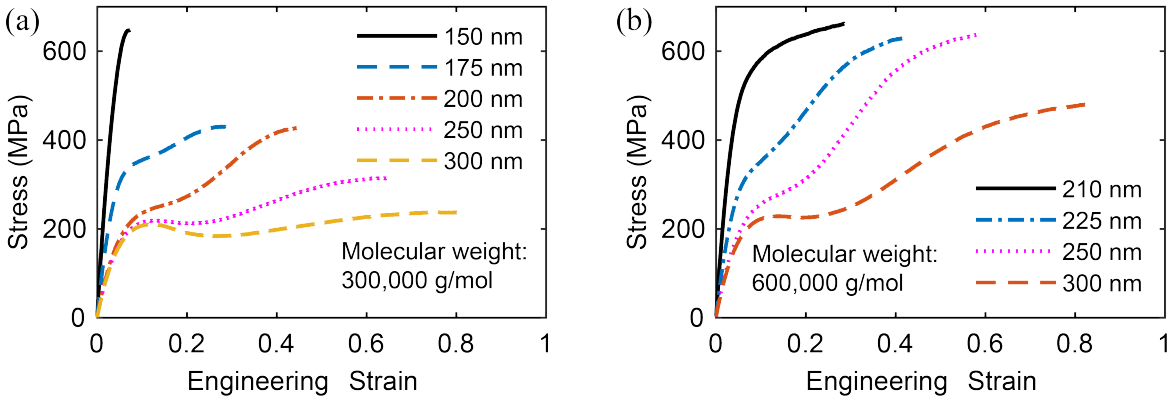

Figure 2.15: Stress vs. strain curve for PS nanofibers of (a) MW = 300,000 g/mol with diameters ranged from 150 nm to 300 nm and (b) MW = 600,000 g/mol with diameters ranged from 210 nm to 300 nm (we think it is much more insightful to plot the stress-strain curve until the maximum stress/load, because in experiment the post-peak load cannot be captured experimentally, and it lead to an instability. For readers' reference, the raw data of the stress-strain curves are shown in Figure 2.16 and the snapshots of nanofibers during tensile tests are provided in Figure 2.17).

Focusing on the nanofibers with diameters ranged from 200 nm to 300 nm, it is clearly noted that the nanofibers with the same diameter, but different lengths of composite polymeric chains have different mechanical responses. Such a variation can be linked to the normalized diameter in the confined polymeric system. As briefly mentioned in the simulation method part, D_norm is the ratio of fiber initial diameter ($D_{initial}$) to the root mean squared of

Table 2.1: Mechanical properties of simulated PS nanofiber systems.

Molecular weight (g/mol)	Nanofiber diameter (nm)	Young's modulus (GPa)	Strain at break (Mpa)	Stress at break
300,000	150	11.72	0.07	647.30
300,000	175	6.09	0.29	430.70
300,000	200	3.56	0.45	427.37
300,000	250	3.34	0.65	314.15
300,000	300	3.25	0.81	236.14
600,000	210	9.64	0.28	661.85
600,000	225	5.62	0.42	630.63
600,000	250	3.78	0.58	636.66
600,000	300	3.43	0.84	482.45

chain end-to-end distance, R^*_{ee}. Based on the works of Fetters et al. [62, 63], we have $R^*_{ee} = \sqrt{0.437MW}$. Need to note that R^*_{ee} here is the end-to-end distance for unperturbed chains in polymer melts. It doesn't refer to the specific end-to-end distance for polymeric chains in the confined nanofiber system. The calculated D_{norm} for the nanofibers in our case are listed in Table 2.2 below.

Table 2.2: The parameters used in the calculation of normalized diameters of PS nanofibers.

Molecular weight (g/mol)	Nanofiber diameter ($D_{initial}$,nm)	End-to-end distance (R_{ee},nm)	Normalized Diameter (D_{norm},nm)
300,000	150	36.2	4.1
300,000	200	36.2	5.5
300,000	250	36.2	6.9
300,000	300	36.2	8.3
600,000	210	51.2	4.1
600,000	250	51.2	4.9
600,000	300	51.2	5.9

From Figure 2.15, nanofibers demonstrate higher ultimate strength when their diameters decrease, no matter what the molecular weight of their composite chains is. However, comparing Figure 2.15a with Figure 2.15b, the mechanical performance of the same sized nanofibers

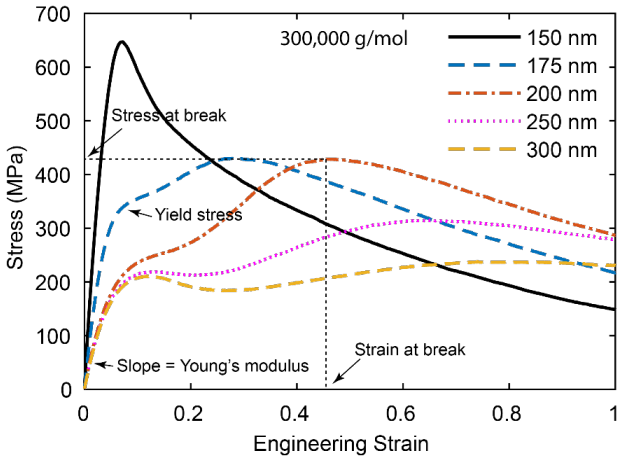

Figure 2.16: The stress-strain curve for nanofibers of chains of 300,000 g/mol without smoothing. The smoothness is simply a result of the very large system sizes. In the Figure, we think it is much more insightful to plot the stress-strain curve until the maximum stress/load, because in experiment the post-peak load cannot be captured experimentally, and it led to an instability

behaves distinctively when they are made by different lengths of PS chains. When the diameters are fixed, the increase of young's modulus and strength of the fibers can be attributed to the larger molecular weight of their composite chain. In other words, fibers with the same size but made by the longer polymeric chain are more confined. Associated with the normalized diameter, the smaller value of D_{norm} imply stronger molecular confinement in individual nanofiber, which will also lead to distinguished chain conformation compared to the chains in the bulk state.

A clearer understanding of the relationship between D_{norm} and mechanical properties of nanofibers emerge upon grouping the results of Figure 2.15 and Table 2.2. When the values of D_{norm} are close to each other, as compared between 200 nm nanofiber with MW=300,000 g/-mol and 300 nm nanofiber with MW=600,000 g/mol ($D_{norm} > 5$ in both cases), they exhibit quantitatively similar modulus and strength. Notably, when $D_{norm} > 5$, the nanofibers show a pronounced stress plateau region between the elastic extension and post-strain-hardening regime. As D_{norm} decreases, the nanofibers tend that the stress sharply increases at the

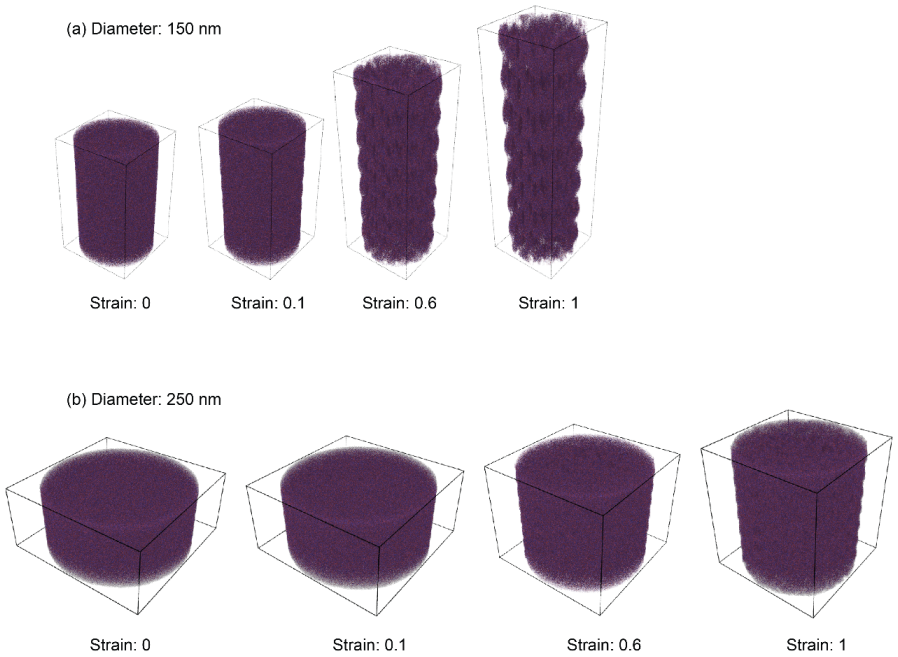

Figure 2.17: The snapshots for 150 nm and 250 nm PS nanofiber during tensile tests, periodic images in the z-direction are included for clarity. The boxes here are drawn as guides to the eye (It is not the simulation box used in the MD simulation).

initial strain stage until nanofiber breaks, thus there is no stable necking region existing. Therefore, it is worth to say that although the parameter D_{norm} cannot provide any detailed information about molecular orientation or bond length, D_{norm} is still a representative factor that can evaluate the status of spatial confinement and expect the mechanical response of the nanofibers.

2.2.4 Molecular orientation

To quantify molecular chain orientation strictly, we introduce the Herman orientation parameter, P_2 as calculated by equation 1, where, θ_i is the angle between z-direction and the vector from bead i-1 to nearby bead i+1 along the same backbone. The orientation parameter takes the value of 0 for an entire amorphous distribution, 1 for the perfect parallel

alignment between chains and -1/2 when chains are perpendicular to each other.

$$\langle P_2 \rangle = \frac{3}{2} \langle \cos^2 \ \theta_i \rangle - \frac{1}{2}$$

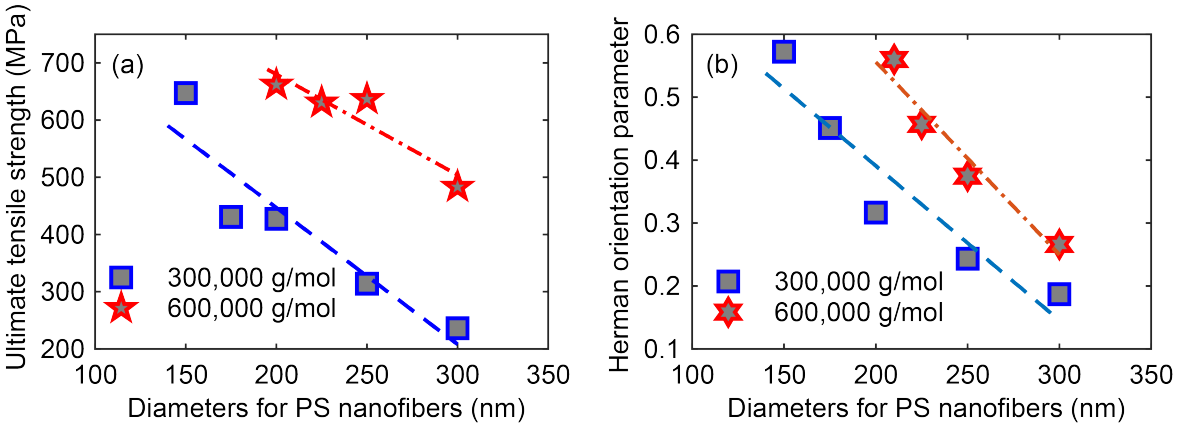

Figure 2.18: The correlation of (a) nanofiber diameter vs. ultimate tensile strength (MW = 300,000 g/mol and MW = 600,000 g/mol) and (b) corresponding nanofiber diameter vs. chain orientation parameter (MW = 300,000 g/mol MW = 600,000 g/mol).

It can be observed in Figure 2.18 that the orientation parameter increases from 0.2 to 0.6 when diameter drops, which indicates chains have aligned order along fiber axial direction. The molecular orientation of both nanofibers (MW=300,000 and MW=600,000) have similarly linear evolution patterns. Interestingly, by extracting the values of ultimate tensile strength and group them together, we find the correlation between diameter and strength is also linear. The analogous evolving pattern of strength and orientation as a function of diameter can be explained by the following reasons. During the tensile test, the mechanical response is mainly determined by the combination of van der Waals forces and resistant forces provided by covalent bonds. The resisting forces by chemical bonds are much stronger than the van der Waals forces, actually it is the dominant force determining the overall stress response. As we know for polymers, the tensile stretching process would lead to the rearrangement of the chain orientation [64]. For amorphous PS, the initial chain orientation

parameter is 0, and the stress response mostly relies on the intermolecular forces. As the deformation continues, chains aligned and disentangled, so the stress increases until fractures occur due to chain disentanglement. For PS nanofiber, the stretch of the oriented structure leads to the deformation of covalent bonds from a very early stage. Therefore, higher chain alignment makes for larger ultimate strength. On the other hand, because of the disentanglement from the aligned structure, nanofibers with a larger value of chain orientation parameter exhibit lower breaking strain.

Contradicting to some existing explanations about the mechanism nanofiber size effect, from our results, although the molecular orientation has a significant effect on the ultimate strength, it plays a relatively less important role in determining the young's modulus of the nanofiber. Detailed discussion is presented in the following sections.

2.2.5 Young's moduli

As a typical size-effect of nanofiber, the young's modulus increases exponentially when the diameter of the nanofibers drops down below the "onsite" diameter (shown in figure 2.19). The young's moduli along the nanofiber axis are determined by the stress-strain curve in the elastic region from Figure 2.15. We observed an increment from 3 GPa to 12 GPa when diameter drops from 300 nm to 150 nm for nanofibers with the MW of 300,000 g/mol. As a counterpart, the young's moduli of nanofibers (MW=600,000 g/mol) rise from 3 GPa to 10 GPa as the diameters decrease from 300 nm to 210 nm. It needs to be mentioned that when the diameter of the nanofibers (MW=600,000 g/mol) drops below 210 nm, the geometry of the nanofiber system starts to become unstable. This is the reason why the result shown here does not cover the same diameter range.

In our cases, the onset diameters are around 200 nm and 250 nm for the nanofiber of PS

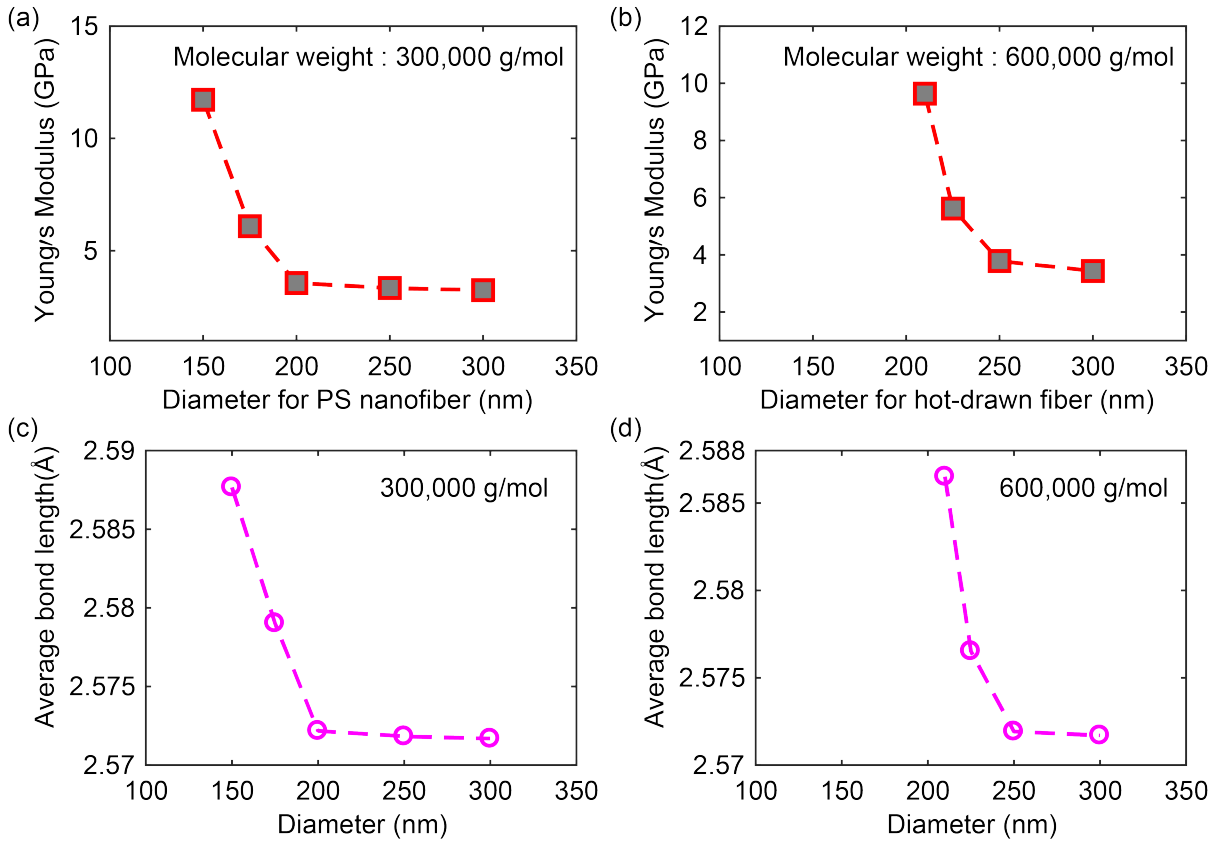

Figure 2.19: The correlation of nanofiber diameter vs. Young's modulus for fibers with (a) MW = 300,000 g/mol and (b) MW = 600,000 g/mol. (c) Diameter vs. the average length of bonds along PS backbone (MW = 300,000 g/mol), (d) diameter vs. bond length (MW = 600,000 g/mol).

MW of 300,000 and 600,000 g/mol respectively. We can claim that the onset diameters are associated with the MW. The higher the MW of PS we used, the larger the onset diameter would be. This statement is qualitatively consistent with the experimental results reported by Marie and co-workers [43], they used high molecular weights of PS chain to make the fiber and then found the nanofibers have an impressively large onset diameter.

In order to rationalize the origin of the increase of Young's modulus, the change of average bond length between the backbone beads (beads type A) is tracked. Surprisingly, the up-turn points for bond length increment are around 200 nm and 250 nm for two nanofibers

separately, which is perfectly consistent with the onset diameter of Young's modulus. As briefly mentioned in section 2.2.4, there were some explanations stating that the dominant reason for the change of Young's modulus is the chain alignment. However, from our studies, we think the most direct reason for it is the bond elongation along the backbone. By analyzing Figure 2.18 and Figure 2.19 together, since the increase of the chain orientation parameter is rather linear than exponential, it cannot thoroughly explain why the trend of the young's modulus climbing sharply after a certain point. A proper picture of the onset mechanism might be the interplay of chain alignment and bond elongation. During the fiber fabrication process, the polymeric chain starts to be aligned and disentangled due to the stretching or drawing force. To a certain point, parts of the aligned polymer chains would have a high chance of being directly extended. On account of the very fast evaporation, some extended chains are locked and staying in a non-equilibrium state after solidification. When the uniaxial tensile test is performed, the resisting force from the elongated covalent bonds is extremely strong. Thus it results in the rapid growth of the stress response at the early strain stage. To make sure there is no systematic "drift" during the calculation of the bond length and provided clearer evidence that the bond length is the most direct reason for the enhancement of Young's modulus, the plot of the evolution of bond length vs. time at 300 K before the tensile test is provided in Figure 2.20, and the change of bond length during tensile stretching is shown in Figure 2.21.

2.2.6 The onset mechanism for nanofiber diameter dependence

Our aim now is to cross-validate the specific onsite mechanism for the diameter dependent modulus and strength of amorphous nanofiber. From Figure 2.22a and Figure 2.22b, experimental results are shown here in order to compare with our simulation results. Xu et al. reported the stress-strain curves of as-spun amorphous polycarbonate (PC) nanofibers

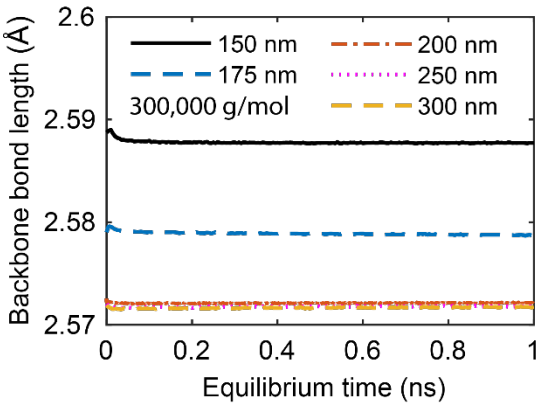

Figure 2.20: The evolution of backbone bond length vs. equilibrium time at 300 K (right before the tensile test).

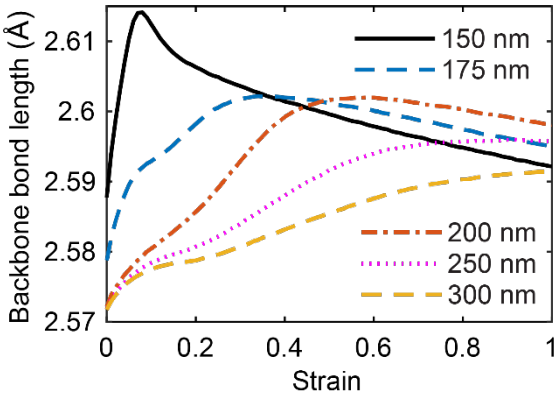

Figure 2.21: The evolution of backbone bond length vs. strain during the tensile test.

[65]. Kolluru and co-workers demonstrate the mechanical response of annealed amorphous PS nanofibers [61]. It is noteworthy that the significant distinction between the nanofibers before and after annealing is the change of Young's modulus. For as-spun nanofiber, the young's modulus sharply increases as diameter decreases. However, the values of Young's modulus fall closely for annealed nanofibers regardless of thickness. One thing we need to mention before we go further is that, unlike the crystalline nanofibers that the annealing process will trigger the formation of crystal phase and then enhance the overall mechanical properties of them, the annealing process may lower the mechanical properties of amorphous nanofiber since high temperature makes the inside chains re-oriented.

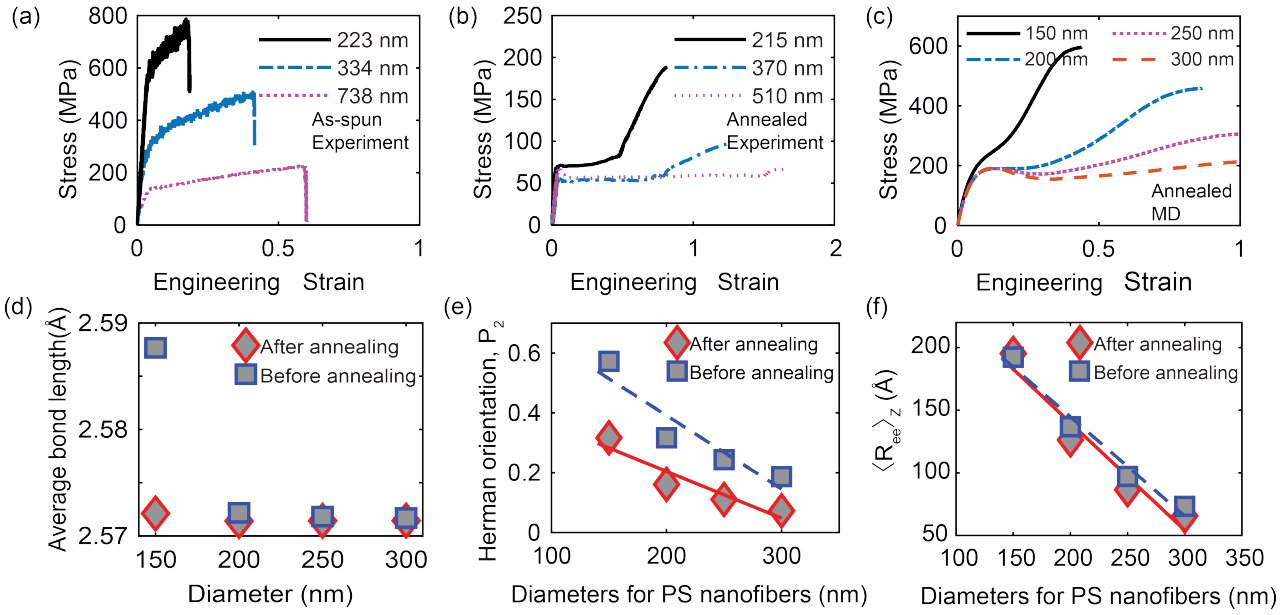

Figure 2.22: Stress-strain curves for (a) as-spun amorphous PC nanofibers and (b) annealed amorphous PS nanofibers. (c) The stress-strain relationship of annealed PS fiber by MD simulation and corresponding (d) bond length, (e) chain orientation parameter, and (f) end-to-end distance extracted from the as-spun and the annealed nanofiber.

By performing MD simulation, the as-spun PS nanofiber of MW=300,000 g/mol (stress-strain curve in Figure 2.15a) was annealed. The nanofibers are heated up from 300 K to 750 K in 1 ns, then an NPT ensemble is performed at 750 K for 4 ns with zero pressure in fiber axial direction, finally the temperature drops back to 300 K in 1 ns. The corresponding stress-strain curves are shown in Figure 2.22c while Figure 2.22d and Figure 2.22e demonstrate the bond and information of the annealed nanofibers. We found the stress-strain curve trend from MD simulation (Figure 2.22c) is qualitatively consistent with the experimental results (Figure 2.22b). The variation in specific values comes from the high strain rate used in the tensile test via MD simulation. We further confirmed that the bond length of all nanofibers with different thicknesses is returned back to its equilibrium length (Figure 2.22d). The chain orientation parameter and fiber diameter still have a linear correlation for annealed fiber, but certain values are relatively lower than in as-spun nanofibers because partial relaxation

happened during the annealing process. The end-to-end distance of chains in these confined nanofiber systems (along the z-direction), $\langle R_{ee} \rangle_z$, is presented in Figure 2.22f. Contrary to the bond length, $\langle R_{ee} \rangle_z$ shows a linear correlation with respect to the nanofiber diameter before and after annealing.

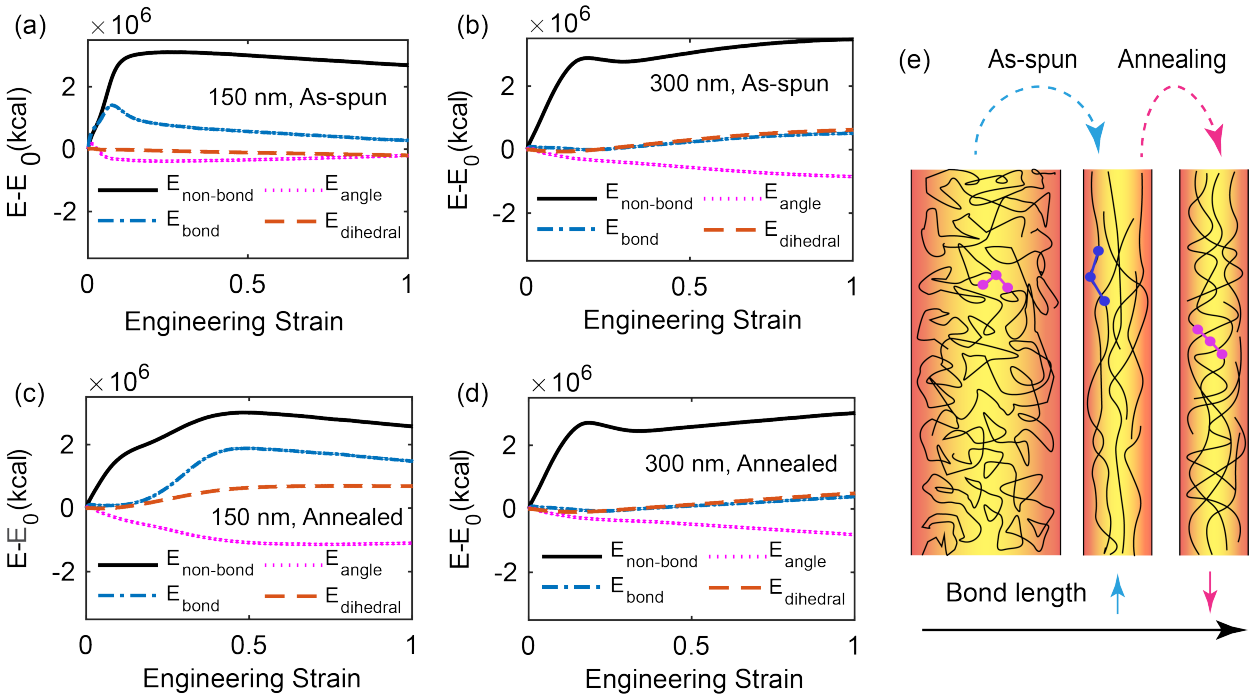

Figure 2.23: The evolution of the bond, angle and dihedral energies during the tensile test for (a) 150 nm as-spun nanofiber, (b) 300 nm as-spun nanofiber, (c) 150 nm annealed nanofiber and (d) 300 nm annealed nanofiber. (e) The schematic representation of the annealing mechanism regarding the molecular orientation and backbone bonds length in the PS nanofiber.

To further understand the roles of these descriptors (bond length, chain orientation and end-to-end distance) during the nanofiber annealing process, the evolutions of energetic terms during pulling are shown in Figures 2.23a to 2.23d. For 150 nm as-spun nanofiber, the bond energy exhibit a pronounced increase at the elastic stage (strain < 0.1). However, after the annealing, the bond energy is kept almost flat at the initial pulling stage and then smoothly grows up. Considering Figure 2.23 and Figure 2.22f together, we find the significant drop of

Young's modulus has few connections with the chain orientation, but the bond energy (bond length) plays a much more important role. In general, an overall picture of the microstructure evolution of amorphous nanofibers is sketched to present the proper chain organization before and after the annealing procedure. In Figure 2.23e, the initial thick fibers are composed of isotropic disordered chains with bonds around equilibrium length. As the fiber diameter is reduced through drawing or electrospinning process, the inside chains will be aligned along the fiber axis, and some of the bonds will be extended out of its original equilibrium length (middle of Figure 2.23e). Such kinds of solidified as-spun nanofibers will show an increase in modulus and strength, simultaneously. After annealing, the bond length will return to the equilibrium state. Meanwhile, the overall chain alignment reduces as well, but might still be in a more oriented state than the state in thick fiber (or bulk state).

2.2.7 Conclusion

The diameter dependent mechanical properties of individual PS nanofiber with MW in the range of 300,000-600,000 g/mol and diameter of 150 nm to 300 nm were studied via molecular dynamics simulation. To the best of our knowledge, it is the first time MD simulation study of PS nanofiber has reached the size directly comparable to the one can make in experiments. We introduced the parameter D_{norm} to represent the extent of chain confinement in nanofiber and found the stress responses of the nanofiber not only have diameter dependence, but they are also associated with the molecular weight. PS nanofibers with close values of D_{norm} follow master curves that capture the effect of diameter and chain length scale on the stress-strain relationship for individual PS nanofiber. We also investigated the interplay of chain orientation and bond length on nanofiber mechanical properties. An increasing chain alignment when reducing nanofiber diameter increases the ultimate strength of nanofibers. The exponential increase of Young's modulus is more directly originated from the increase

of covalent backbone bond length rather than the linear increase of molecular orientation. To validate this statement, experimental stress-strain results of as-spun fibers and annealed fibers were presented and also the modeled PS nanofibers with MW of 300,000 g/mol were adopted for annealing via MD simulation. The stress-strain evolution pattern of PS nanofiber with and without annealing from simulation excellently fits with the experimental results. By extracting the morphology information of this annealed nanofiber from simulation, it is convinced that both chain orientation and bond length will affect the modulus and strength of PS nanofiber, but the backbone bond length plays a more significant role on determining Young's modulus of PS (amorphous) nanofiber.

Chapter 3

Shape memory polymers in HIFU fields

3.1 Introduction

Size effects of polymeric materials are not limited to the pure mechanical response alone. For instance, when the functional polymers (shape memory polymers in this case) is in a external stimulus field, their thermomechanical response is also highly size-related. In the field of medicine, controlled drug delivery technology has received extensive attention during the past three decades [66], mainly because of numerous advantages of this technology compared to the conventional methods [67]. Despite significant recent achievements, controlled drug releasing systems still face major challenges in practice including chemical issues involved in synthesizing biocompatible drug containers, reducing the releasing time of drugs in the body, delivering the drugs at a targeted location and utilizing a safe and noninvasive trigger to initiate drug release [68, 69]. It is found the shape memory polymers (SMPs) have a good feasibility for designing CCD system. So in this chapter, we leverage the experimental, analytical and computational techniques to investigate the feasibility of using shape memory polymers (SMPs) and high-intensity focused ultrasound (HIFU) for designing a CDD system. The design is used in a conceptual novel mechanism for simultaneously opening the drug container and pushing the particles out, which will significantly improve the rate of drug

releasing at a targeted location.

Smart materials are engineering materials that have one or more properties, which can be changed by external stimuli such as temperature, electric field, magnetic field or stress [70–73]. SMPs are a relatively new class of smart materials that have the ability of storing a temporary shape and returning to their permanent or original shape [74] when subjected to external stimuli such as heat, light or ultrasound [75–79]. Compared to other shape memory materials such as shape memory alloys [80–82] and shape memory ceramics [83], SMPs are light weight, inexpensive, and can recover large deformations [84–86] in a controlled manner. Development of SMP-based devices for medical applications such as stents for cardiovascular systems and self-tightening sutures has gained a lot of attention recently [68, 74, 87, 88]. Xue et al. [89] developed self-expandable stents which exhibited shape recovery at body temperature at a much faster rate compared to the best known self-expandable stents. Because of these advantages, during the past decade, SMPs have received increased interest in biomedical applications [90] and advancing CDD systems [91]. At present, the commercially available drug release devices still lack the capability of delivering drugs in a spatially and temporally controlled manner [92]. The combination of SMPs and CDD leads us to a multidisciplinary research in order to reduce the drug side effects in patient body and frequency of taking drugs by patient, which means having more reliable and accurate treatment.

The shape memory effect of SMPs relies heavily on the external trigger provided. For use in in vivo applications, thermal activation through body heat has often been relied upon to trigger shape recovery [69]. However, there is a need for more flexible stimuli as compared to fixed body heat temperature. Consequently, noninvasive triggers such as light [93–95], magnetic field [96, 97], electrical field [98, 99] and radiofrequency wave [97] have been employed. These triggers require special components such as magnetic or florescent particles

to generate response, which can compromise the biodegradability and biocompatibility of SMPs. Thus, use of a safer and effective trigger is of utmost importance to achieve remotely controlled shape recovery. The use of FU an as external stimulus fulfils the above criteria. The underlying mechanism involves focusing ultrasound into a tight spot in domain area of millimeter scale, which causes selective and controlled heating of the medium at the spot. This localized heating also eliminates the need of incorporating special or responsive particles in the medium as shape deformation occurs due to heating caused by viscous shearing oscillation of molecules under ultrasound.

Employing high-intensity FU has been researched for biomedical purposes for many years [100, 101]. The higher penetrating ability of acoustic waves as compared to light has been used for selective tissue necrosis in controlled volumes. Studies have been conducted reporting the use of ultrasound in acoustic energy transfer systems [102–105] and for drug delivery [106–108] especially from polyelectrolyte micro-containers [109], multilayered capsules [107, 110] and polymer micelles [111–114]. In their study, Kost et al. [108] irradiated ultrasound on a polymer matrix for releasing drugs entrapped in the matrix. Liu et al. [115] and Han et al. [116] conducted proof-of-concept experiments using FU to demonstrate shape recovery process of SMPs and obtain various intermediate shapes with the help of FU. The research done in recent years demonstrating the effect of FU on shape recovery behavior of polymers has been experimental in nature. The very limited literature lacks fully coupled modeling efforts to analytically solve the underlying problem and optimize a SMP-based CDD design.

In this chapter, for the first time, we perform a multiphysics analytical and numerical modeling to optimize the design of a SMP-based drug delivery system and quantify its activation under FU. This model provides the foundation for designing and testing SMP capsules, an example of which is schematically shown in Figure. 1.Therefore, by using HIFU we are able

to release the loaded drug in a switchable manner.

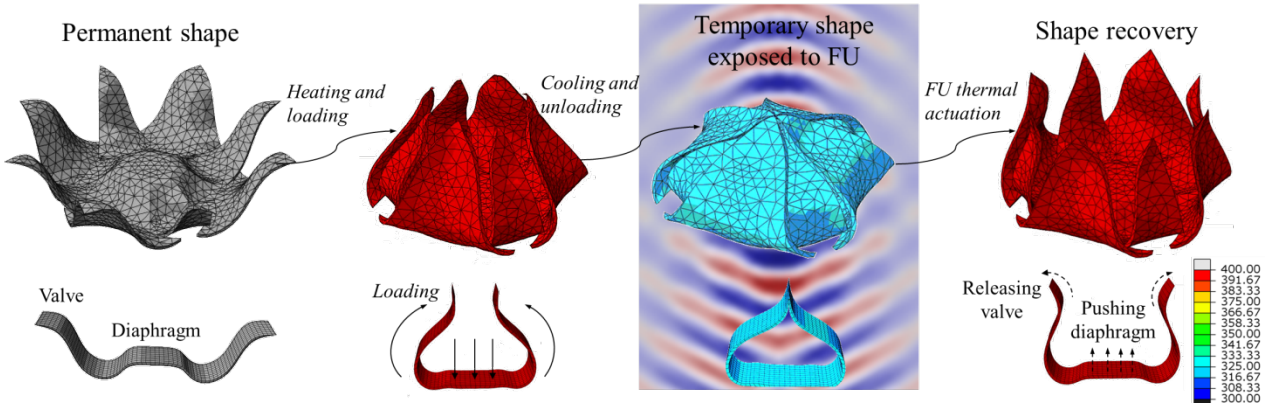

Figure 3.1: 3D (top) and 2D (bottom) schematic representation of the concept for shape memory polymer (SMP) container under focused ultrasound (FU) irradiation. From left to right: the SMP container with a permanent shape is loaded with the particles then heated and deformed to a temporary shape. When delivered to the desired location, the container undergoes shape recovery under FU-induced thermal actuation and releases the loaded particles.

In this chapter, we implement a comprehensive set of analytical, numerical and experimental studies to design, analyze and test a coupled FU and SMP representative mechanism at a millimeter-scale framework. The model studies the acoustic-structure interaction of FU with SMP-based filaments to establish the relationship between input parameters (such as input power and frequency) with the acoustic, thermal and stress fields and shape recovery of SMPs. Medium properties such as absorption and nonlinearity, which significantly affect the pressure field of a propagative wave [117], are studied to analyze their influence on the shape memory behavior of polymer. The analytical-numerical model is validated through experiments using a high-intensity focused transducer in a water tank. Various concepts can be considered for the design of a SMP container subjected to FU, similar to the example shown in Figure 3.1, while the modeling effort is focused on the special case of a filament, as fundamental element of any container, stimulated by FU.

3.2 Theory

To design a SMP-based drug delivery system, development of a robust theoretical model which predicts the HIFU induced acoustic and thermal fields and subsequent mechanical behavior of SMP is essential. In this work, we present multiphysics acoustic-thermoelastic modeling for ultrasound actuation of SMP filaments. The analytical-numerical model is divided into three interconnected parts. The first part studies the focused acoustic pressure field in a multilayer domain which includes a SMP filament submerged in fluid. The temperature distribution of the polymer obtained from the second part is given to the third part which provides a framework to predict the mechanical stresses developed in SMPs and consequent shape recovery. A mechanical model is formulated by a compressible neo-Hookean constitutive equation, which assumes the SMPs behave as a thermoelastic material and predicts the thermally induced shape memory effect under FU. The constitutive model is numerically implemented in a user material subroutine (UMAT) in ABAQUS to model the deformation of the filament.

The effects of focused ultrasound on soft tissues are well documented [118–120]. A mathematical formulation to analyze the effects of ultrasound on tissues is given by Penne's Bioheat equation which models the transfer of heat and generation of thermal field in the tissue domain. In this work, similar framework is used to evaluate the temperature rise of the polymer as a result of FU heating. The modified Penne's Bioheat equation for SMP is given as [121],

$$\rho C_{hm} \frac{\partial T}{\partial t} = \kappa \nabla^2 T + H$$

where heating rate H is given by,

$$H = \frac{1}{\rho c_m} \sum_{n=1}^{k} Re(\bar{a_n}) p_n$$

and ρ, C_{hm} and κ denote the density, specific heat capacity and thermal conductivity of polymer. Parameter c_m denotes the sound speed in polymer and denotes the pressure field associated with each harmonic predicted by KZK equation. The thermal equation is coupled with KZK equation through heating rate H. Heating rate takes into account the cumulative heating by all harmonics.

Having obtained the temperature distribution above, in this part, a SMP filament is modeled to predict the shape recovery process under focused ultrasound by applying the obtained thermal boundary conditions. SMPs are categorized as semi-crystalline shape memory polymers (CSMPs) and glassy shape memory polymers (GSMPs). GSMPs have both amorphous and glass regions, with defined as the glass transition temperature above which the SMPs exist in amorphous form. In this study, the selected constitutive model takes into account the stress-strain response which depends on thermal expansion of polymers to predict the glass transition of GSMPs [122–124]. The constitutive model involves four steps, the loading (amorphous phase), cooling (phase transition), unloading (glassy phase) and heating (phase transition) of the polymer filament. The constitutive model is numerically implemented in a user material subroutine (UMAT) in ABAQUS, a commercial finite-element software, to model the deformation and shape recovery of an L-shaped filament which is thermally activated by FU. The governing equations calculating the stresses during the whole cycle and the evolution rules for the glass volume fraction are given in the following [124].

SMPs above the glass transition temperature show the characteristics of an elastomer. The stress σ in the amorphous part of the SMPs is given as,

$$\sigma = -C_{10}I + \mu_a B_{k_a}$$

where c is the Lagrange multiplier due to the constraints of incompressibility, I is an identity

tensor, B_{k_a} is the left Cauchy stretch tensor and μ_a is the shear modulus of the amorphous phase. Here B_{k_a} is related to deformation gradient in amorphous phase, F_{k_a}, as $B_{k_a} = F_{k_a} {F_{k_a}}^T$. The stored energy function for the amorphous phase, Ψ_a is given as

$$\Psi_a = C_{10}(I_{Ca} - 3) + \frac{1}{D_1}(J_a - 1)^2$$

where $C_{10} = \mu_a/2$ and $D_1 = 2/K_a$ are the coefficients related to shear modulus and bulk modulus, , of the amorphous phase, respectively. Here $I_{C_a} = tr(B_{k_a})$ and J_a is the volume ratio that can be determined by $J_a = det(B_{k_a})^{1/2}$.

During cooling, as the temperature goes below the glass transition temperature, the glassy phase starts forming and both amorphous and glassy phase coexist at the same time. The stress for cooling phase of the cycle is given by

$$\sigma = -cI + (1-h)\mu_a B_{ka} + \mu_g h B_{k_g}$$

where μ_g is the shear modulus of the glassy phase and h is the glassy volume fraction. B_{kg} is left Cauchy stretch tensor which is related to deformation gradient in glassy phase, Ψ_g as,

$$\Psi_a = C_{20}(I_{C_g} - 3) + \frac{1}{D_2}(J_g - 1)^2$$

where C_{20} and $D_2 = 2/K_g$ are the coefficients related to shear modulus and bulk modulus, K_g, of the glassy phase respectively, and $I_{C_g} = tr(B_{k_g})$.

In the heating phase, SMPs return to the original shape as the temperature goes above T_g. Due to the melting of glassy phase, the final state of the material is stress free and is given

by $\mu = 0$. The activation criterion for heating (starting of phase change) is governed by,

$$(1-h)\mu_a B_{k_a} + \mu_g h B_{k_g} = cI$$

In a thermomechanical cycle, the change of glassy volume fraction controls the strain storage and release. Consistent with experimental results [123], this volume fraction is assumed to be a function of temperature only. Based on this assumption, a phenomenological function is given by [125],

$$T = 1 - \frac{1}{1 + exp(\frac{T_r - T}{\epsilon})}$$

where T_r is the reference temperature [126] at which the recovery stress has a maximum value. Here ϵ is the parameter determining the width of the phase transition zone. In this study, we set $T_r = 328\ K$ and $\epsilon = 1.5$. These two parameters are obtained from curve-fitting of the experimental results in previous literatures [126].

To implement the constitutive model in ABAQUS, UMAT provides the updated stress and the local tangent stiffness matrix, $\Re$. Here $\Re$ is a fourth-order tensor which is termed as the Jacobian matrix and provides the relationship for the stress and strain. The required Jacobian matrix format is given as

$$\Re = \frac{1}{J}\frac{\partial \tau^J}{\partial D}$$

where τ^J is the Jaumann rate of Kirchoff stress defined as $\tau^J = J\sigma + \sigma^J$. $\Re$ is given as,

$$\Re = [1 - h(T)]\Re_a + h(T)\Re_g$$

$\Re$, which relates stresses to strains thus predicting shape recovery based on the detailed derivation given by Barot. [127] The shear modulus of the amorphous and glassy phases, μ_a

and μ_g, are given as $\mu_a = E_a/2(1+v_a)$ and $\mu_g = E_g/2(1+v_g)$ where $v_a = 0.49$ and $v_a = 0.40$ are Poisson's ratios for the rubbery and glassy phases, respectively [90]. The bulk modulus, K_a and K_g, are given as $K_a = E_a/3(1-2v-a$ and $K_g = E_g/3(1-2v_g)$.

3.3 Experimental results and model validation

3.3.1 Experimental setup and SMP filament preparation

Experiments are conducted for a flat 25 mm long, 3 mm wide, 1.5 mm thick TBA-DEGMA polymer filament. The HIFU transducer rests on the bottom of the tank (Figures 3.2a and b). The tank of water is filled to a depth such that the focal point of the HIFU transducer is located at the surface of the water. Special care is taken to ensure the water doesn't spray when the transducer is activated, and that the exposure power is low enough to prevent sample degradation. In an attempt to prevent acoustic interference, a rigid sample holder is placed outside of the tank to suspend the SMP sample at the surface of the water. The sample is suspended in a way such that the lower surface is submersed in water, and the upper surface is exposed to air. The thermal imaging camera is fixed so that the images are focused around the exposure area of the FU, as shown in Figure 3.2. The camera has an imaging rate of once every four seconds. Duration of sinusoidal exposure is 20 continuous seconds, with most thermal measurements reaching 40 seconds to capture cool down. Data is processed with FLIR Tools software. Exposure power can be varied within the sample damage range. Figure 3.2c shows shape recovery of a SMP filament exposed to FU.

The monomer and the crosslinker that are utilized for fabrication of the SMP filament during the experiments are Tert-Butyl acrylate (TBA) and Di (ethylene glycol) dimethacrylate (DEGMA) (molecular weight 550) respectively. The photo-initiator used for the UV curing

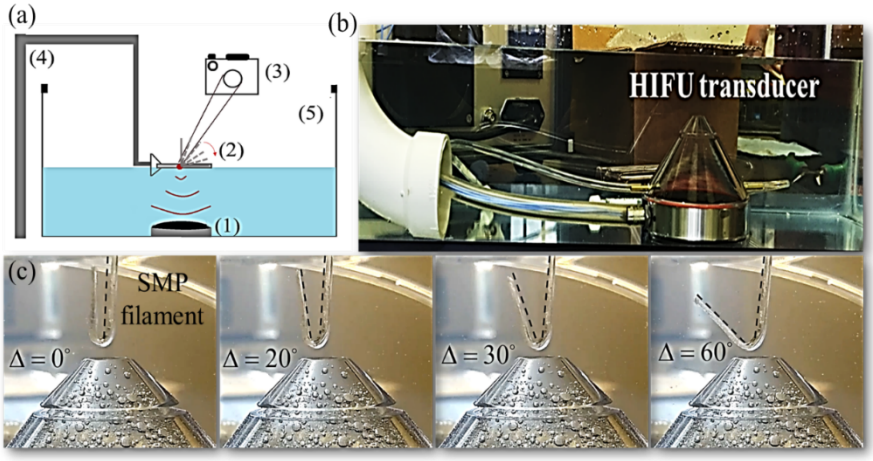

Figure 3.2: (a) Illustration of experimental setup; (1) the transducer resting on the bottom of the tank, (2) shape memory polymer sample is suspended by the sample holder at the surface of the water, (3) thermal imaging camera directed at the focal point of the transducer (indicated by a red circle), (4) and (5) the water tank, and the stand. (b) Experimental setup and (c) shape recovery of a SMP filament exposed to HIFU at different time steps during 20 seconds of HIFU exposure.

process is 2,2-Dimethoxy-2phenyl-acetophenone. All chemicals are purchased from Sigma-Aldrich, and are not altered prior to use. Molds are created with dimensions of 150 mm x 100 mm from clear ultra-scratch resistant acrylic, and sealed with Loctite silicon sealant. Thickness of polymer filaments developed is varied as per the needs of the experiment, but is typically 1.5 mm. Curing is completed with a 100 W Blak-Ray B-100 AP High Intensity UV Lamp.

Depending on the desired composition, TBA is mixed with DEGMA in different volumetric ratios of 80-20; 90-10; 95-5; and 100-0, respectively. The crosslinker-monomer combination is mixed well for ten minutes with a stir plate after adding 1 wt% photo-initiator. The mixture is then transferred to the acrylic molds for curing. The UV light exposure lasts 20 minutes for each mold. The prepared SMP is then removed from the mold. All SMP samples have a permanent shape of a flat rectangle. The SMP film is cut to the desired geometry by either scoring the material or use of a rotary tool.

Dynamic mechanical analysis (DMA) is done for each of the aforementioned compositions. DMA measures storage modulus (Figure 3.3a), Tan delta (Figure 3.3b) and stiffness (Figure 3.3d); the ratio of the loss modulus (Figure 3.3c) to the storage modulus (Figure 3.3a) is the Tan delta and is often called damping. It is a measure of the energy dissipation from a material. A TA Instuments-Q800 DMA is used with an oscillation rate of 1 Hz. The data is collected in steps, and the temperature is ramped at a rate of per minute. DMA analysis and the preliminary experiments for shape recovery behavior show that 95%TBA-5%DEGMA is the most suitable composition and is used for all further experiments and theoretical analysis in this chapter. The preliminary tests show that the other compositions are either too brittle to be used practically or are easily damaged even at low input power to the transducer.

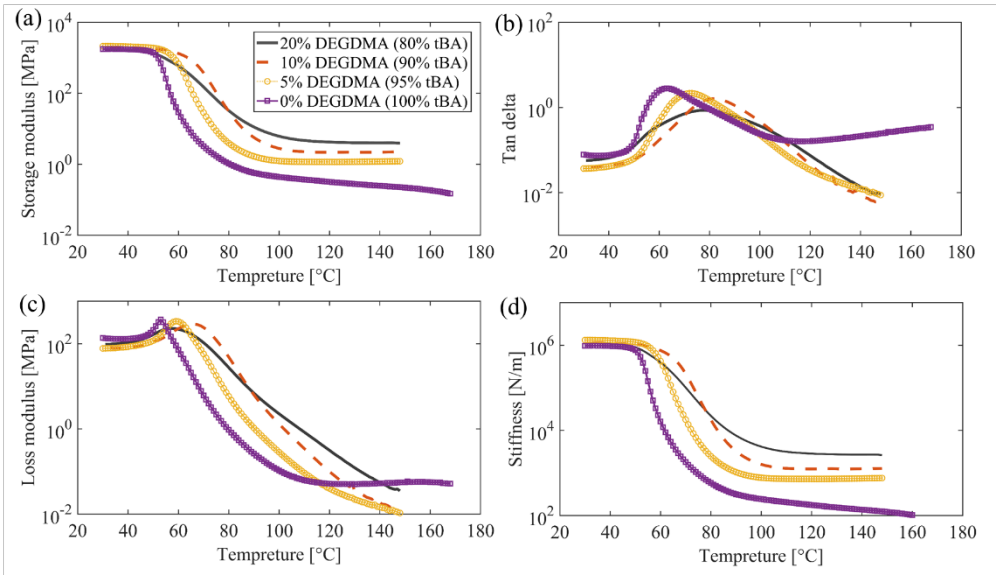

Figure 3.3: (a) Storage modulus, (b) Tan delta, (c) loss modulus and (d) stiffness curves obtained from DMA tests for different compositions.

A hot disk thermal constants analyzer is utilized for evaluating thermal properties of the SMP filament. The hot disk hardware consists of a Keithley 2000 voltmeter, a Keithley 2400 sourcemeter, a Hot-disk bridge, and a computational device. After fabrication of SMP films, 14 disks of 15 mm diameter and 1 mm thickness are cut with a rotary tool. These sheets

are clamped tightly in the sample holder for testing. The measurement method is verified with solid porcelain and sheets of PMMA with known thermal properties. The values of mechanical and thermal properties extracted from DMA analysis and hot disk experiment for 95%TBA-5%DEGMA are reported in Table 3.1. These values are later used in the entire research work for theoretical and experimental analysis of SMP filaments. The results obtained from DMA tests are also used to set the values of following parameters for the mechanical modeling in ABAQUS as $C_10 = 0.28$, $C_20 = 375$, $D_1 = 0.072$ and $D_2 = 0.00054$.

Table 3.1: Mechanical and thermal properties of 95%TBA-5% DEGMA polymer.

Property	Value
T_g	72 $°C$
Density, ρ_m	1100 kg/m^3
E_a	1.66 MPa
E_g	2100 MPa
Thermal conductivity, κ	0.175 $W/m/K$
Specific heat capacity, C_{hm}	1050 $J/kg/K$

3.3.2 Experimental results and acoustic-thermoelastic model validation

Figure 3.4 shows the thermal images of the polymer to demonstrate the temperature rise with respect to time corresponding. The heating of polymer is due to absorption of acoustic energy as a result of viscous shearing exerted by ultrasound focused waves and subsequent release of energy in the form of heat [115]. In the images, the highly concentrated spot in the center has the maximum temperature while the immediate surroundings outside of the focal spot has significantly lower temperatures. This shows a sharp temperature gradient from center to the edges of the polymer demonstrating the highly localized heating effect of focused ultrasound. As seen in the temperature curve in Figure 3.4b, after 20 s, the

ultrasound is switched off and the polymer immediately begins cooling down which is shown by the sharp temperature decay. This ability to change the temperature of the polymer in short range of time shows the capability of focused ultrasound to control the heating effect which is an important parameter to consider in designing of SMP-based CDD systems.

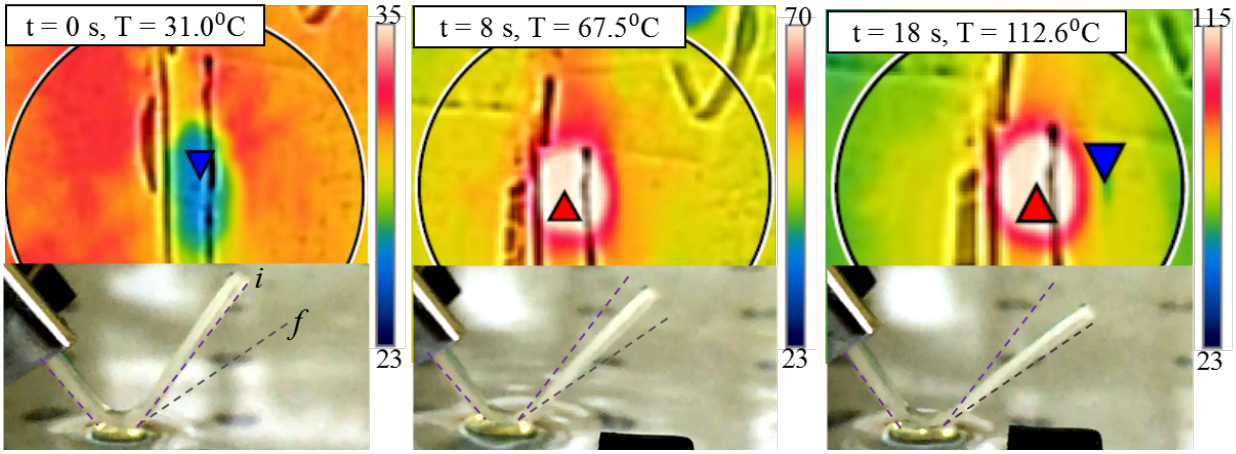

Figure 3.4: Thermal images of the SMP filament exposed to ultrasound at the focal point of the transducer and the corresponding deformation with time; here i denotes the initial angle at temporary shape and f denotes the final angle after shape recovery. The red and blue triangles define the highest and lowest temperature locations in the image (the triangles only account for the portion of the image within the circle).

Having validated the acoustic-thermal model results and identified the mechanical and thermal parameters, a three dimensional filament is modeled to investigate the shape recovery of SMPs thermally induced by FU. The simulations of SMP's recovery process are performed by using a commercially available finite-element software package in ABAQUS (version 6.14, Dassault Systems Simulia Corp., Providence, RI, USA), with a user material subroutine (UMAT).

The SMP filament is modeled in ABAQUS using the properties given in Table 3.1. For the filament, the symmetry in x-direction and y-direction is applied to nodes that are on the central cross section and perpendicular to the x-y directions. Referring to Figure 3.5, a punch and a die, defined as analytical rigid parts, are also introduced for modeling the

loading process. The die is fixed and the punch is constrained in x and y directions, $\mu_x = 0$ and $\mu_y = 0$, while only z-direction movement is allowed. Contact between the punch/die parts and the filament is modeled as frictionless and we assume there is no thermal transfer between punch/die parts and the filament.

The initial temperature is set above the glass transition temperature and the filament is deformed at different angles ranging from 60°to 120°. After cooling and unloading, ultrasound thermal field data from acoustic-thermal model is imported and applied as a mapped temperature distribution field in the finite-element model, ABAQUS, to simulate the heating stage of the mechanical model, at 6 W power as shown in Figure 3.5. The thermal field data is exported from 0 to 20s, divided into 4 sub steps (0-1, 1-5, 5-10, and 10-20 s) and applied as boundary conditions successively in the heating stage in the model. The inset in Figure 3.5 compares the experimental and model predicted values of change in deformed angle against time for a filament with temporary initial angle of 60o. According to Figure 3.5 and Table 3, the simulation results show a good agreement with experiments.

Table 3.2: Experimental and simulation predicted change in initial angle (degree) upon shape recovery process of the SMP filament.

	Final angle		Angle change	
Initial angle	Model	Experiment	Model	Experiment
60	84.06	85	24.19	25
90	110.14	110	20.23	21
120	135.38	135	15.52	15

3.3.3 Effects of various parameters

Simulations are performed to explore the effects of polymer constitutive composition on the shape recovery behavior of SMP filament at a fixed ultrasound actuation power. Reference

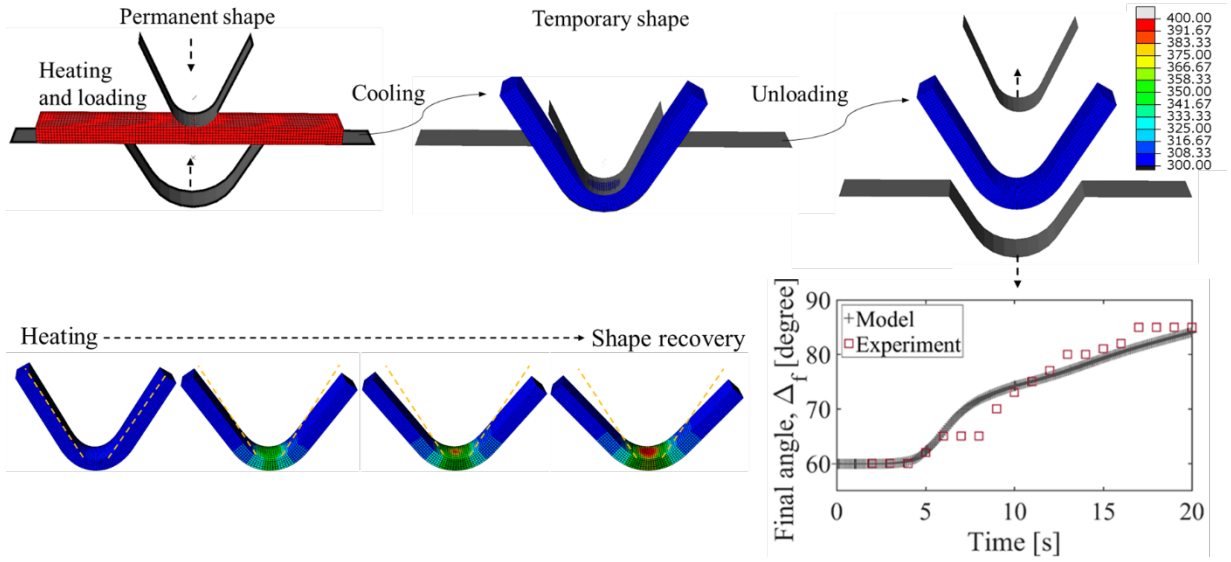

Figure 3.5: Graphical representation of four stages specified in the mechanical model (Sec. II.D.). The SMP is first deformed into a temporary shape and cooled down, followed by unloading. It is then heated by the temperature distributions obtained from the acoustic-thermal model to facilitate shape recovery; the color bar is temperature in K. The inset shows the experimental and model predicted values of change in deformed angle of the SMP filament vs. time.

temperature, T_r, and the elastic modulus of amorphous phase, E_a, are the two parameters to be considered as variables in the simulations, while all other parameters are kept constant. Figure 3.6a shows that the onset of shape recovery is delayed for the SMP with higher characteristic recovery temperature ($T_r = 328\ K$), however the recovery ratios do not show a uniform trend. Figure 3.6b shows that the SMP with higher elastic modulus in rubbery phase gives better shape recovery and therefore achieves larger change in initial angle. The reason is that the polymer with high elastic modulus (hard material) has a higher stored energy under the same deformation during loading stage as compared to a softer polymer with lower elastic modulus. Since for different compositions, the elastic moduli in glass phase are same, the polymer with larger stored energy has a better recovery ratio.

In Table 3.3, the results from simulation show that the glass transition temperature increases with increasing the crosslinker content since the heavier crosslinking will require more energy

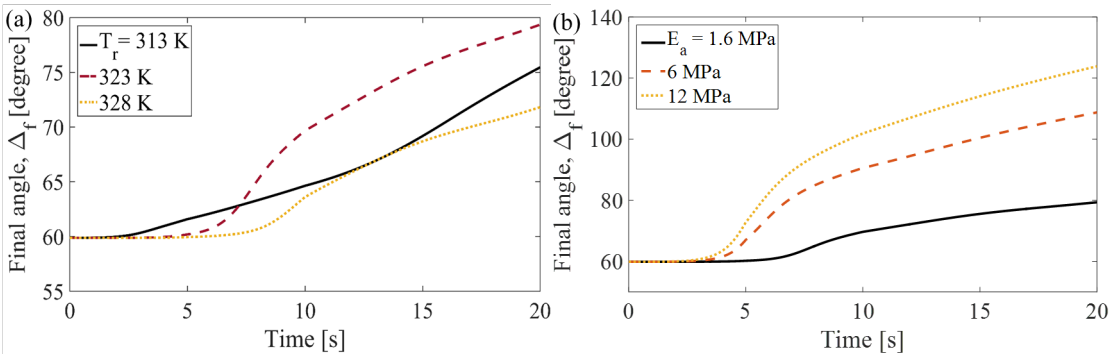

Figure 3.6: (a) Final angle vs. time for various (a) recovery temperature and (b) elastic moduli of amorphous phase.

to begin transition, which is consistent with Figure 3.3. This will also lead to lesser shape recovery as samples with higher T_g and more crosslinking will restrict the chain relaxation and limit the shape recovery process [128]. It is worth to emphasize that in Figure 3.6, the reference temperature and elastic modulus of amorphous phase are the only parameters which are varied in the simulations which is not the case in Table 4 (both reference temperature and elastic modulus are different for various compositions).

Table 3.3: Simulation predicted final angles (degree) upon shape recovery process for various polymer compositions.

%TBA-%DEGMA	$T_g[°C]$	Final angle	Angle change
70-30	91	85	15.52
80-20	82	110	20.23
90-10	72	135	24.19

To study the effect of geometric parameters and input power on the thermal effects and shape recovery behavior of polymers, simulations are performed for varying thickness, width, initial angle of bending curvature of the filament and input power to the transducer. Figure 3.7a shows the final angle (the angle of the deformed area after undergoing shape memory behavior) with time for a 3 mm wide filament with initial deformation of 60°at 6 W of input power for varying thickness. The change in final angle and therefore shape recovery is more

in thicker filaments. The reason behind this trend is the increase in the available sample volume with increased thickness for absorbing heat, resulting in increased bulk temperature of the exposed sample and therefore more shape recovery [128]. Thus, thickness plays an important role in determining shape memory behavior of a given filament.

Figure 3.7b explores the effect of change in width of polymer filament on shape recovery behavior for a 1.5 mm thick filament with initial bending curvature of 60°at 6 W. The increase in width delays the onset of shape recovery and decreases the amount of shape recovery. It is observed that angle recovery onset time is related to the temperature at the edge nodes. Since the filaments have different width, the time taken by edge nodes of filaments with larger width to reach glass transition temperature is more. Thus, a larger width increases the zone of phase transformation and requires more time and energy to transform the overall exposed area and initiate the shape recovery, along with lesser change in initial angle.

The simulations of the filaments for various initial radii of curvature are conducted for a 3 mm wide and 1.5 mm thick filament heated at 6 W power of focused ultrasound. Figure 3.7c shows that even though the filaments have almost same onset time, a sharper bending area leads to a larger deformation. Since the filaments have same width, the time for edge nodes on central cross section to reach the glass transition temperature is approximately the same. Hence, the filaments with different bending radius but same width have almost same recovery onset time. However, for a sharper bending area, the spreading phase transformation zone easily covers the whole bending area which results in a larger deformation for the sharper filament.

Figure 3.7d shows the final angle with respect to time at various input powers. The thickness of the polymer filament is kept constant at 1.5 mm and initial angle of 60°is used for all powers. It is seen that higher input power results in higher shape recovery (more change in

initial angle) of the polymer. This is expected as the increase in power will result in increase in absorption of energy, due to higher internal friction and therefore increase in energy subsequently released as heat [128]. As power increases, the bulk temperature crosses T_g at an earlier time step thus initiating early shape recovery.

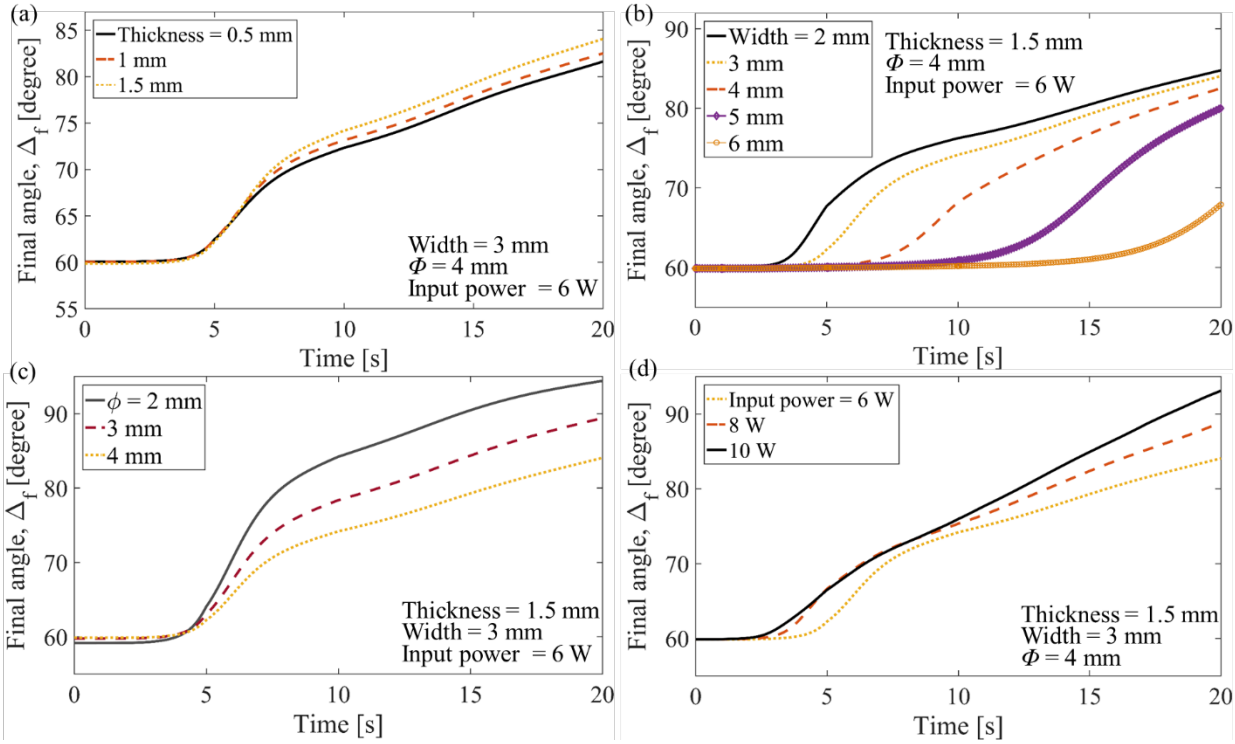

Figure 3.7: Final angle vs. time for various (a) thickness and (b) width of the SMP filament, (c) initial bending curvatures of the deformed area, and (d) transducer input powers.

3.3.4 SMP container design

The theoretical model in this research aims to develop a mathematical framework for optimizing and evaluating the role of different input parameters, geometrical configuration, and medium properties on shape memory behavior of polymers through experimental validation. The efforts lead to propose a design for an ultrasound activated drug delivery container. A possible design for such a container is shown in Figure 3.8. The 0.3 mm wide (diameter)

container is a 2D representation of Figure 3.1 and is composed of 0.01 mm thick layer of 95% TBA-5% DEGMA kept at the focal point of the ultrasound transducer. Figure 3.8 shows the simultaneous displacement of the valve and diaphragm with time and the intermediary stages due to shape recovery under HIFU at 6 W. The color contour gives the temperature distribution inside the container.

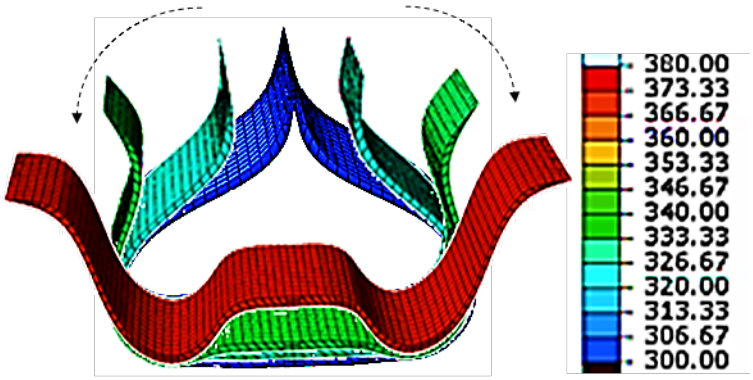

Figure 3.8: Thermal distribution of a container kept at focal point of the transducer; the color bar is temperature in K. The intermediary stages represent the movement of the valve with time due to shape recovery under FU.

The design proposes a novel mechanism for simultaneously opening the drug container and pushing the particles out, which will significantly improve the rate of drug releasing. The movement of valve with respect to diaphragm is shown in Figure 3.9a. Figure 3.9b shows the normalized velocity (normalization is done with respect to the maximum velocity) of the diaphragm and valve is maximum within first five seconds suggesting the maximum release of drug particles occurs within first (Figure 3.9) seconds of ultrasound exposure. The time at which the normalized velocity attains maximum can be manipulated by varying the input power or geometric parameters of the container. Since the diaphragm velocity is lower than the valve velocity as shown in Figure 3.9c, the drug release of particles is expected to be uniform, unhindered and regulated. It is worth noting here that we are only showing a proof of concept and the developed experimental-computational framework can be utilized

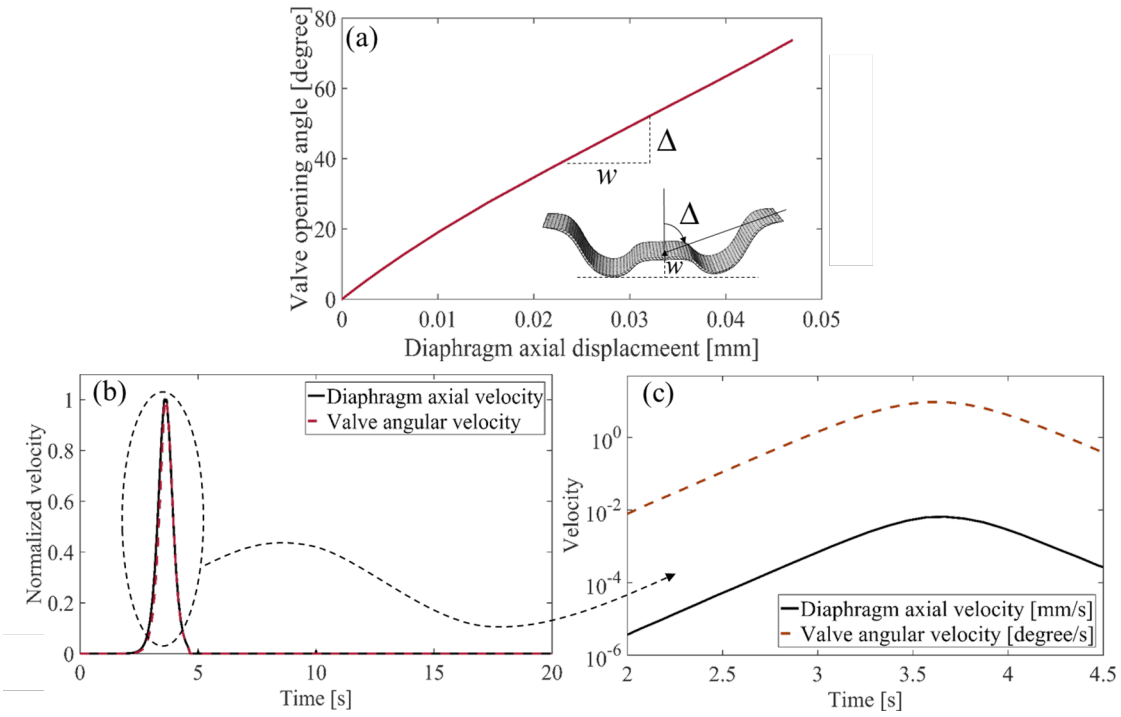

Figure 3.9: (a) Angular displacement of valve vs. transverse displacement of diaphragm of the container, (b) normalized velocity vs. time for diaphragm and valve, and (c) velocity vs. time for diaphragm and valve for the time range when they attain maximum.

for designing various ultrasound activated drug delivery containers, specifically tailored for different applications depending on the size of drug particles, target time for releasing the particles, and the size/shape of the container. This is the topic of a future communication by the authors.

3.4 Conclusions

This chapter aims to present a combined acoustic-thermal-structural model to predict the shape recovery behavior of polymers under focused ultrasound. The numerical model provides the basis for designing spatially and temporally controlled drug delivery (CDD) systems. A theoretical framework is used to predict acoustic pressure field due to focused

transducers, and the acoustic model is coupled with a thermal model to predict the developed temperature field due to focused ultrasound. The thermal field is then coupled to the mechanical model which solves for the stresses developed in the polymer and predicts the shape recovery of the system. Experiments are conducted to validate the numerical model. In addition to successful model validations against 3D finite-element simulations, a study on the effects of several system parameters is performed. The model is used to explore the effects of medium properties (nonlinearity and absorption), geometrical properties (thickness, width and initial deformation of the polymer filament) and input parameters (power and frequency) on shape recovery behavior of the polymer. The results show that while input source frequency has more influence on nonlinearity, input power plays a major role in achieving high temperature rise rates and thereby faster onset and increased shape recovery. Observations related to medium properties show that the coefficient of nonlinearity of the medium plays a significant role in distorting the waveform and generating more harmonics, thus increasing the energy deposition at the focal point and enhancing the shape recovery behavior. Our results will pave the way for introducing a more efficient drug delivery capsules at meso to nanoscale, and will shed light into the details of utilizing focused ultrasound for stimulating SMP-based mechanisms in drug delivery applications.

Chapter 4

Polyethylene in HIFU fields

4.1 Introduction

Chapter 3 explores the feasibility of SMPs for designing medical devices. However, when polymers are heated in HIFU fields, the mechanism of the size-dependent thermal effect is still not clear yet. In this chapter, we investigate two factors, the types and the sizes of the polymers, to the thermal effect induced by HIFU. As we know, stimuli-responsive polymers, i.e., shape memory and shape-changing polymers, have been intensively investigated for their applications in controlled drug delivery [129–132], sensing and biosensing [133, 134], smart coating [135], soft robotics [136, 137] and flexible electronics [138, 139]. The choice of an environmental trigger for stimulating polymers is one of the critical factors. Although direct heat is one of the most commonly used triggers, it is not always practical and safe, especially for heat-sensitive applications [140–142]. Consequently, other forms of noninvasive actuating mechanisms such as irradiation (UV, IR, and solar), magnetic field, electric current, among others, have come to the forefront [143–151]. However, most of these triggers significantly lower the efficiency of the responsiveness of the polymers. As an alternative to the conventional stimulus type, it has been shown that the polymeric materials are ultrasound-stimulus-responsive, with controlled multifunction [131, 152]. High-intensity focused ultrasound (HIFU) is an entirely different and promising stimulus due to its superior and unique capability. HIFU could induce localized heating and achieve temporal and spa-

tial effects in polymers, by adjusting the geometric and chemical properties of the polymer, ultrasound frequency, exposure time, intensity as well as the position of ultrasound focusing, all while being noninvasively.

HIFU transmits and focuses acoustic energy from a transducer into a small focal volume. The sound waves are directed to interact with polymer chains in a selected area, heat the polymers locally, and cause a significant thermal effect on the focal point, while the surrounding area is not significantly affected. When the mechanical waves pass through the polymer matrix, damping loss will occur due to viscous shearing and relaxation. Ultrasonic waves, as one kind of mechanical wave, can make a polymer behaves in a pattern of forced vibration, and thus exert alternative stress at every chain of the polymer matrix. For viscoelastic polymer materials, change of strain will lag behind that of stress, which induces the internal friction, and the energy absorption during HIFU absorption. The energy absorption pattern has two types, one part of the energy is dissipated and transformed into heat, and the remaining part is stored by elastic deformation of polymer chains. The ultrasound energy converts to heat through the internal friction, which induces the temperature rise of the polymer. This localized heating eliminates the need to incorporate individual or responsive particles employed for use noninvasive triggers [25]; therefore, ultrasound can be considered one of the most potent modalities for spatiotemporal stimulation of polymers in an on-off switch manner.

Unlike conventional heating, it has been observed that different polymers possess different HIFU-induced thermal effects [153]. However, the research related to the fundamental mechanisms behind this phenomenon, particularly at the atomistic scale, is still limited. Liu et al. reported the heating rate and equilibrium temperature for HIFU heated polyethylene (PE), poly(methyl methacrylate) (PMMA), Polycarbonate (PC), polystyrene (PS), Nylon-6 (PA-6) and polypropylene (PP) [154]. Without any evidence, they hypothesized that the

variation in heating effect for different polymers could be attributed to the different internal friction between their macromolecular chains. Bruinewoud also investigated the ultrasound-induced thermal effect of a set of polymers, including PMMA, PUR PEVA. They thought the ultrasonic attenuation might be a key factor [155]. Coralie and co-workers reported the correlation between the particle velocity distribution and PMMA heating effect by HIFU [44], and they concluded the particle velocity distribution and the sample thickness determine the heating response of the polymer. Although these experimental results indicate that the ultrasound-induced thermal effect in polymers are affected by many factors, to understand the mechanisms completely only by experiments is extremely challenging. This is because tracking the interaction between the polymer and ultrasonic waves at the atomistic scale by the experiments is very difficult. As an alternative, here, we utilize computational models to explore how the HIFU triggers thermal actuation of polymers, and how the atomistic structure of the polymer interacts with the representative mechanism. Molecular dynamic (MD) simulations have been shown as a unique tool for studying the thermal properties of polymeric materials [136, 141, 146, 156, 157]. The trajectory history of every atom in the polymeric system during the ultrasonic actuation, as well as the evolution of the chain orientation can be recorded.

We investigate the ultrasound-induced thermal effect at the atomistic scale by MD simulation (using the LAMMPS package [145]). Related experiments were also performed to support the findings of the computational model. We will particularly focus on exploring the role of chain arrangement and structure on the thermal effects. Amorphous polyethylene and crystalline polyethylene are modeled as a counterpart. In the following section, we regard amorphous polyethylene as low density polyethylene (LDPE), and crystalline polyethylene is represented by high density polyethylene (HDPE), shown in Figure 4.1. To our best knowledge, this is the first study on the ultrasound-induced heating effect of polymeric

materials at the atomistic scale, which can explain the observed responses at the macroscale.

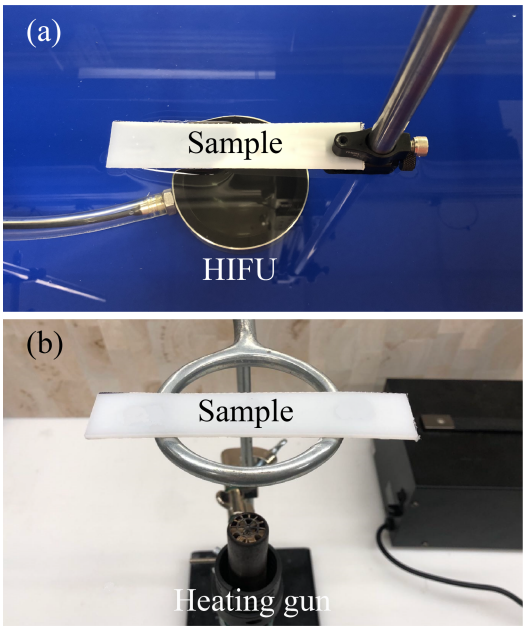

Figure 4.1: (a) Experimental setup of the polymer filament with fixed-free boundary conditions exposed to harmonic acoustic pressure at 0.5 MHz; the geometric center of the filament is located in the focal area. (b) Heat gun setup.

4.2 Methods

4.2.1 Experimental scenarios

Before delivering the results from MD simulation, we show two experimental scenarios about actuating the polymers with HIFU and direct heat are shown here. Firstly, in Figure 4.1a, a PE filament with a dimension of 125 × 25 × 2.38 mm was suspended by a holder at the surface of deionized water. Next, the filament was exposed to harmonic acoustic pressure field at 0.5 MHz generated by a modified H-104–4 A SONIC Concepts HIFU transducer. The transducer, actuated with 30 V voltage at 6 W input power, was turned on in continuous mode for 30 seconds. The geometric details of the modified HIFU transducer are listed

in Table 4.1. The distance between the transducer and the filament is 50 mm, which was adjusted by a positioning system, to make the geometric center of the filament located at the focal area of the transducer. The water level in the tank was maintained, such that the bottom part of the filament was submerged in water and the focal point of the HIFU transducer located at the central portion of the filament. The power of the transducer is maintained below a threshold level (10 W) to prevent degradation of the sample.

Table 4.1: The geometric details of the modified H-104–4 A SONIC Concepts HIFU transducer.

Outer Diameter	Intensity Focus Watts	Focal Width (dia.)	Focal Length
$64mm$	$3,267.56\ W/cm^2$	$3.02\ mm$	$50\ mm$

A FLIR C2 thermal imaging camera was fixed to capture thermal images focusing on the exposure area of the HIFU. The camera has an imaging rate of around 0.25 Hz. The duration of ultrasonic actuation is 30 continuous seconds, with most thermal measurements reaching 40 seconds to make sure the entire thermal history is captured. Data is processed with FLIR Tools software. For the direct heat method, the sample was suspended 80 mm above a heat gun in Figure 4.1b. The exhaust temperature of the hot air was set at 180 ℃, to make the temperature rises by hot air and ultrasound comparable.

4.2.2 Simulation methods

In the following sections, we regard amorphous polyethylene as LDPE and crystalline polyethylene as HDPE, shown in Figure 4.2. In the MD simulation, the polymeric systems were built by a self-avoiding random-walk algorithm initially, then equilibrated under different conditions to create an amorphous structure (LDPE) and a crystalline structure (HDPE) separately. The details of the equilibration conditions are discussed as follow.

To avoid the influence of molecular weights (chain lengths), both systems contain 576 chains with chain length N=400, in a total of 230400 atoms. For LDPE, the initial geometry is first melted by increasing the temperature from 300 to 500 K. The system is further annealed back to 300 K, followed by an equilibration through NPT ensemble until the density reaches the targeted value (0.9 g/cm3). To form the HDPE structure, the system is melted at 500 K, then pre-stretched along the z-direction. After that, the oriented melt is suddenly quenched down to 330 K, then an NPT ensemble runs for 60 ns at 330 K to guarantee the crystallization grows sufficiently. Finally, the system is cooled down to 300 K and equilibrated again.

The simulation domain (shown in Figure 4.2), which is periodic in x and y direction, contains polymeric materials on a substrate. Polymeric chains are rendered in different colors to show the structure variation. We use the potential force filed for polyethylene-like material [158, 159], a cutoff distance of 10.0 Å for the Lennard-Jones interaction and 1 fs as the time step for all simulations.

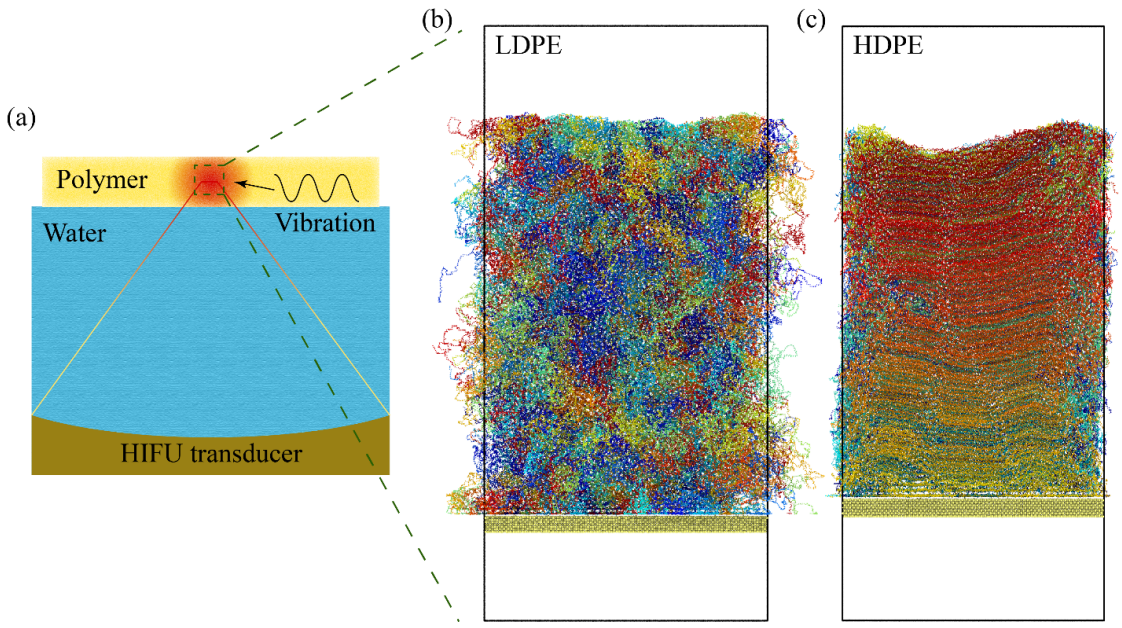

Figure 4.2: Schematics of (a) typical ultrasound-induced heating setup, and MD simulation setup for (b) LDPE and (c) HDPE system.

As mentioned early, the temperature rises for HDPE and LDPE are similar manner by direct heat. Therefore, it is interesting to use MD simulations to explore the reasons why the heating rate varies when they are subjected to HIFU. In the simulation, the substrate is vertically oscillated at multiple frequencies to imitate the mechanical vibration caused by ultrasonic waves. The substrate is maintained at 300 K to physically represent the heat sink at room temperature, while no temperature restriction is placed on the polymer system (NVE ensemble). The velocity of the substrate in the z-direction is $v_0 = A\omega\cos(\omega t)$, where A is the amplitude and is the frequency. A summary of all parameters applied in the MD simulations is listed in Table 4.2. With regard to HIFU specification, the amplitude and frequency here are proportional to the ultrasound input power and frequency.

Table 4.2: The parameters applied in the MD simulations.

	Frequency (GHz)	Amplitude (nm)	Duration (ns)
Case 1	8.33	0.5	1
Case 2	11.1	0.5	1
Case 3	12.5	0.5	1
Case 4	8.33	2.0	20

4.3 Results and Discussions

4.3.1 experimental results

The samples were exposed to the ultrasound or hot air for 30 s, the temperature changes for HDPE and LDPE are shown in Figure 4.3a. For all the cases, the initial temperatures are ranging from 25 to 27 ℃ (the room temperature). Heating by hot air, the temperatures for HDPE and LDPE are ramped almost linearly, with $R^2 = 0.9988$ and 0.9997 separately. However, when the samples are stimulated by HIFU, the temperature rises are nonlinear

and saturated after 15 s. In the initial 5 s, the rate of temperature increase for LDPE and HDPE are 2.2 $°Cs^{-1}$and 0.88 $°Cs^{-1}$separately, so the observed temperature rate for LDPE is larger than HDPE by an amount of 150%. The equilibrium temperature for LDPE, after 30 s exposure to HIFU, is 48 °C which is 10 °C higher than that of HDPE. Figure 4.3 b-e show the induced thermal field of the HDPE and LDPE filaments when t=25 s. In the image, the spot in the center has the maximum temperature. This indicates the thermal effect of focused ultrasound on PE materials is highly concentrated and localized.

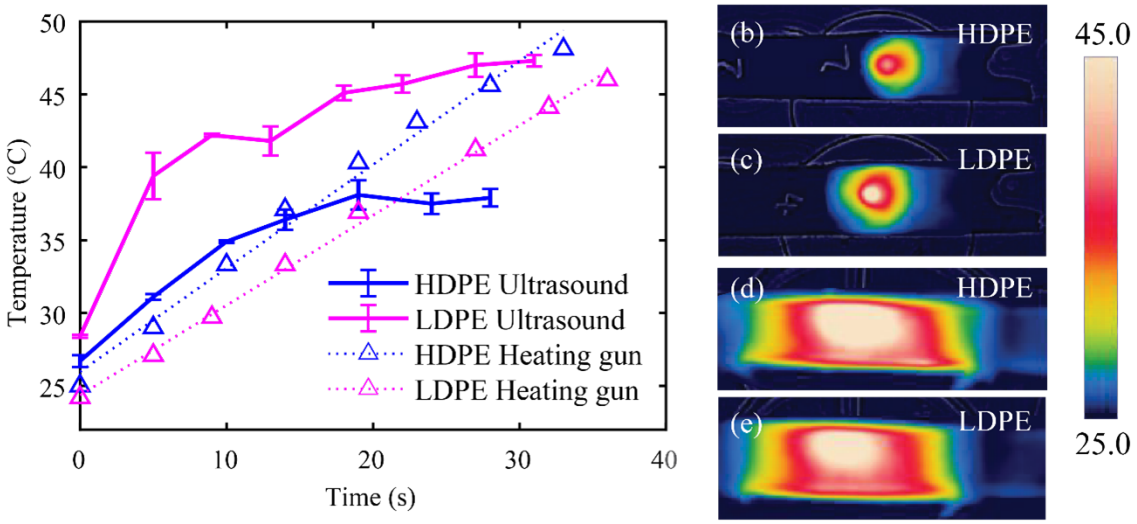

Figure 4.3: (a) temperature vs. time for HDPE and LDPE induced by HIFU (solid lines) or heat gun (dot lines). Thermal images of (b) HDPE and (c) LDPE filaments under ultrasound, (d) HDPE and (e) LDPE filaments under hot air when t= 30 s.

4.3.2 Molecular dynamics simulation

We systematically study the thermal effect of HIFU on HDPE and LDPE across a wide range of oscillation times, amplitudes (A) and frequencies (f). The temperature evolution with a time duration of $1ns$ for $A = 0.5\ nm$, as well as $f = 8.33, 11.1, 12.5\ GHz$ are shown in Figure 4.4a-c. In Figure 4.4d, the substrate is oscillating for 20 ns at $A = 2\ nm$ and $f = 8.33\ GHz$.

Upon Figure 4.4a-c, we found the frequency increase raises the polymer temperature in general. In addition, in comparison of Figure 4.4b and c, the heating rate for LDPE is higher than that of HDPE, which is consistent with the experimental results. It is also interesting to note that although the temperature rise in Figure 4.4a is almost negligible due to the relatively low frequency, the accumulated thermal effect becomes considerable when the amplitude and time scale enlarge at the same frequency, which results in a prominent temperature rise as shown in Figure 4.4d. The applicable HIFU frequency (MHz) is orders of magnitude smaller than that in the MD simulation (GHz), but we believe that the MD simulation here is able to replicate the heating mechanism in a manner which is consistent with the actual experiment. Firstly, although acoustic energy with higher frequencies is lost more along the beam path before reaching the target, the mechanism of the vibration-induced heating is not dependent on that. The frequency-dependent energy absorption efficiency of the sample is beyond the scope of this work. Secondly, because of the limit of computational resources, the time scale of most MD simulation is at the range of several nanoseconds (10^{-9} s). This is a very common problem in almost all MD simulations, but researchers show molecular dynamics simulations are able to capture the critical mechanism for ultrasonic actuation problems. Therefore, we believe our MD results can shed light on the mechanism at the macroscale.

Now the open question is why HDPE and LDPE, with the same chemical composition and chain length, respond differently to the same external excitation. By using MD simulations, we are able to provide a qualitative description of the ultrasonic actuation mechanism in a top-to-bottom manner, in which the microscopic picture of the HIFU-induced vibration is described at different scales from the entire polymer system, single polymeric chain down to single atoms. For the entire polymer system, the heat is generated by the viscoelastic damping, which is highly dependent on the polymer viscoelasticity. Since viscoelasticity

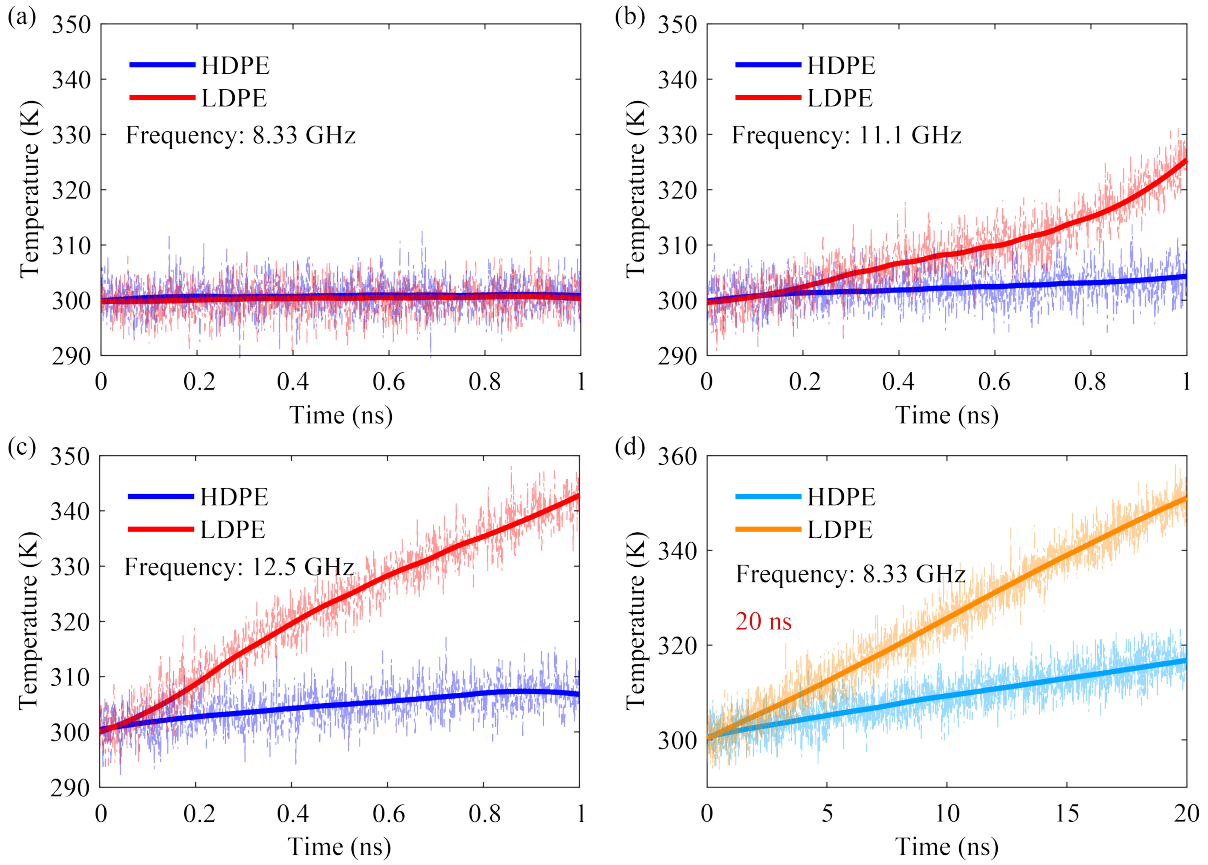

Figure 4.4: Temperature vs. time curve for 1 ns at frequencies of (a) 8.33 GHz, (b) 11.1 GHz, (c) 12.5 GHz, and (d) for 20 ns at a frequency of 8.33 GHz.

is frequency-dependent, the phase lag between stress and stress curves is also related to frequency. The dissipated energy per cycle that transferred into heat can be given as the following energy density function:

$$\delta W = \sigma_0 \epsilon_0 \int_0^{\frac{2\pi}{f}} \sin(\omega t) \cos\ (ft - \theta) dt$$

where σ_0 is the amplitude of stress, ϵ_0 is the amplitude of strain, f is the frequency, θ is the phase lag between the stress and strain curves. Note that the energy into heat δW is in direct proportion to σ_0, ϵ_0, and θ. The frequency f is set to be 8.33 GHz and 12.5 GHz as shown in Figure 4.5. Figures 4.5a and c represent the results for HDPE while Figure 4.5b

and d represents LDPE.

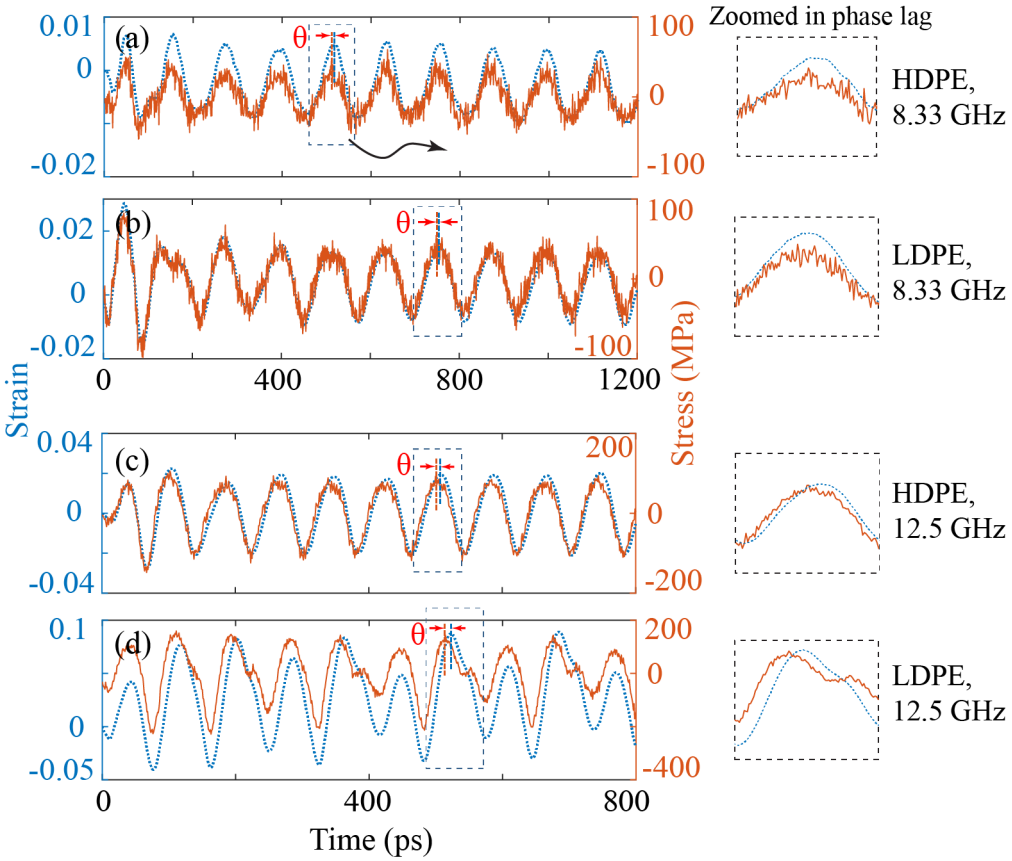

Figure 4.5: The evolution of stress curves (in red) and strain curves (in blue) and their phase lag at a frequency of 8.33 GHz for (a) HDPE and (b) LDPE, plus at a frequency of 12.5 GHz for (c) HDPE and (d) LDPE. Zoom-in graphs to show the phase lag between stress and strain curves are inserted.

The temperature difference between HDPE and LDPE at 8.33 GHz is negligible, and results in subtle phase lags between strain curves and stress curves for both LDEP and HDPE as seen in Figure 4.5. When the frequency increases to 12.5 GHz, LDPE shows an apparent temperature increase. Correspondingly, there is a significant lag between the stress and strain curves in Figure 4.5d (shown in the zoom-in plot). Contrary to LDPE, the phase lag change for HDPE between 8.33 GHz and 12.5 GHz becomes slightly larger (Figure 4.5c). Besides, the oscillating amplitude of stress/strain curves, at 12.5 GHz is prominently larger

than that at 8.33 GHz. Moreover, the stress/strain amplitude for LDPE is larger than that for HDPE at the specific frequencies. Figure 4.6 shows the relationship between the position of the oscillated substrate and the stress of the polymer at 12.5 GHz. whether the stress change can follow the substrate movement. We can find there is a more pronounced phase delay between the substrate position and the polymer stress curve (labeled as δ) for LDPE in Figure 4.6b than that for HDPE in Figure 4.6a . Hereby, the LDPE is expected to be more difficult to follow the external vibration, such as by ultrasonic actuation, which may cause more viscous internal friction and then generate more heat.

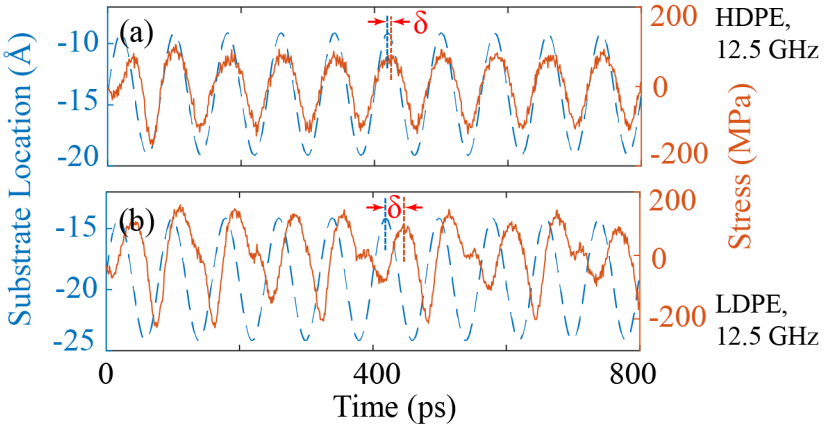

Figure 4.6: The evolution of substrate movement (in blue) and stress (in red) for (a) LDPE and (b) HDPE at the frequency of 12.5 GHz.

To investigate the differences in the thermal effects of the two PE systems in terms of quantities at the polymeric chain level, we first perform the topological analysis on the systems by using the Z1 method. This method is used for identification of entanglement and calculation of the entanglement length. By performing Z1 analysis, the movement of single polymer chains, the number of interior "kinks", Z, and the entanglement length N_e are introduced here. Z is proportional to the number of entanglement per chain, while N_e is defined as the ratio between chain length N and the number of entanglements. For crystalline PE, $Z = 4.052$ and $N_e = 79.136$, while for amorphous PE, $Z = 4.806$ and $N_e = 68.870$.

When polymers react to the vibration induced by ultrasonic waves, the entanglements will continuously be created and lost due to the contour length fluctuation (CLF) of the primitive chains. Regarding the reptation mechanism in the tube model, the movements of polymeric chains will also lead to a constraint release (CF) when polymeric chains are crawling out of the tube. When CLF and CF happen, the more entangled chains in amorphous PE tend to generate more heat than the less entangled chains in crystalline PE.

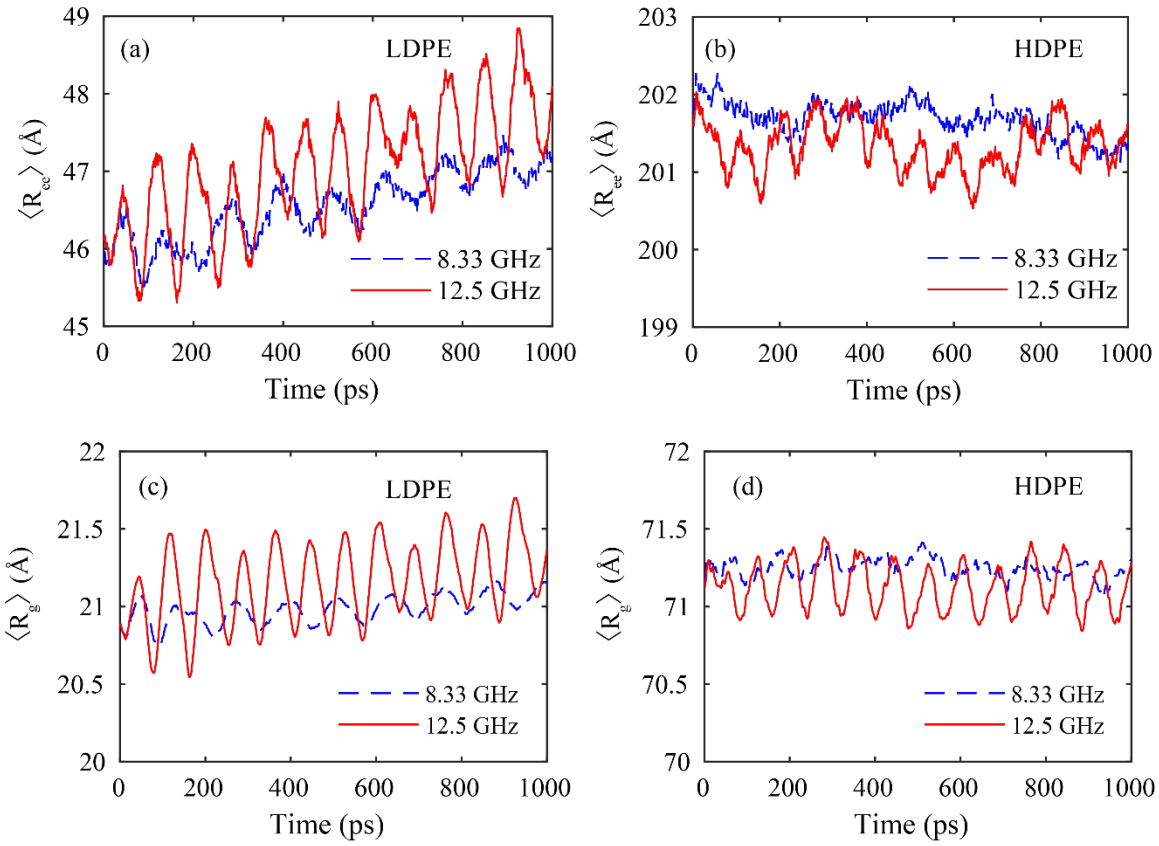

Figure 4.7: The evolution of substrate movement (in blue) and stress (in red) for (a) LDPE and (b) HDPE at the frequency of 12.5 GHz.

The evolution of averaged chain end-to-end distance, $\langle R_{ee} \rangle$, and radius of gyration, $\langle R_g \rangle$, for all polymeric chains in both amorphous PE and crystalline PE systems during actuation are reported in Figure 4.7. From Figure 4.7a and b, it is found the values of end-to-end distance of amorphous PE increases while that of crystalline PE decreases. It shows that the random

polymeric coils in amorphous PE tend to extend while the more aligned chains in crystalline PE are crimped slightly. The evolution of radius of gyration in Figure 4.7c and d provides evidence to this micropicture of polymeric chains when it is excited by the ultrasonic wave. Grouping Figure 4.7a-d, the movements and geometric changes of polymeric chains are more significant at a higher frequency (12.5 GHz) that at a lower frequency. Comparing between the amorphous PE and crystalline PE at the same frequency, the conformational fluctuation of polymeric chains in amorphous PE is more pronounced than crystalline PE, which is the reason for the different ultrasound-induced thermal effects at chain level.

Focusing on the vibration of single atoms, we believe that the discrepancy in the ultrasound-induced motion of atoms in HDPE and LDPE causes the observed difference in their temperature change, since the temperature is a measurement of the average kinetic energy of the system. To examine this hypothesis, we introduce the root mean square fluctuation, RMSF [151, 160, 161], of every PE monomer in the system to evaluate the vibration-induced local mobility of HDPE and LDPE. The expression of RMSF takes the following format:

$$RMSF_i = \sqrt{(\frac{1}{\tau}\sum_{t=1}^{\tau} -(r_i(t) - r_{i,mean})^2}$$

Figure 4.8 shows that the overall RMSF value is lower when the polymer is excited by a lower frequency external vibration. Compared between HDPE and LDPE, the flexibility of HDPE with the crystalline structure is much less than that of the amorphous LDPE. The chain movement inside HDPE is less active, which may cause less friction with surrounding chains. It means less heat will be generated due to the internal friction, thus HDPE is less heated by focused ultrasound compared to LDPE.

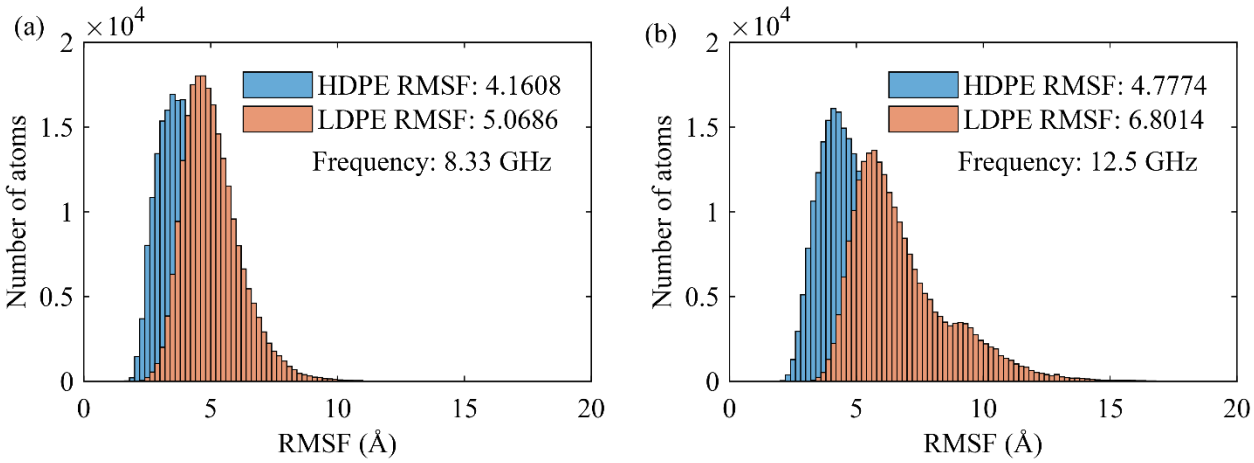

Figure 4.8: RMSF values of HDPE and LDPE at frequencies of (a) 8.33 GHz and (b) 12.5 GHz.

4.4 Conclusion

In this work, the HIFU-induced thermal effect on PE was systematically studied by experiments and MD simulations. From the experiments, we found the heating rate of amorphous LDPE is remarkably larger than the crystalline HDPE under focused ultrasound with the same acoustic power. To investigate the mechanisms behind this phenomenon, MD simulations were performed. In a top-down manner, the mechanisms were investigated at different conformational scales. At the entire system level, we found the frequency-dependent viscoelasticity is the direct factor. It was shown the amplitude of cyclic stress σ_0, strain ϵ_0, and the corresponding phase lag θ, determine the ultrasound-induced thermal effect on PE. When the polymers react to ultrasonic waves, LDPE has a larger phase lag θ than HDPE, and results in a larger heating rate. With the increase of frequency, the increases of σ_0 and ϵ_0 are the proximate causes of fast heating in response to the HIFU. Second, at the molecular chain level, we found the thermal motion of chains in LDPE is larger than HDPE by analyzing the conformational quantities, the end-to-end distance and radius of gyration. Last, the parameter RMSF indicates the atoms inside LDPE are more flexible than HDPE on

average. In conclusion, this study can establish a rigorous link between molecular constitute and macroscopic mechanical properties, i.e., between polymer chemistry and viscoelasticity, for optimal processing, design, and application of polymers in the HIFU fields.

Chapter 5

A ductile SMP composite with enhanced shape recovery ability

5.1 Introduction

Shape memory polymers (SMPs) are a class of smart materials which can store one or more intermediate shapes and recover to their permanent shape when subjected to an external stimulus [162–165]. The ability of being responsive to multiple stimuli [166] enable SMPs a superior choice for applications in soft actuator and soft robotics [167, 168]. For certain types of SMPs [169], being biodegradable and biocompatible also make them potential candidates in biosensing [170, 171], and controlled drug delivery fields [172–175]. SMPs can be usually categorized into several types, namely, chemo-/thermo-responsive [176–180], and photo-responsive SMPs [181]. When temperature rises, the thermo-responsive SMPs absorb heat to accomplish shape recovery due to the inner phase transition or components softening/transition [177]. Compared to traditional shape memory materials, such as shape memory alloys [182, 183] and shape memory ceramics [184], SMPs are flexible, inexpensive, lightweight, and consequently applicable in a broad range of devices. Because of these advantages of SMPs, the study of their properties has received extended attentions in the past several years.

Among multiple types of SMPs, acrylate-based AB copolymer networks, obtained from

monomers and crosslinkers copolymerization, have remarkable advantages such as the biocompatibility [185, 186], relative ease of preparation,[187] and 3D/4D printability [188–190]. For instance, Yu et al. demonstrated a photopolymer printable tertbutyl acrylate (tBA)-co-di(ethylene glycol) dimethacrylate (DEGMA) network [191]. By using the stereolithography apparatus (SLA) technology, thermo-responsive acrylate-based SMPs with complex geometry can be fabricated. Hongzhi and co-workers also presented a four-dimensional printing method to fabricate acrylate-based SMPs [192]. G. Jerald et al. synthesized a type of SMPs by using tBA and poly (ethylene glycol) dimethacrylate (PEGDMA). The synthesized SMP sample can recover from the deformed shape (a deformed M-shape filament) to the permanent shape (a straight filament) in 45 seconds after being completely immersed in 55 °C/min hot water. By adding diurethane dimethacrylate (DUDMA) to the existing tBA-PEGDMA SMP matrix, the shape recovery rate of this SMP network become around 20 seconds for full recovery [193].

Despite many works reported on fabricating efficient SMPs, experiments have shown that fulfilling a 100% shape recovery within a few seconds ($<$ 10 s) is still challenging. If SMPs have large recovery percentage and fast response, it will make them a good candidate for being used as remote actuators. One example is the high-intensity focused ultrasound (HIFU) induced in vivo drug delivery system, because HIFU can remotely and noninvasively actuate SMPs. However, the actuation is usually slow, and the recovery percentage is low, which emerges the need for new classes of SMPs with large recovery percentage and a fast response. We have recently investigated the influence of chemical composition of SMPs on HIFU-induced shape recovery [172, 194–196]. In these works, tBA and DEGMA were used as monomer and crosslinker to synthesize SMPs. It was shown the chemical composition (the ratio of monomer to crosslinker) has a significant effect on the final shape recovery ratio of SMPs (Need to note that selecting a proper programming temperature can also help

optimize the shape recovery performance even without modifying its composite [197, 198], but we choose to tune the chemical composite in this work). Tuning the composition ratio could help achieve a higher shape recovery ratio after a 20 second continuously ultrasonic exposure. However, the maximum recovery ratio was around 20%. In our recent study, it was found that the HIFU-induced thermal effect for polymers is closely associated with the viscoelasticity of materials [199]. The viscous damping caused by the HIFU results in obvious heating difference. The computational works indicated that more heat is generated in viscoelastic amorphous polymers when they are subject to HIFU compared to crystalline polymers.

Therefore, to design more efficient HIFU-induced SMP devices, the targeted properties of SMPs fall into two aspects. On one hand, the actuation of SMPs should be efficient, which means sufficient heat can be accumulated at relatively low acoustic power exposure. On the other hand, SMPs should have adequate recoverability, which is closely associated with the elastic part (the cross-linking in the thermoset material). It refers that the SMPs can achieve fast full recovery, such as a 95% or more recovery ratio within 10 seconds, when subject to traditional heat sources (like hot water or air).

In this chapter, an acrylate-based polymeric composite with a superior shape memory ability is synthesized. This composite can achieve almost 100% shape recovery ratio within 2 seconds under hot air/water. From the DMA test, it is observed this composite also have relatively large viscoelasticity, which may lead to good thermic response triggered by HIFU. Nanoindentation tests are also conducted to further explore the related mechanical properties of this composite. Additionally, molecular dynamics (MD) simulations are also performed to study the reasons behind these properties at the atomistic scale by investigating the crosslinking mechanism for the curing process of this composite.

5.2 Materials and Methods

Tertbutyl acrylate (tBA), di(ethylene glycol) dimethacrylate (DEGMA), polystyrene (PS) pellets with typical molecular weights of $M_n = 35,000$, toluene (anhydrous, 99.8%) and the photo-initiator 2,2-dimethoxy-2-phenyl-acetophenone were purchased from Sigma-Aldrich and used as received condition without further alternation. Molds are ordered from Allied High Tech Products, Inc. In a typical experiment, tBA (monomer) and DEGMA (crosslinker) were firstly mixed at a weight ratio of 85:15, followed by 1 wt% photo-initiator added into the solution. The solution was then fully stirred for 20 min. In addition, 1.5 g PS pellets were added into 8.5 g of toluene. The solution was stirred at 50 °C for 2 hours to make PS pellets fully dissolved. The prepared tBA-DEGMA solution and PS solution were mixed at a weight ratio of 85:15 (2.55 g tBA-DEGMA solution and 0.45 g PS solution in this case) and stirred for another 20 min. Afterwards, the resultant mixture was cured in a Teflon open mold (without cap) with 365 nm UV light exposure for 15 minutes. The prepared SMP composites, namely, tDPS, were post-cured inside the fume hood for 24 h. The tDPS sample is cut into 10 mm × 2 mm × 1 mm strip for the mechanical tests and 25 mm ×3 mm ×1 mm for the shape recovery test. The entire synthesis procedures are shown in Figure 5.1.

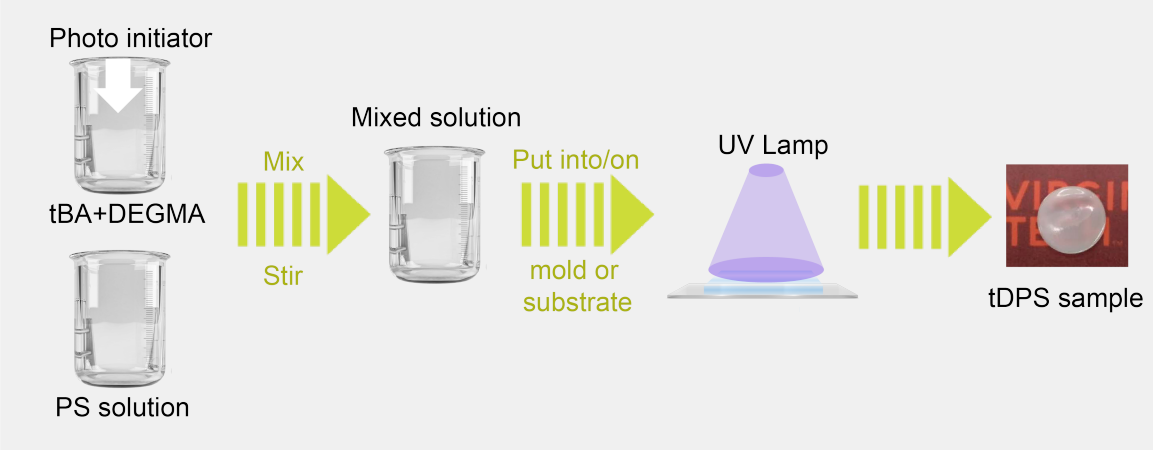

Figure 5.1: Schematic showing the processing steps to prepare tDPS composite.

To provide a comparison between tBA-DEGMA SMP (we will call it tD in all following sections for convenience), PS and the tDPS samples, pristine tD and PS samples were obtained by UV curing and drop casting method separately. Detailed synthesis method for tDs is in our previous paper [172]. For PS samples, 1.5 g PS pellets were dissolved into 8.5 g of toluene. The well-mixed solution was then dropped on a 25 mm×25 mm mica substrate (Highest Grade V1, Ted pella). A pristine PS film can be easily peeled off from the mica substrate after 24 h solvent evaporation in fume hood.

The uniaxial tensile tests and dynamic mechanical analysis (DMA) were measured by a universal testing system (MTS Tytron 250). The tensile tests were performed with strain rate 0.0067 s^{-1} (displacement control). In addition, dynamic mechanical thermal analysis is also done by a TA-Q800 DMA tester (TA Instruments, USA) to measure the storage modulus, loss modulus and tan delta for the samples. The oscillation frequency is 1 Hz, and the temperature is increased at a rate of 2 °C/min Differential scanning calorimetry (DSC) measurements were performed on a TA-Q200 DSC tester (TA Instruments, USA). The samples in the aluminum pans were analyzed under nitrogen condition at a heating rate of 5 °C/min. Testing cycles were run from 30 to 120 °C. In addition, the mechanical tests in the out-of-plane direction of the samples were conducted by a nanoindenter (Hysitron TI950, Eden Prairie, MN, USA). The peak load 500 μN was held for 1 s with a loading and unloading rates 50 μN/s. The depth at the peak loading is small enough to maintain a quasi-static state.

Molecular dynamics simulations were performed to investigate the crosslinking mechanism during the curing process of tDPS and tD. All simulations are implemented by the molecular dynamics simulator LAMMPS [200]. Two simulation systems, one contains tBA, DEGMA and PS monomers/chains, and another only contains tBA and DEGMA, were created by using the open-source package Moltemplate [201, 202] and Packmol [203, 204]. The post-

processing is processed by the software Ovito [205]. Each simulation takes around 4 hours on 48 CPUs.

5.3 Results and discussion

Samples made of PS, tD and tDPS, prepared by the methods described in the previous section are shown in Figure 5.2a. From DSC and DMA measurements (Figure A.1 - A.5), the glass transition temperature of PS is 95 °C, and the transition ranges of tD and tDPS samples are from 60 °C to 80 °C. Notably, although PS and tD are transparent polymers, tDPS, as a combined composite of PS and tD, is a type of white material with relatively low transparency. These samples are then cut into strips to perform uniaxial tensile test. It can be found that PS and tD are brittle while tDPS is a ductile material. As shown in Figure 5.2b, the stress of PS increases dramatically at the initial regime of strain and breaks at a strain level of 0.03. A pronounced increase also presents at the early stage of the stress curve of tD. The tD yields at a stress of 10.5 MPa, then breaks at 0.3 strain. In contrast, tDPS shows a significantly different stress-strain response. The material stiffness decreases prominent with an extended ductility. The young's modulus of PS, tD and tDPS are 597.24 MPa, 270.12 MPa, and 39.55 MPa, respectively. The maximum stress of tDPS during tensile test is 1.5 MPa, and the sample can be elongated to a strain of 1 without breaking. The possible reasons for this mechanical response variation will be investigated later by MD simulation.

The programming and shape recovery process of tDPS sheet is shown in Figure 5.3. The initially flat (permanent shape) tDPS sample is deformed to an angle of 5°. The deformed shape (intermediate shape) is programmed for 10 seconds. After the load releases, the bended sample will return to an angle of 50° automatically, because of the elastic component in the

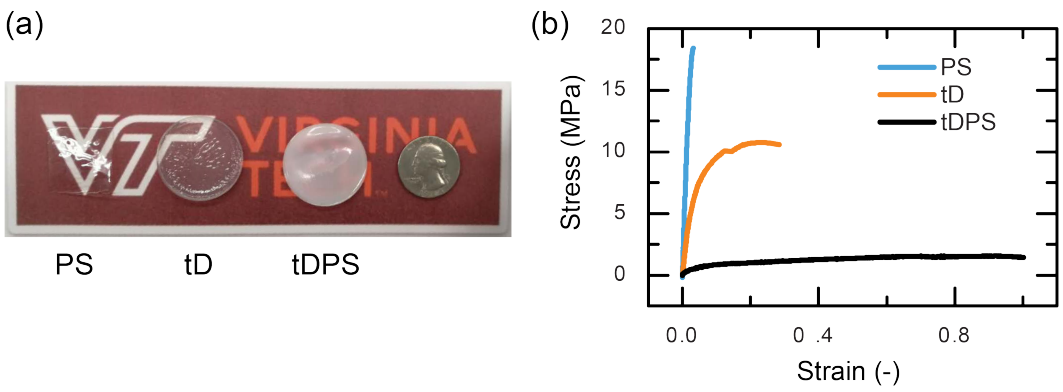

Figure 5.2: Digital image (a) and Stress-strain curves (b) of the PS, tD, tDPS samples.

material [197]. Subsequently, a regular hair dryer is used to apply hot air to the sample. As shown in Figure 5.3, it is observed the filament will return to their its initial shape ($\Delta = 175°$) within 2 seconds after heating by the hair dryer. In another scenario, the deformed composite is immersed into hot water (temperature 65 °C), that sample also shows a very fast recovery to its original shape (flat shape, $\Delta = 175°$). Notably, although bending has some limitations to characterize shape memory effect, such as the strain in bended area is not uniform [206]. However, bending is one of the most common-used and straightforward way to evaluate the performance of shape memory effects quantitively. Here, we still use bending and tracking the change of bended angle to characterize the shape recovery ability of the samples.

The synthesized tDPS is able to achieve good temporal and spatial effects. From Figure 5.3, tDPS sample has almost 100% shape recovery, which is 5 times more than the maximum shape recovery of tD (20%) shown in our previous work [172]. A very quick response (recovery in 2 seconds) is also observed when direct heat is applied. The better recover degree can be due to the improved thermal processability [164]. These results show that the tDPS has a remarkably better recovery ability compared to tD.

The tensile stress hysteresis loop of the tDPS sample is shown in Figure 5.4a. The test was performed with loading/unloading rate is 0.0067 s^{-1} without any peak load holdings. The

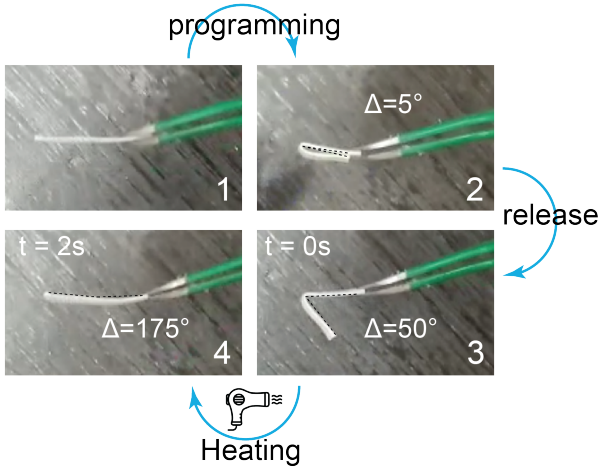

Figure 5.3: Illustrations of the programming and recovery of the tBA-PS sheet sample. See text for details.

large areas in the hysteresis illustrates the high viscoelasticity of the composite, given the fact that the loading and unloading locus will overlap for ideal elastic material [207, 208]. To further explore the mechanical properties of tDPS, the DMA test is performed. A 10% pre-strain is firstly applied on the sample, then the sample is subjected to cyclic loading and unloading with constant strain rates. The frequency is 1 Hz and the amplitude is 10% strain. In Figure 5.4b, there is a 56.14° phase lag between the stress-strain curves on average, which again indicates the high viscoelasticity of the tDPS sample.

It is worth noting that the viscoelasticity makes tDPS having a great potential for being actuated with HIFU. The vibration induced damping loss and viscous internal friction inside tDPS may result in obvious heating effect, even when the power level of the trigger (HIFU) is relatively low. In this way, the "onset" shape recovery temperature can be reached when subject to lower level acoustic power, which helps to avoid the unpredictable damage inside the polymer and easier actuation for soft actuator applications.

As shown in Figure 5.5a, the reduced Young's Modulus of the PS, tD and tDPS samples are 4.46, 3.72, and 0.02 GPa separately. Figure 5.5b compares the hardness of PS, tD

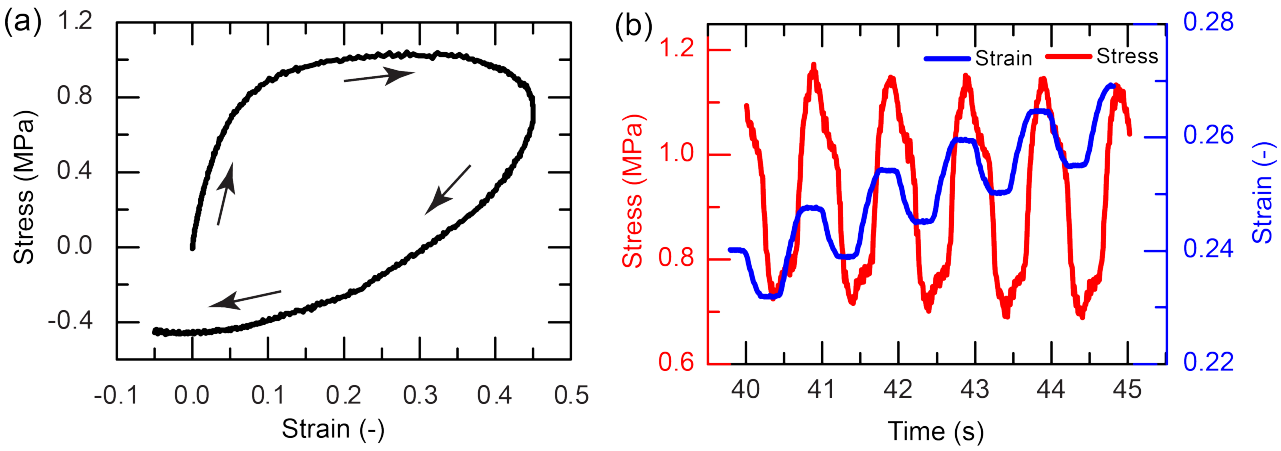

Figure 5.4: (a) Stress hysteresis loop of tDPS composites and (b) corresponding phase lags between stress and strain by DMA test.

and tDPS samples by nanoindentation. Figure 5.5c shows typical loading-unloading curves for the samples during the nanoindentation test. The tDPS sample shows a much larger indentation depth (displacement in the indenting direction) at the peak loading, because hardness depends on stiffness and strength. Grouping Figure 5.5a-c, these results correspond well with tensile tests results in Figure 5.2b.

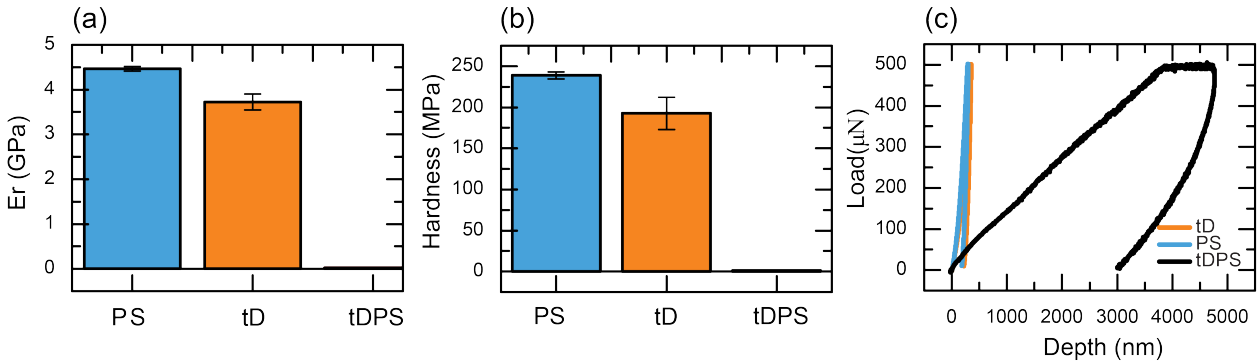

Figure 5.5: The reduced Young's Modulus (a), the hardness (b), and the load-displacement profiles (c) of the samples by nano-indentation tests.

A question that needs to be answered here is why tD and tDPS show totally different mechanical properties. As mentioned, tD is synthesized from the mixture of DEGMA and tBA, while tDPS is cured from the mixed solution of DEGMA, tBA, and PS. We hypothesize

PS plays an import role during the UV curing procedure, and investigate the potential mechanism with MD simulations. Figure 5.6a displays the schematic of UV curing process [191, 192]. The monomers of tBA would polymerize together into long chains, and finally form the crosslinked network with the crosslinkers DEGMA. Two MD simulation boxes are created with periodic boundary conditions in x, y, and z directions. Each simulation box contains 288 tBA monomers and 27 DEGMA crosslinkers (the mass ratio of tBA and DEGMA molecules are 85:15), separately. One of the boxes also has 27 short PS chains (chain length N = 8) inside. There are 1 active polymerization sites on every tBA molecule and 2 active crosslinking sites on DEGMA. A distance-based bond creation criterion for the polymerization and crosslinking is used. Specifically, a new bond will form when the distance of two active sites is shorter than 4.5 Å. Note that the new bond can only form between different molecules. To avoid sudden energy jump, which may result in non-equilibrium, the system will then equilibrate by NVT (constant substance amount N, constant volume V, temperature and constant temperature T) and NPT (constant substance amount N, constant pressure P, and constant temperature T) ensembles, as well as energy minimization process. After the systems reach equilibrium again, a new iteration can be started. CVFF potential force file [209] is used in all MD simulations. The motion equations in the simulations are integrated by velocity-Verlet algorithm with a timestep of 1 fs. The temperature is held at 330 K by Nose-Hoover thermostat with a damping constant of 0.1 ps.

The schematic representation of the polymeric system after polymerization and crosslinking (iteration = 100) is illustrated in Figure 5.6b. The polymerized and crosslinked sites are highlighted in yellow and orange, respectively. Figure 5.6c and d show the evolution of the number of crosslinked and polymerized sites. Grouping Figure 5.6b-d, it is found that the added PS can hinder the polymerization and crosslinking processes by 9.77% and 23.64%, separately, which prevent the mixture form a tightly crosslinked network during the curing

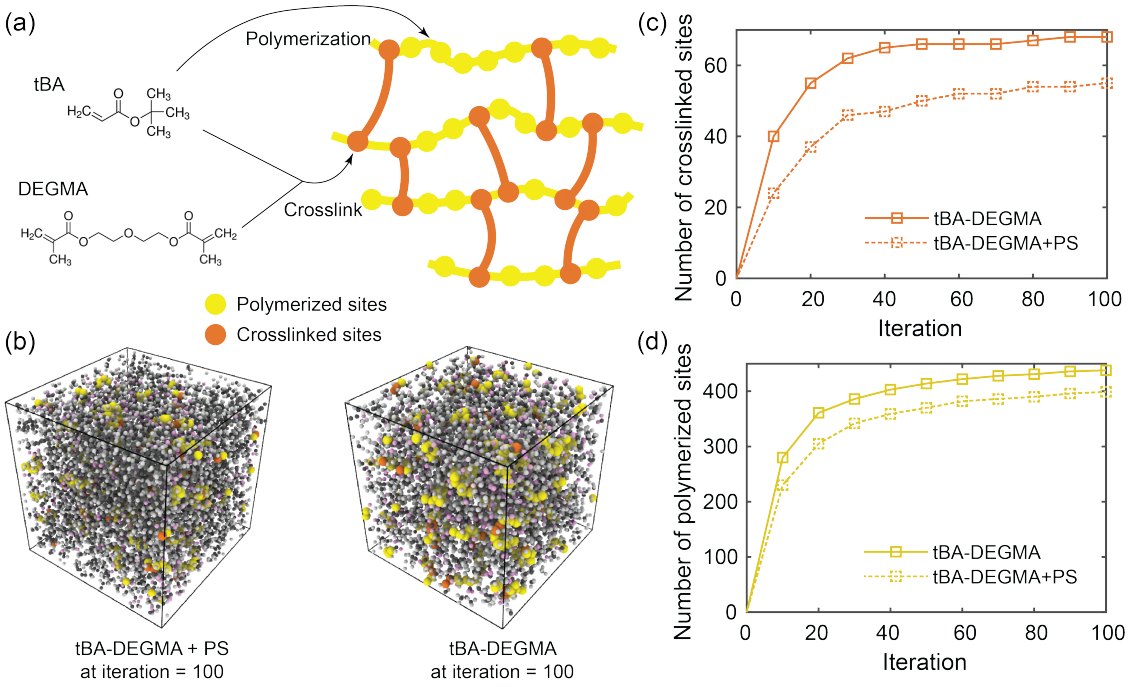

Figure 5.6: (a) Schematics of polymerization and crosslink of tBA (monomer) and DEGMA (crosslinker) during polymer UV curing process. (b) Representation of tDPS (tBA-DEGMA + PS) and tD (tBA-DEGMA) system in simulation box. Periodic boundary conditions are applied in x, y and z directions. (c) and (d) show the evolution of crosslinked sites and polymerization sites for these two systems for the entire curing process (iteration from 0 to 100).

process. Notably, the PS chain length in MD simulation is much shorter than in real experiments, so the quantitative values (9.77% and 23.64%) here only provides a lower boundary threshold. The decreased polymerization and crosslinking rates will result in shorter molecular chains and looser networks, which enables larger local molecular mobilities. Hence, the tDPS has a lower stiffness and hardness compared to the well-crosslinked tD. Additionally, short chains and the loose network can also yield to more liquidus behaviors, in other words, higher viscoelasticity. On the other hand, it is worth noting that pristine PS is a brittle material with relatively high stiffness. This is because lots of entanglements are inside the pure PS system. For tDPS in this case, PS chains are much less entangled due to the obstructs of tBA and DEGMA, which finally makes tDPS a ductile material.

5.4 Conclusions

In this study, a novel shape memory composite tDPS is synthesized, and systematically studied by experiments and molecular dynamics simulations. The composite exhibits enhanced shape recovery ability, which can reach almost 100% recovery ratio in 2 seconds triggered by hot air or water. From corresponding mechanical tests, the composite shows reduced hardness and relatively high viscoelasticity. Moreover, molecular dynamics simulations are also used to study the related mechanisms. It is found the added PS can lower the polymerization and crosslinking ratio during curing process, in which alters the mechanical properties. Overall, these results indicate tDPS a promising material for the application of shape memory polymer based devices, and the corresponding computational works paves the way in front of understanding the mechanism and optimizing the design for SMP devices.

Chapter 6

A two-way shape memory polymer for soft actuator applications

6.1 Introduction

Soft actuators made by soft smart materials have attracted tremendous interests owing to their great potential for the robotic applications [210, 211]. They are capable of generating desired motions and forces/torques, such as gripping [212], climbing [213], running [214] and leaping [215], under external stimuli. Among the smart materials, shape memory polymers (SMP) have been extensively studied due to their extraordinary advantages, including large output forces, simple manufacturing, and low cost [216]. Although SMPs have the ability to recover to the permanent shape under external stimuli (e.g., heat, light, pH, electric field, etc), a large majority of SMPs only have irreversible shape recovery property without re-programming applied, which is also known as "one-way shape memory effect" [217]. In general, the irreversible shape memory effect of SMPs hinders their practicability for further applications.

SMPs with reversible shape memory effect (aka. two-way shape memory effect) have been recently investigated due to their shape-programmable behavior, showing a broad applicability in soft actuators and robots. The liquid crystal elastomers (LCE) is one of the most widely used two-way SMPs because of their large deformation recovery as large as 300% [9].

For example, Ware et al. [218] synthesized a liquid crystal elastomer which can form complicated 3D structures upon heating and recover back to original flat shape automatically when cooled to room temperature. Shahsavan et al. [215] fabricated a kind of light-actuated liquid crystal gels which can accomplish many complex motions, such as walking and leaping. However, the inherent low stiffness of the LCE (usually less than 1 MPa) generally becomes a serious hindrance for the soft actuators requiring high load capacity [219]. Therefore, the crosslinked poly(ethylene-co-vinyl acetate) (cPEVA) based two-way shape memory polymer owing a relatively higher stiffness may be a promising candidate for using in soft actuators adapting to a diverse range of applications.

The poly(ethylene-co-vinyl acetate) (PEVA) are usually utilized as adhesive and structural materials due to their outstanding adhesion property [220] and remarkable mechanical properties [221], respectively. Recently, the two-way shape memory effect of cPEVA based polymers has been unveiled by Behl et al [222]. Subsequently, they are attracting a great deal of attention for applications in the soft actuator domain. On the other hand, the as-formed cPEVA as one copolymer network exhibits high stiffness which enables the final systems to realize the desirable forces and torques output. Up to date, several studies have been performed on the cPEVA based two-way SMPs. For example, cPEVA based thin film with a well-designed pattern and reversible thermally-induced actuation has been successfully fabricated by Liu et al [223], which may be beneficial for the potential soft actuator miniature. Yang et al. [224] studied the use of hierarchical chiral cPEVA fibers to fabricate artificial muscles. Hui et al. [225] and Gao et al. [226] also found that the different crosslinker combinations can significantly affect their two-way shape memory behavior, mechanical and thermal properties. However, to the best of our knowledge, the cPEVA based two-way SMPs as one kind of smart materials for various applications have not been sufficiently explored.

In this work, cPEVA samples using dicumyl peroxide (DCP) as the crosslinker have been

successfully fabricated. The effect of the DCP concentration on the mechanical properties at different temperatures and the two-way shape memory behavior is systematically studied. On the other hand, the cPEVA samples can be tailored into multiple shapes depending on the predefined ways (e.g., spiral and screw shape). More critically, cPEVA based soft actuators, including a gripper and a self-rolling structure, are also manufactured, indicating that the as-synthesized cPEVA possesses not only large output force, but also excellent shape recovery property. Furthermore, finite element analysis is also conducted to study the related mechanisms controlling the self-rolling motion. This investigation provides important insights in designing smart materials with high performance for a variety of advanced applications.

6.2 Materials and methods

The PEVA pellets with 18 wt% vinyl acetate (VA) and the DCP are purchased from Sigma-Aldrich without further treatment. Figure B.1 illustrates the cPEVA preparation procedure. Firstly, 2 g PEVA pellets and different amounts of DCP (i.e., 2 wt%, 4 wt%, 6 wt%, and 8 wt%) are mixed in 20 mL of toluene (anhydrous, 99.8%, Sigma-Aldrich) at 70 °C with magnetic stirring for 2 h. Then the solution is transferred into a Teflon mold, and air dried in a fume hood for about 2 days. When the toluene is fully evaporated, the bulk PEVA and DCP mixture is collected and loaded in an aluminum mold which is pre-applied with demolding agent. Finally, the cPEVA sheet sample can be obtained after curing in a hot press (Genesis, Wabash, IN, USA) at 200 °C with 20 bar pressure for 15 min.

The mechanical properties of the cPEVA samples are measured by a dynamic mechanical analyzer (Q800 DMA, TA Instruments). The tensile tests of the samples obtained with different DCP concentrations are performed at both room temperature (i.e., 25 °C and 70

°C. The storage and loss moduli of the sample with 6% DCP are swept from 25 °C to 85 °C at 10 Hz by dynamic mechanical analysis (DMA) test. The XRD profiles of the samples are measured by an x-ray diffractometer (PANalytical x'pert pro). The differential scanning calorimetry (DSC) tests of the samples are conducted using a commercial DSC unit (Q200 DSC, TA Instrument) with a heating/cooling rate 5 °C/min in running N2.

6.3 The effect of DCP concentration

The influence of the crosslinker (DCP) concentration on the mechanical property of cPEVA is firstly investigated. Figures 6.1a and b display the typical stress-strain curves of the cPEVA samples obtained with different DCP concentrations (i.e. 2%, 4%, 6%, and 8%) at 25 °C and 70 °C, respectively. As shown in Figure 6.1a, all the samples have similar Young's Modulus (15 MPa), and all the samples yield at about 2.5 MPa and 25% strain. This implies that the DCP concentration has an insignificant effect on the elasticity and yielding stress of the cPEVA. Wang et al. [227] found that the elasticity and yielding of cPEVA are mainly determined by its crystallinity. Improving the crystallinity by increasing the content ratio of the polyethylene (PE) to VA results in the mechanical properties enhancement of cPEVA. This also means that the DCP concentration cannot significantly alter the crystal phase of cPEVA. However, it can be noted that the ultimate strains of the cPEVA samples decrease as the DCP concentration increases. For example, when the strain is larger than 350%, the 2% DCP sample does not break and is well-maintained, while the other samples are fractured (i.e., the 4% DCP sample, 6% DCP sample, and 8% DCP sample break at 350%, 280%, and 220% strain, respectively). This may be because a higher crosslinking concentration results in more interactions between the polymer chains to prevent them from sliding over each other. Similarly, Figure 6.1b shows that the ultimate strains decrease from 300% to

50% with the DCP concentration increasing from 2% to 8% at 70 °C. On the other hand, the cPEVA samples exhibit reduced mechanical properties at 70 °C compared to the room temperature. For example, the Young's Modulus is reduced to 3.3 MPa, and the yielding points (0.45 MPa) become less clear.

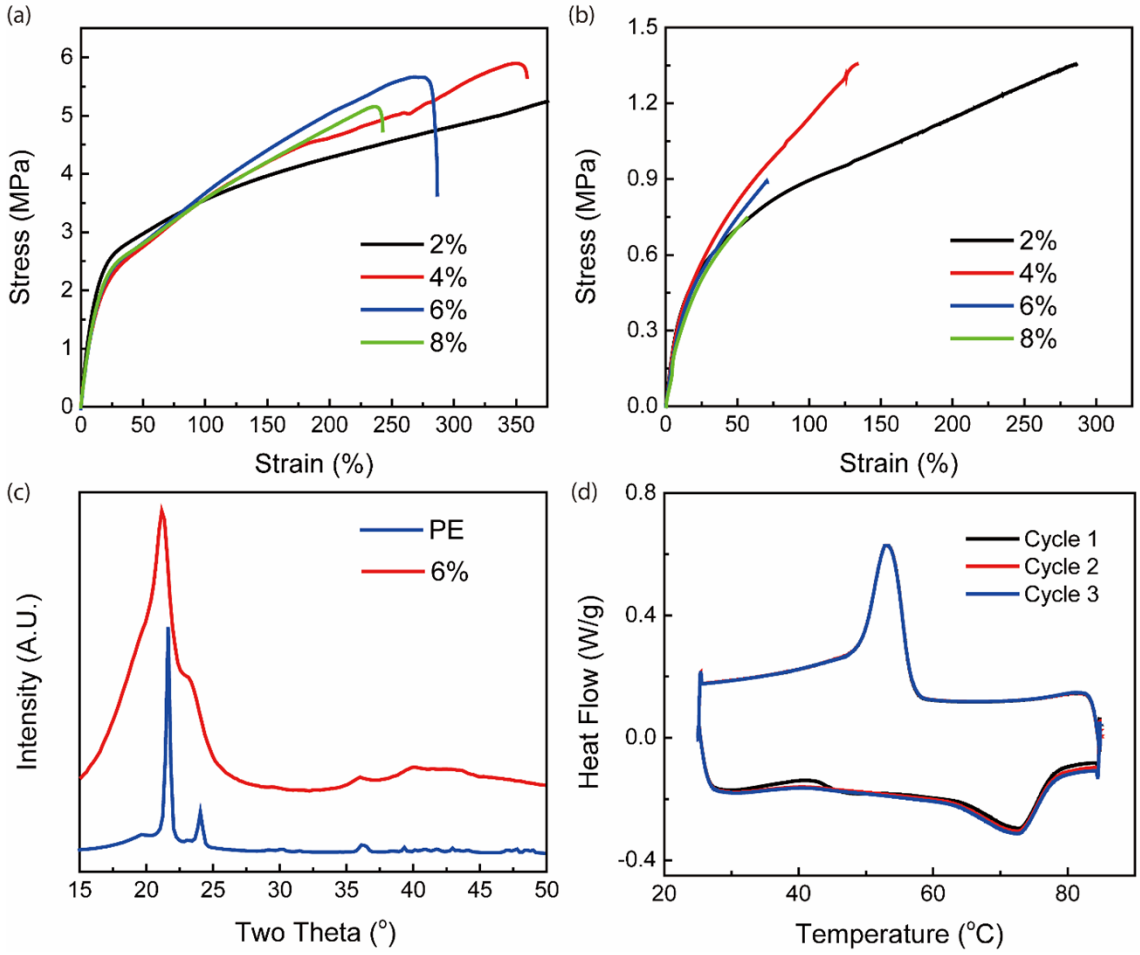

Figure 6.1: The stress-strain curves of the cPEVA samples with different DCP concentrations at (a) room temperature and (b) 70 °C. (c) The XRD profiles of the 6% DCP sample (red) and a commercial polyethylene sample (blue). (d) Three DSC cycles of the 6% DCP sample (black, Cycle 1; red, Cycle 2; blue, Cycle 3).

The XRD patterns of the cPEVA and pristine PE samples are shown in Figure 6.1c to further investigate the nature of their crystallinity. For the cPEVA sample, the peaks at 21.1° and 23.2° match well with the previous studies by Wang et al. [227] and Aradhya et al.

[20]. The polyethylene sample has two prominent peaks at 21.6° and 24.0°, corresponding to the (110) and (200) diffractions, respectively [228, 229]. The similar peaks and intensities between these samples imply that the crystal phase in cPEVA mainly depends on the PE content. However, it is also clear that the XRD patterns of cPEVA exhibit both peak shift and broadening compared to pristine PE. The reason may be that the VA content of cPEVA can significantly alter the crystal structure of the PE content. Figure B.2 shows the XRD profiles of the cPEVA samples with different DCP concentrations. In general, the XRD peaks are very similar among all samples, implying again the DCP concentration would not significantly alter the crystal structure of cPEVA.

Figure 6.1d presents the typical DSC curves of the 6% DCP sample based on three heating/cooling cycles. There are minimal changes in the melting temperatures, indicating high thermal repeatability and stability of cPEVA. Figure B.3 illustrates the DSC curves of the cPEVA samples with different concentrations. It can be noted that increasing the DCP concentration shifts the melting point to a lower temperature. Gao et al. [226] reported that the crosslinker concentration can significantly affect the crystallinity of cPEVA which dominates the melting and consolidating behavior. Hereby, the shifting-down of the melting point in this work may be attributed to high crosslinker (e.g., DCP) concentration induced weakening the crystallinity of the cPEVA.

The influence of the DCP concentration on the two-way shape recoverability of samples is also studied. The thermally induced shape memory behavior (e.g., opening and recovering) of the cPEVA samples can be visually demonstrated in Figures 6.2a-d. Here, the bent samples are heated in hot water at 75 °C and cooled in cold water at 25 °C. It can be found that both the 2% and 6% DCP samples tend to recover back to the permanent shape when dipped in the hot water bath. However, the 6% DCP sample shows a nearly complete recovery with a fast response, while the deformation of the 2% DCP sample cannot be fully recovered in

even longer cooling time. The measured shape recovery ratio as a function of cooling time is displayed in Figure 6.2e. It is obviously observed that the 6% DCP sample can fully recover within 2 s, while the 2% DCP sample only has around 60% shape recovery ratio after 4 s. This means that the 6% DCP sample exhibits relatively higher recovery speed and shape recoverability compared to 2% DCP sample. It is concluded that the shape memory behavior of cPEVA in our work is highly dependent on the DCP concentration.

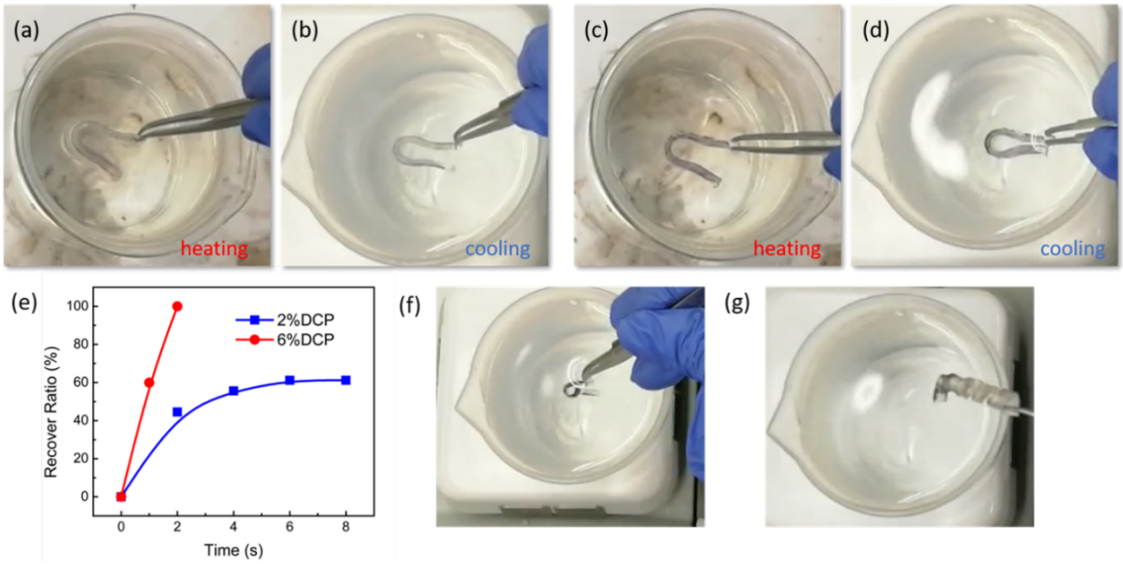

Figure 6.2: The digital images of the two-way shape memory effect of the bended 2% (a, heating; b, cooling) and 6% (c, heating; d, cooling) DCP samples. (e) The shape recovery ratios of the 2% and 6% DCP samples as a function of cooling time. Digital images of the (f) spiral and (g) screw shape of 6% DCP sample.

As aforementioned, increasing DCP concentration can enhance the two-way shape memory effect in terms of the response time and shape recoverability (see Figure 6.2e). However, correspondingly, the mechanical properties (especially strength at high temperature) will be significantly compromised (see Figures 6.1a and b). Further increasing the DCP concentration leads to the sample fracture during the programming process at a high temperature (e.g., 95 °C). Hereby, 6% could be the optimal DCP concentration for the trade-off between the mechanical and shape memory property. Figures B.4a and b further illustrate the two-way

shape memory effect of the 6% DCP sample. The recoverable angle can be up to 30°, which is roughly three times larger than the previous study by Gao et al. [218]. Furthermore, we found that the two-way shape memory effect of the 6% DCP sample is still well maintained undergoing successive heating/cooling cycles. This indicates that the as-synthesized cPEVA sample possesses high thermo-mechanical stability.

Furthermore, the shape memory effect of cPEVA samples with multiple shapes (e.g., spiral and screw shape) has also been successfully proved (see Figures 6.2f and g). Figures S4c and d exhibit that the spiral shape has an approximately 90o overall shape recovery. The two-way shape memory property of the screw shape is demonstrated in Figures B.4e and f. It can be seen that the end of the sample in the screw shape can spin freely and recover for more than one revolutions driven by the temperature. This indicates that the cPEVA samples own good designing versatility in terms of their programmable architectures, which may benefit the related applications in soft actuators which are intended to perform complex motions.

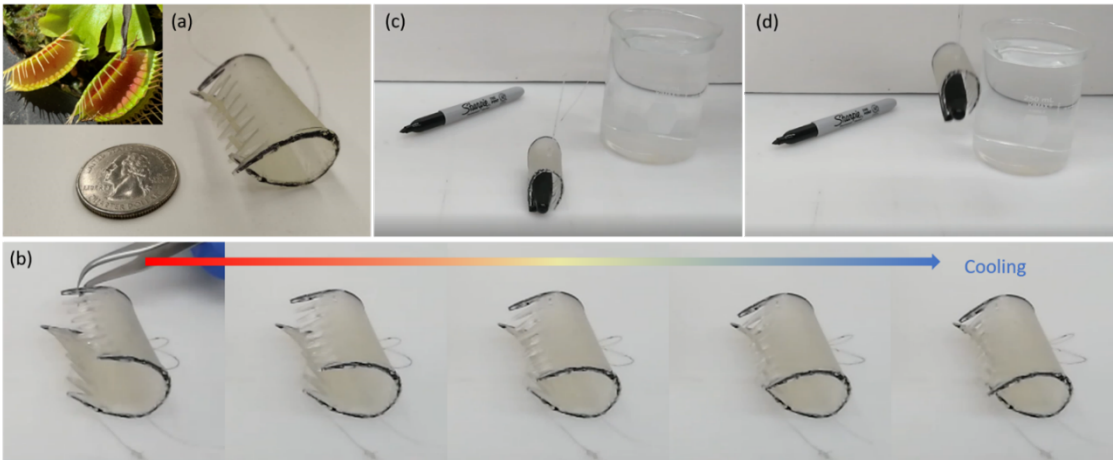

Figure 6.3: (a) The digital image of the cPEVA gripper, where the inset shows the optical image of the venus flytrap. (b) The process of the cPEVA gripper closure when cooling naturally in air. Grasping (c) and lifting (d) of a marker pen cap.

6.4 Applications in soft actuators

Soft actuators based 6% DCP sample are fabricated to further demonstrate the designing versatility of as-synthesized cPEVA. As shown in Figure 6.3a, a Venus flytrap-inspired cPEVA soft gripper with teeth assisting gripping has been fabricated. Figure 6.3b display the closure process of the cPEVA gripper initiated by natural cooling in air. Here, the gripper gradually closes in air followed by opening upon heating in 75 °C water. Notably, the closure speed of cPEVA gripper in air is much slower than the responsive speed of bending/opening in hot/cold water bath. This means that the cPEVA is actuated by temperature difference instead of the heating/cooling rate. However, the response speed is significantly dependent on the heating/cooling rate. As shown in Figure 6.3b, the cPEVA gripper can completely return back to its original shape when fully cooled. Figures 6.3c and d show that the cPEVA gripper is able to grasp a regular marker cap. This indicates that the large output forces of cPEVA enable the corresponding soft actuators and robots adapting to complex systems requiring high load capacity, which may be advantageous over other two-way SMPs, such as liquid crystals.

Additionally, a cPEVA self-rolling structure in a pentagon shape (1.7 cm in edge length and 2 cm in depth) is manufactured with the 6% DCP sample (see Figure B.4a). The self-rolling pentagon structure can indicate the output torque magnitude. On the other hand, it is also a basic concept which can be further expanded with more sophisticated structures [230]. The pentagon frame is made by regular cardboard, and each side has a bended cPEVA serving as the actuators. The total mass of the structure is 5 g while each cPEVA is around 0.74 g. The self-rolling process is visually demonstrated in Figures 6.4a-h. In this work, the structure is rolling on a hot surface with 90 °C. Notably, the structure is able to roll for more than one revolutions as shown in Figures 6.4a-h.

For the first rolling step, the 1st cPEVA actuator closely contacted the hot surface is heated, leading to the cPEVA opening. Figures 6.4a and b display the first rolling step is initiated by the cPEVA actuator opening. As shown in Figures 6.4c and d, when the opening angle of the 1st cPEVA is large enough to elevate self-rolling structure to an unbalanced state, the structure will roll one step forward. Subsequently, the next (2nd) cPEVA actuator contacts the hot surface and is actuated by heating. In the meantime, the previous (1st) cPEVA actuator detaches from the hot surface, which causes shape recovery (cPEVA folding) due to cooling. In this manner, the structure realizes self-rolling on the surface step by step driven by the temperature change.

Nonetheless, in order to initiate the second self-rolling revolution period, it is necessary to cool down the hot surface. As abovementioned, the cooling rate of cPEVA is relatively low in air. Therefore, the hot surface should be cooled when the 5th cPEVA actuator starts to contact the surface, as shown in Figure 6.4e. In this way, as shown in Figures 6.4f and g, the subsequent (1st) cPEVA can be gradually cooled and recovers back to its initial bended shape. Then the surface is heated up to 90 °C again, and the second self-rolling revolution period is initiated. Figure 6.4h displays the first self-rolling step in the second revolution period. Consequently, the structure can move forward step by step by iterating the previous process.

To investigate and understand the mechanisms of the self-rolling, a simulation with finite element analysis is conducted. The simulation model is illustrated in Figure B.5b. The simulation is implemented by a commercial finite element software Abaqus (version 6.14, Dassault Systems Simulia Corp., USA) with a user material subroutine (UMAT). The modified UMAT calculates the updated stress and the local tangent stiffness matrix of materials, in order to model the deformation and shape recovery of SMPs. Related details can be found in our previous study which provides a typical constitutive model for SMPs in the

finite element simulation [231]. Figures B.5c and d show the input properties of materials including the storage modulus, loss modulus, and Tan Delta sweeping with temperatures for the simulation. The DMA properties are measured with 6% DCP sample at 10 Hz. The results correspond well with the previous study by Wang et al. [227]. Figures 6.4i-k show the self-rolling process simulated by the finite element method. It is notable that the cPEVA actuator starts to open up when contacting the hot surface, which resembles the experimental results. Furthermore, the internal stresses are generated, which is attributed to the shape recovery. As the temperature increases, the internal stresses start to gradually propagate up in the hinge area, corresponding to the heat transfer direction. Therefore, it can be speculated that the localized internal stresses inspired by heating serve as the driven force for the cPEVA opening. As shown in Figure B.5e, when the center of the pentagon surpasses the reference line (dashed), the structure will roll one step forward due to the loss of balance. In summary, the self-rolling structure made by cPEVA indicates that the cPEVA is able to produce large output force and recover shape from large deformation. This study may provide important insights in preparing smart materials for advanced soft actuator applications.

6.5 Conclusion

In this chapter, a crosslinked poly(ethylene-co-vinyl acetate) based two-way shape memory polymer has been successfully synthesized by using dicumyl peroxide (DCP) as the crosslinker. Moreover, the effect of the DCP concentration on the mechanical properties and the two-way shape memory properties has also been systematically studied. It is observed that increasing DCP concentration can enhance the shape memory effect but weaken the mechanical properties. Finally, the 6% DCP cPEVA with high responsive speed and shape

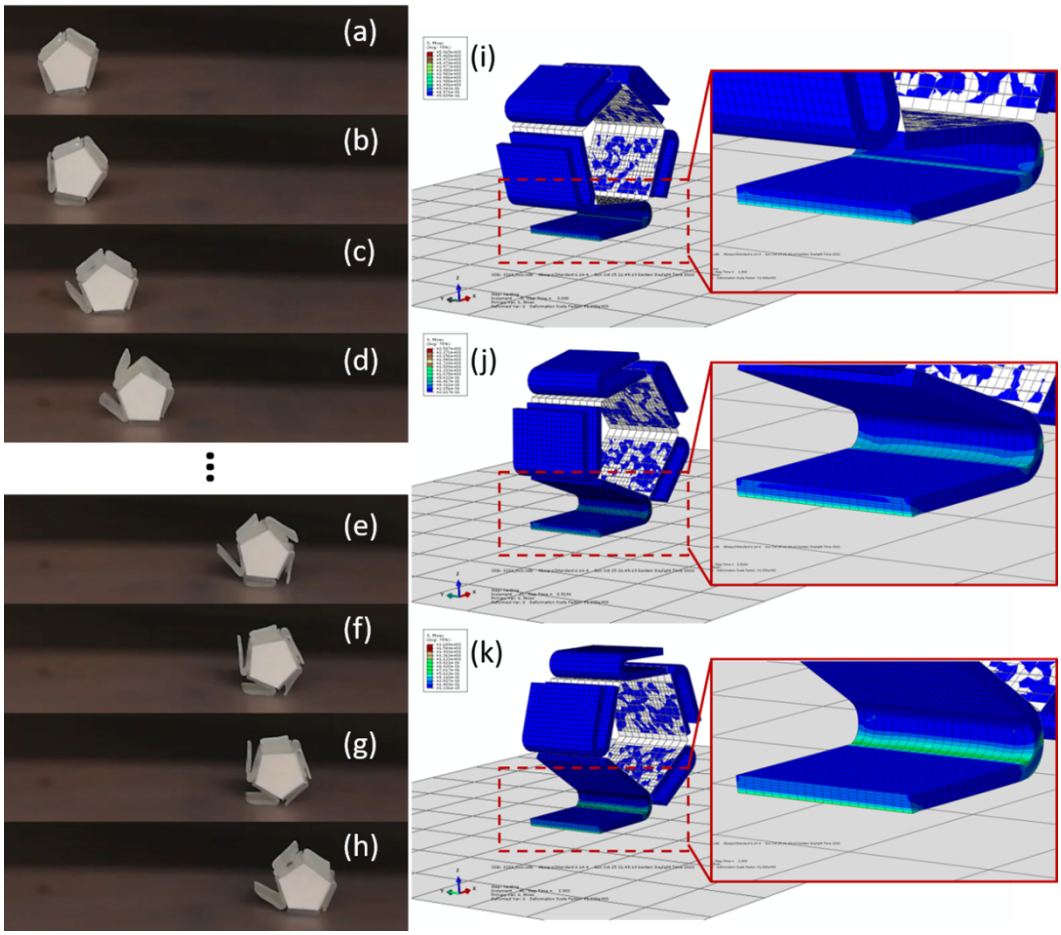

Figure 6.4: The first several steps of the pentagon sample self-rolling on a 90 °C hot surface (a-d). The pentagon sample cools down in air (e, f). The sample is reheated again (g). The second self-rolling cycle initiates (h). One single self-rolling step is simulated with finite element method (i, j, k).

recoverability is found to be the ideal material for the fabrication of soft actuators. Additionally, soft actuators made by cPEVA, such as the bio-inspired gripper and the self-rolling structure can perform complex motions, which indicates that the as-prepared cPEVA has the ability to produce large output forces and recover shape from large deformation. Furthermore, finite element simulations are also conducted to investigate the mechanisms controlling the self-rolling behavior. It is found that the realization of self-rolling is due to the internal stress propagation which is activated by temperature-induced shape memory behavior. This

provides important insights into the design of smart materials for the potential soft actuator applications.

Chapter 7

The effect of evaporation during nanofiber formation process

7.1 Introduction

Polymeric nanofibers are unique one-dimensional materials formed by the solidification from viscous polymeric solution. The widely used fabrication methods for production of polymeric nanofibers are electrospinning, cold-drawing, hot-drawing, etc. Their continuous structure, nanoscale dimension and relative ease of preparation process make them valuable materials in many engineering applications, including heat conversion, energy harvesting, biomedical engineering, as well as controlled drug delivery. Their microstructure and the corresponding mechanical properties, including the molecular orientation, forming of crystalline structure and the size effect, as well as the so-called core-shell structure also make them a very interesting nano-material in research fields.

It has been reported that when the diameter of the nanofiber keep decreasing, the corresponding mechanical properties; e.g. Young's modulus and ultimate strength changes significantly, especially when the diameter is dropping below a critical value. We call it the size effect of nanofibers, and this critical value is defined as "onset" diameter. Many experimental and theoretical works indicate these changes in the mechanical properties of the nanofibers are strongly associated with the variation in the microstructre at nanoscale.

The experimental studies of the structure of nanofibers can be mainly categorized into two parts, measurement of a bundle of fibers and measurement of a single fiber. The measurement of bundle can provide the information about the fiber aliment at macroscale. With the help of XRD and IR, the crystallinity and the chain orientation of nanofibers can also be partially investigated. Due to the relatively high noise-to signal ratio, these experiments can only provide a qualitatively analysis. Studies at single chain level provide more insightful and direct information, and can pave the way in establishing a rigorous link between the unique size effect of mechanical properties of nanofibers and the evolution of microstructure inside nanofibers. However, all these studies are non-dynamics structural analysis. It is still difficult to investigate the dynamic formation process of nanofibers, which the final structure of nanofibers will be heavily depending on the formation factors, such as the drawing force and solvent evaporation ratio.

Recently, it has been reported that the fiber internal nanostructure strongly depends on the elongation or stretching force during the fiber fabrication process. By utilizing the transmission electron microscopy (TEM), infrared, Raman and small-area electron diffraction, researchers found polymeric nanofibers usually have a core-shell structure, as schematically shown in figure 7.1 [16, 17]. However, the results indicated contradictory views on the detailed micro-structure distribution about the core-shell structure. Stachewicz and co-works [17] reported that electrospun fibers have a composite structure consisting of a shell region of aligned polymer chains surrounding a bulk-like isotropic core. The anisotropic shell region has higher density than the core region. On the other hand, Camposeo et al. [16] investigate the nanoscale spatial variation of the polymer density. They found polymeric nanofibers present a dense internal core embedded in a less dense polymeric shell. Interestingly, nanoscale mapping the fiber Young's modulus demonstrates that the dense core is stiffer than the less dense shell area.

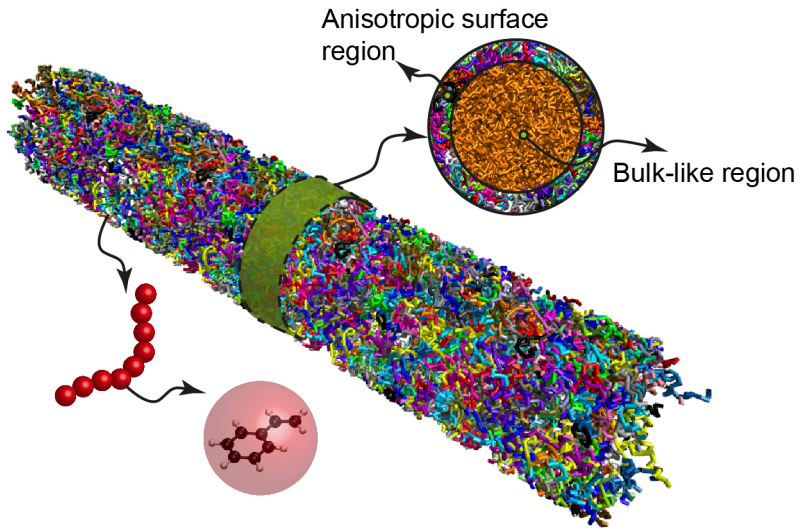

Figure 7.1: Illustration of the core-shell structure of polymeric nanofibers.

A hypothesis has been proposed that the network conformation during fiber fabrication process depends on the balance between stretching and evaporation. Dominant evaporation can cause rapid solidification of the jet surface, retarding evaporation from the core, and resulting in a tubular structure. On the other hand, dominant strain rates will cause higher polymer density in the center due to stretching. However, due to the changeling from the experimental side. This hypothesis have not been fully validated yet. There are still many debates in this field.

In this chapter, the influence of evaporation on nanofiber forming process is investigated by molecular dynamics simulation. First, two coarse-grained models, a coarser Kremer-Grest bead-spring model [232] or a two-bead per monomer coarse-graining model [233], will be used separately to evaluate which one would be better fit for capturing the fiber formation phenomenon. To simulate the evaporation more accurately and physically, MISC package in Lammps is used to simulate the evaporation process, M solvent atoms/molecules will be deleted every N steps. By adjusting the values of M and N, the evaporation rate is under control. Detailed simulation procedure is presenting in the following sections.

7.2 Generic polymeric model

7.2.1 Models and potential force fields

All the simulations are performed by using the open-source molecular dynamics simulation software, Lammps. We employed a well-known generic polymeric bead-spring model, which is based on Lennard-jones (LJ) potential. The potential force filed we used it here have two components, the bond interaction and the non-bond interaction. The pair potential (non-bond part) can represent by the following governing equation,

$$E = 4\epsilon[(\sigma/r)^{12} - (\sigma/r)^{6}]$$

where σ is the bead diameter, r is the distance between two beads and ϵ is the binding energy. The bond interaction can be represented as,

$$E = -0.5KR_0{}^2 \log[1 - (r/R_0)^2] + 4\epsilon[(\sigma/r)^{12} - (\sigma/r)^{6}] + \epsilon$$

where $K = 30\epsilon/\sigma^2$ and $R_0 = 1.5\sigma$ is the maximum possible bond length for FENE bond.

The initial geometry of the system is generated by the self-avoid random walk algorithm. Polymeric chains are randomly placed inside the cubic simulation box. Next, periodic boundary conditions are turned on in all three dimensions (x, y, z directions). A series of quenching process are performed in order to equilibrate the whole system. After the system reach equilibrium, random positioned solvent atoms (LJ liquids) are also put inside the system. The system goes under a second round equilibrium again. After that, periodic boundary conditions are turned off in x and y directions, and the corresponding directions are expanded 2 to 3 times. Next, we apply a NPT ensemble in z-direction. Under these conditions, the

system can form a cylindrical shape.

The polymer/solvent systems are then treated by cylindrical wall confinement. the cylinder diameter decrease from 60σ to 23.1σ slowly. For these polymer chains, bonds between two different chains are allowed to swap following Monte Carlo rules using the Boltzmann acceptance criterion. The purpose is to equilibrate the polymer chain conformations more rapidly than dynamics alone would do it. When the whole systems are fully equilibrated, we decrease the temperature from $T = 1.0\epsilon/k_B$ to $T = 0.1\epsilon/k_B$. To mimic the fiber drawing and evaporation process, a wall potential with attractive potential is put below the bottom end of the as-made cylindrical system and a force is added at the top part of the system. The illustration of the setup is shown in Figure 7.2. "fix evaporation" command in Lammps are used to mimic the evaporation process. When the solvent is flying to the outer surface of the nanofiber (targeted region), one particle will be deleted every one timestep.

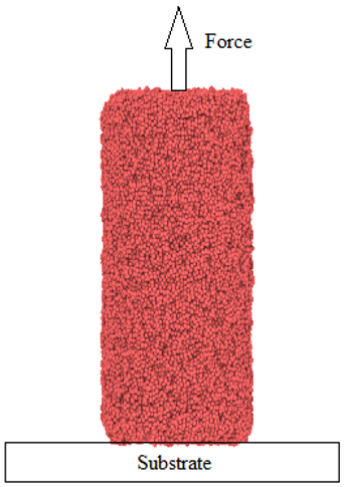

Figure 7.2: Illustration of the nanofiber drawing setup.

7.2.2 Results and discussion

Figure 7.3 shows the final cylindrical system in equilibrium state before stretching and evaporation. It can be observed that the initial geometry of the cylindrical system is in amorphous state. While some solvents are attached at the surface of the fiber, there are also many solvent beads inside the system. This is similar like the fiber solution in dilute state at the beginning of drawing (fabrication by drawing) state.

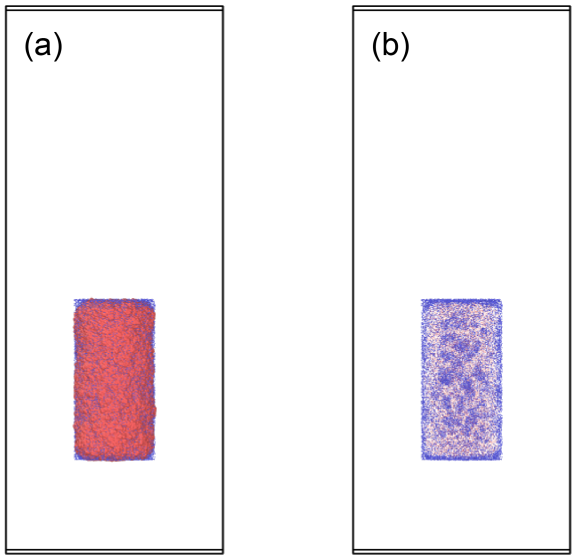

Figure 7.3: Cylindrical system in equilibrium state before pulling and evaporation

In the following two cases, we fixed the evaporation rate. Two different forces are added in the top part of the fiber, which indicate fast-stretching and slow-stretching. Although the evaporation rate is unchanged, but we can still categorised these two cases as: 1. evaporation is dominant; 2. stretching (drawing) force is dominant. Figure 7.4a shows the final geometry after applying a relatively small force. To clarify the distribution of the solvent beads inside the fiber, the radius of the beads in the nanofiber are set to 0.01σ in Figure 7.4b. It is shown the solvent beads at the surface of the nanofiber are evaporating fast, which cause a rapid solidification. Interestingly, although the evaporation is very fast, there are many liquid beads trapped inside the core area of the nanofiber. Such kind of phenomena will cause

a less dense core area of the nanofiber and a dense shell area, which result in a tabulated nanofiber structure.

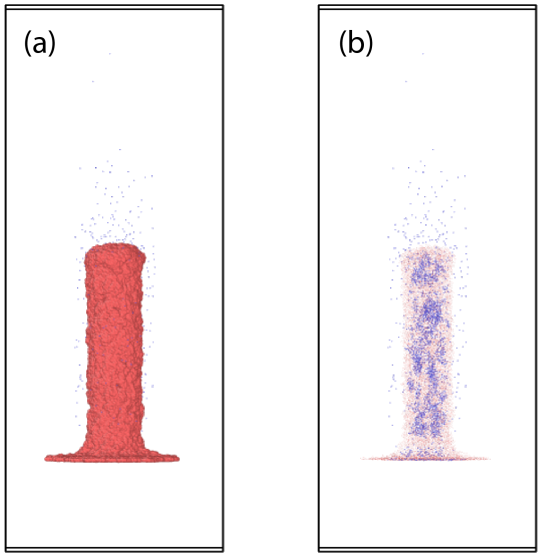

Figure 7.4: Stretching with a relatively small force.

When the stretching force is relatively large. the nanofiber is elongated fast, as shown in Figure 7.5a. We can find there are two points which are significantly different between this case and the former one. First, when the drawing force is large, there is a compacting phenomenon. The diameter of the nanofiber becomes thinner. In this way, some liquid beads which are previously trapped inside the nanofiber are squeezed out. Another point is that there are some tiny voids on the surface of the as-spun nanofiber. These voids will also help the liquid beads fly outside. Note that these tiny voids may disappear in the real experiments due to further relaxation. In Figure 7.5b, we can monitor that there are much less liquid beads inside the nanofiber at the elongation section. In addition, if we compare the molecular orientation of the nanofiber in these two cases, we can find the nanofiber made by slow drawing tend to have a more amorphous structure. However, the chains are more aligned when the nanofiber is suffering from a fast stretching. Thus, we can claim the nanofiber made by fast stretching will have a denser structure compared to the fiber made

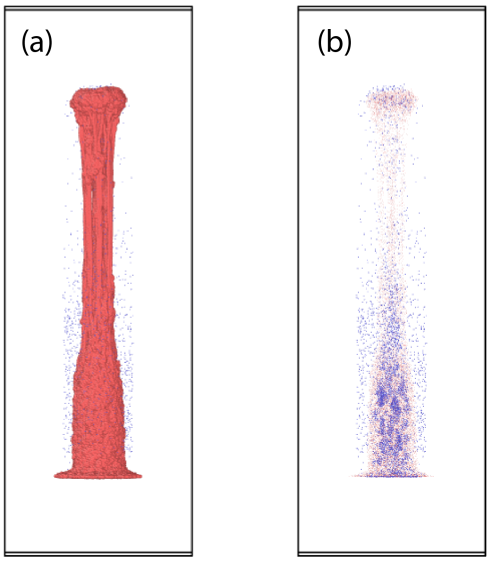

Figure 7.5: Stretching with a relatively large force.

by slow stretching.

In conclusion, the formation of the microstructure of nanofibers depends on the balance between the drawing force and the evaporation rate. By using molecular dynamics simulation, it is found that when the evaporation is dominant, fiber tend to form a tabulated structure with less dense core embedded with more dense shell layer. However, when the stretching force is dominant, the fiber may form a denser structure with chains more aligned. These molecular dynamics simulation results are consistent with hypothesis which is proposed in the previous experimental study.

Contribution

1. The origins of the size effects in PE and PS nanofibers are found differently. For PE nanofibers, our results show that the increased chains alignment and the formation of the crystalline structure are the main reasons for the increase of the strength and modulus of PE nanofibers. For PS nanofibers, which are usually amorphous without any crystalline structures, the increased chain alignment and backbone bond length are two critical reasons. The increase of ultimate strength is found to be more related to the linearly increased chain alignment while the variation in Young's modulus is directly attributed to the exponentially increased backbone bond length.

2. For the first time, the diameter of the modeled PS nanofibers in MD could be directly comparable to the experimental scale.

3. For the first time, an experimentally-validated acoustic-thermoelastic mathematical framework for modeling the focused ultrasound -induced thermal actuation of shape memory polymers is presented. The results from our finite element framework fits the experimental data very well.

4. For the first time, the influence of the evaporation during nanofiber formation process is investigated by using molecular dynamics simulation. Our results validate the hypothesis that the microstructure of the nanofiber is because of the balance of drawing force and the evaporation rate during fiber formation process.

5. The HIFU-induced thermal effect on PE was systematically studied by experiment and molecular dynamic simulation. We found that the HIFU-induced thermal effect is different for HDPE and LDPE. The heating rate of amorphous LDPE is remarkably larger than the

crystalline HDPE under focused ultrasound with the same acoustic power. By using the MD simulation, it is found that the frequency-dependent viscoelasticity is the most influential factor. We believe that this study can establish a rigorous link between molecular constitute and macroscopic themomechanical properties in HIFU field.

6. A shape memory polymer composite with enhanced shape recovery ability and also a two-way shape memory polymer are synthesized. A smart gripper and a self-rolling structure are designed. Our results prove that SMP materials are good candidates in soft robotics field.

List of Publications

Journal Papers

1. Yao Zhao*, **Kaiyuan Peng***, Jiaxin Xi, Shima Shahab, Reza Mirzaeifar. "A crosslinked poly(ethylene-co-vinyl acetate) based two-way shape memory polymer with improved shape memory property for soft actuator applications." **Submitted**. (*equal contribution)

2. **Kaiyuan Peng**, Yao Zhao, Shima Shahab, Reza Mirzaeifar. "A ductile shape memory polymer composite with enhanced shape recovery ability." *ACS Applied Materials & Interfaces*. **accepted**.

3. **Kaiyuan Peng**, Shima Shahab and Reza Mirzaeifar. "Polymers in High-Intensity Focused Ultrasound Fields." *Nanotechnology*. 2020, 32, 045707.

4. **Kaiyuan Peng**, and Reza Mirzaeifar. "Interplay of Chain Orientation and Bond Length in Size Dependency of Mechanical Properties in Polystyrene Nanofibers." *ACS Applied Polymer Materials*. 2020, 2, 4, 1664-1671.

5. **Kaiyuan Peng**, Amrinder Nain, and Reza Mirzaeifar. "Tracking the origins of size dependency in the mechanical properties of polymeric nanofibers at the atomistic scale." *Polymer*. 2019. 175(26): 118-128.

6. Aarushi Bhargava, **Kaiyuan Peng**, Jerry Stieg, Reza Mirzaeifar, and Shima Shahab. "Focused ultrasound actuation of shape memory polymers; acoustic-thermoelastic modeling and testing." *RSC advances*. 2017. 7: 45452-45469.

Conference Papers

1. **Kaiyuan Peng**, Shima Shahab and Reza Mirzaeifar, Polymers in high-intensity focused ultrasound fields. Acoustic society of America (ASA) annual meeting (2020), 7-11 December 2020.

2. Aarushi Bhargava, **Kaiyuan Peng** and Shima Shahab, Dynamics of focused ultrasound actuated shape memory polymers, Proceedings of the 26th SPIE Annual International Symposium on Smart Structures and Materials and Nondestructive Evaluation and Health Monitoring, Denver, CO, 3-7 March 2019 (**Best Student Paper Award – honorable mention**).

3. Aarushi Bhargava, **Kaiyuan Peng**, Reza Mirzaeifar, and Shima Shahab, Ultrasound actuated shape-memory polymer based drug delivery containers, Proceedings of the 25th SPIE Annual International Symposium on Smart Structures and Materials Nondestructive Evaluation and Health Monitoring, Denver, CO, 4-8 March 2018.

4. Aarushi Bhargava, **Kaiyuan Peng**, Jerry Stieg, Reza Mirzaeifar, and Shima Shahab, Ultrasound Actuation of Shape Memory Polymer Filaments; Acoustic-Thermoelastic Modeling and Testing. Proceedings of the 10th ASME Conference on Smart Materials, Adaptive Structures and Intelligent Systems, Snowbird, UT, 18-20 September 2017 (**Best Student Paper Award – 1st place**).

Posters

1. **Kaiyuan Peng**, Aniket Jana, Amrinder Nain, and Reza Mirzaeifar, Molecular Dynamics Simulation of Polystyrene Nanofibers, Virginia Tech MII technical conference, Blacksburg, VA, 2-3 November 2019.

2. Aniket Jana, **Kaiyuan Peng**, Reza Mirzaeifar, Amrinder Nain, Integrating Parallel Springs with Cantilever Physics to Measure Mechanical Properties of Individual Nanofibers.

2019 MII Technical Conference, Blacksburg, VA, 2-3 November 2019.

Appendices

Appendix A

Supporting Information for Chapter 5

Appendix A here represents the supporting information for Chapter 5, "A ductile SMP composite with enhanced shape recovery ability". Samples made of PS, tD and tDPS, prepared by the methods described in Chapter 5 are running for DSC and DMA tests. Figures A.1 - A.3 show the DSC curves for PS, tD and tDPS samples. To reveal the switch temperature of the tD and tDPS samples, corresponding DMA curves are shown in Figures A.4 - A.5.

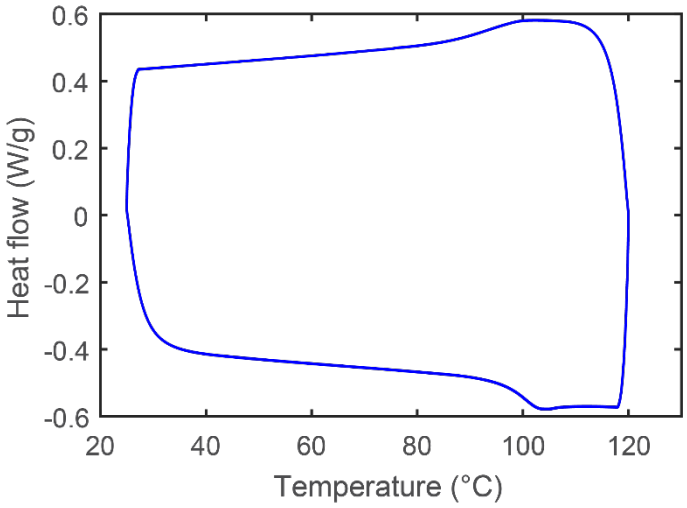

Figure A.1: The DSC curves of the PS samples.

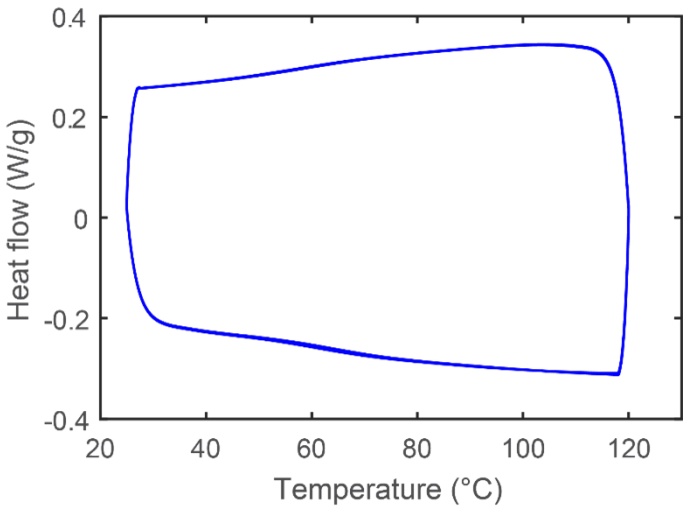

Figure A.2: The DSC curves of the tD samples.

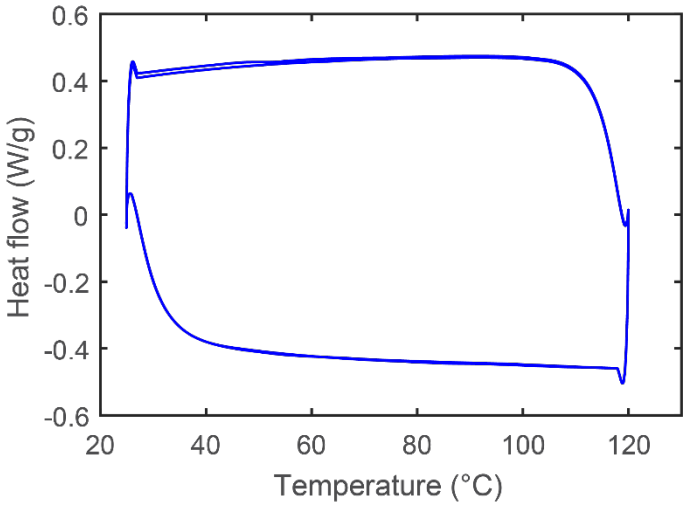

Figure A.3: The DSC curves of the tDPS samples.

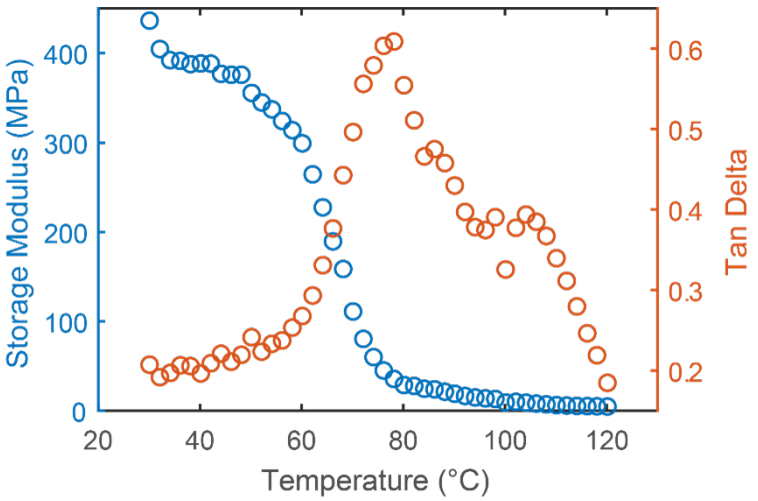

Figure A.4: Storage modulus and tan delta obtained from DMA tests for tD sample.

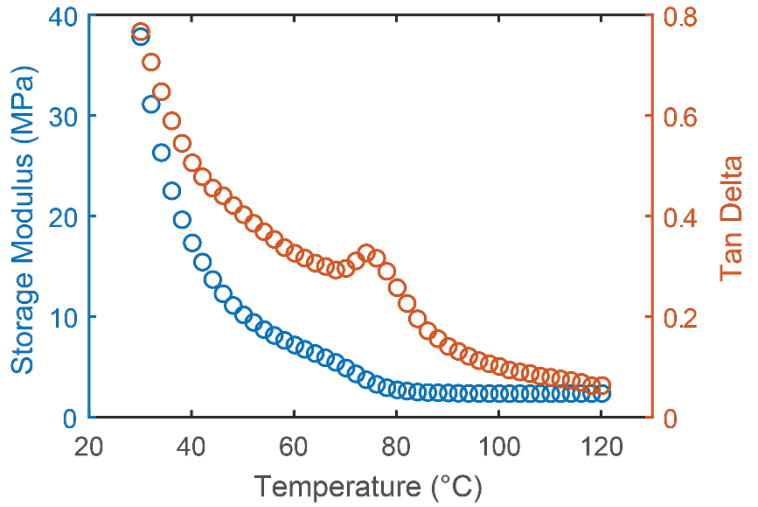

Figure A.5: Storage modulus and tan delta obtained from DMA tests for tDPS sample.

Appendix B

Supporting Information for Chapter 6

Appendix B here represents the supporting information for Chapter 6, "A two-way shape memory polymer for soft actuator applications". Figure B.1 illustrates the cPEVA sample preparation method. Figures B.2 - B.3 show the XRD and DSC results for the cPEVA samples with different concentrations. The recoverability of the cPEVA sample is described in Figure B.4. Figure B.5 focuses on the FEA model of the self-rolling structure.

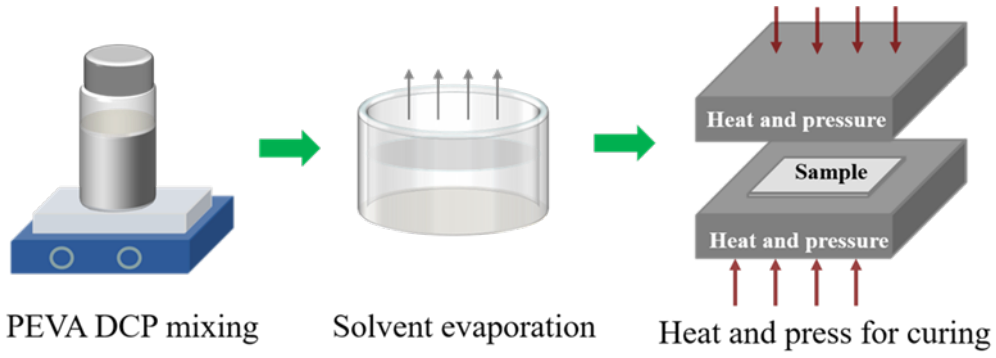

Figure B.1: The schematic of the cPEVA preparation.

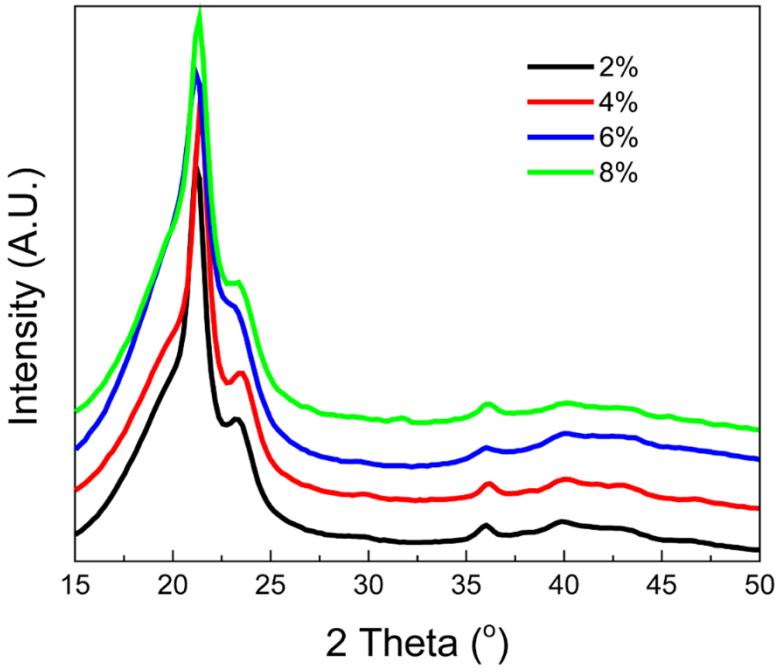

Figure B.2: The XRD profiles of the cPEVA samples with different DCP concentrations.

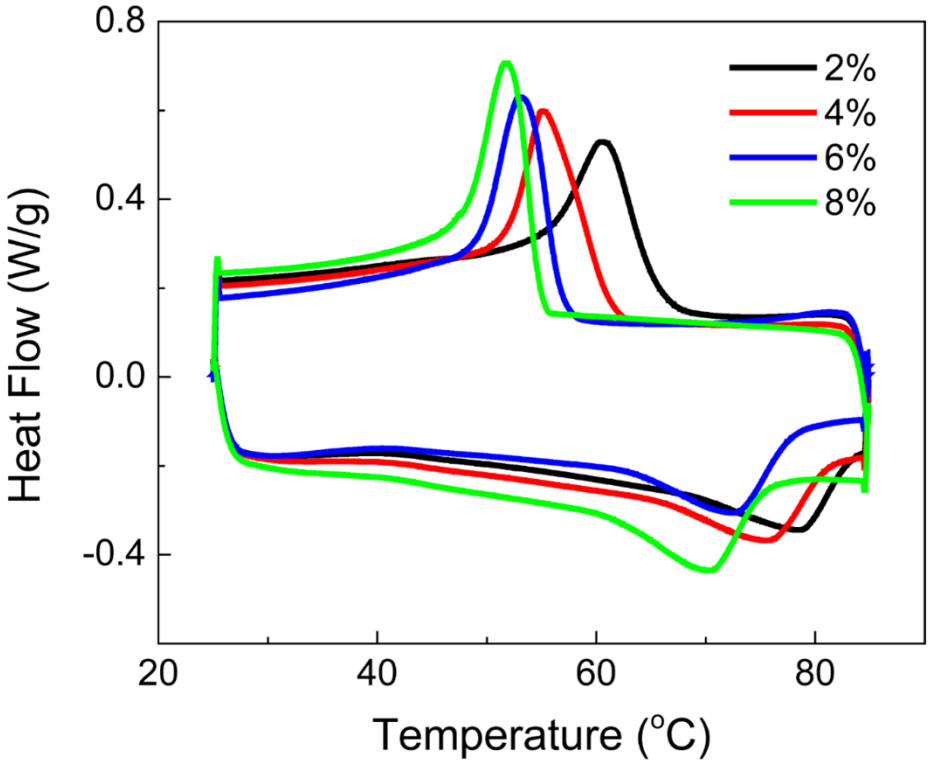

Figure B.3: The DSC curves of the cPEVA samples with different DCP concentrations.

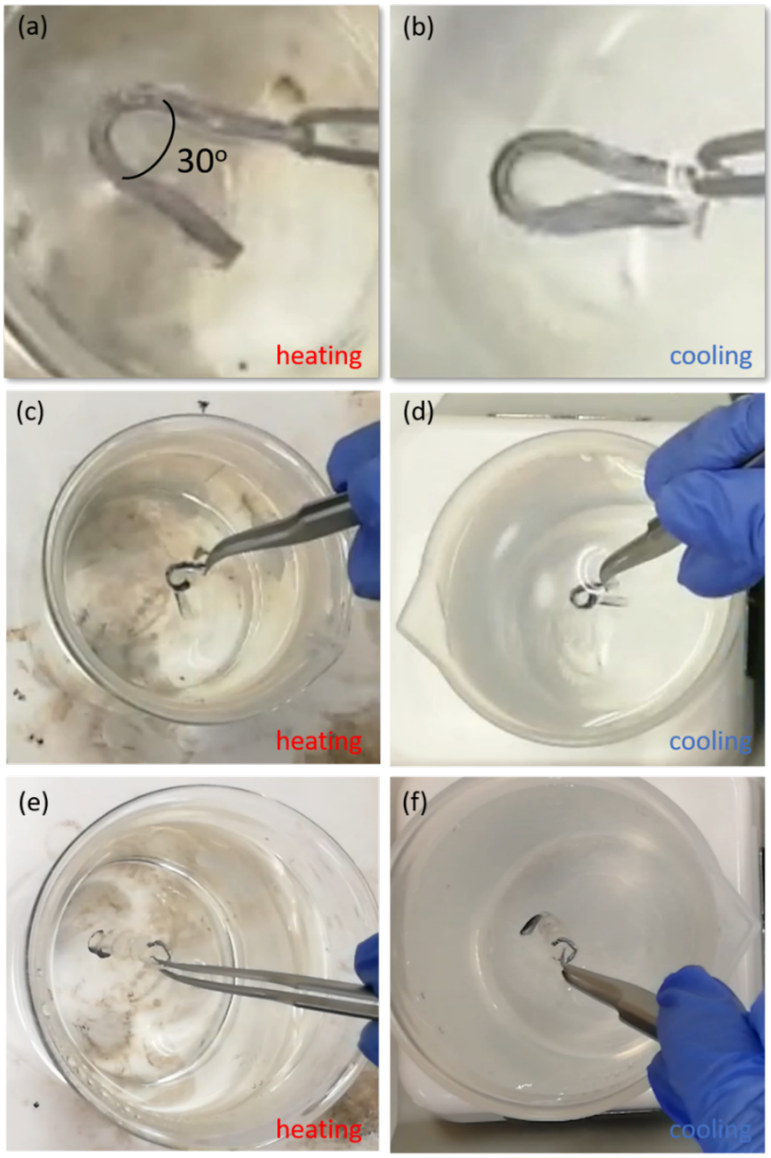

Figure B.4: The recoverability of the 6% DCP sample can be as large as 30o for bended shape (a, b). The spiral shape can recover about 90o (c, d). The end of the screw shape can spin for larger than 1 revolution (e, f).

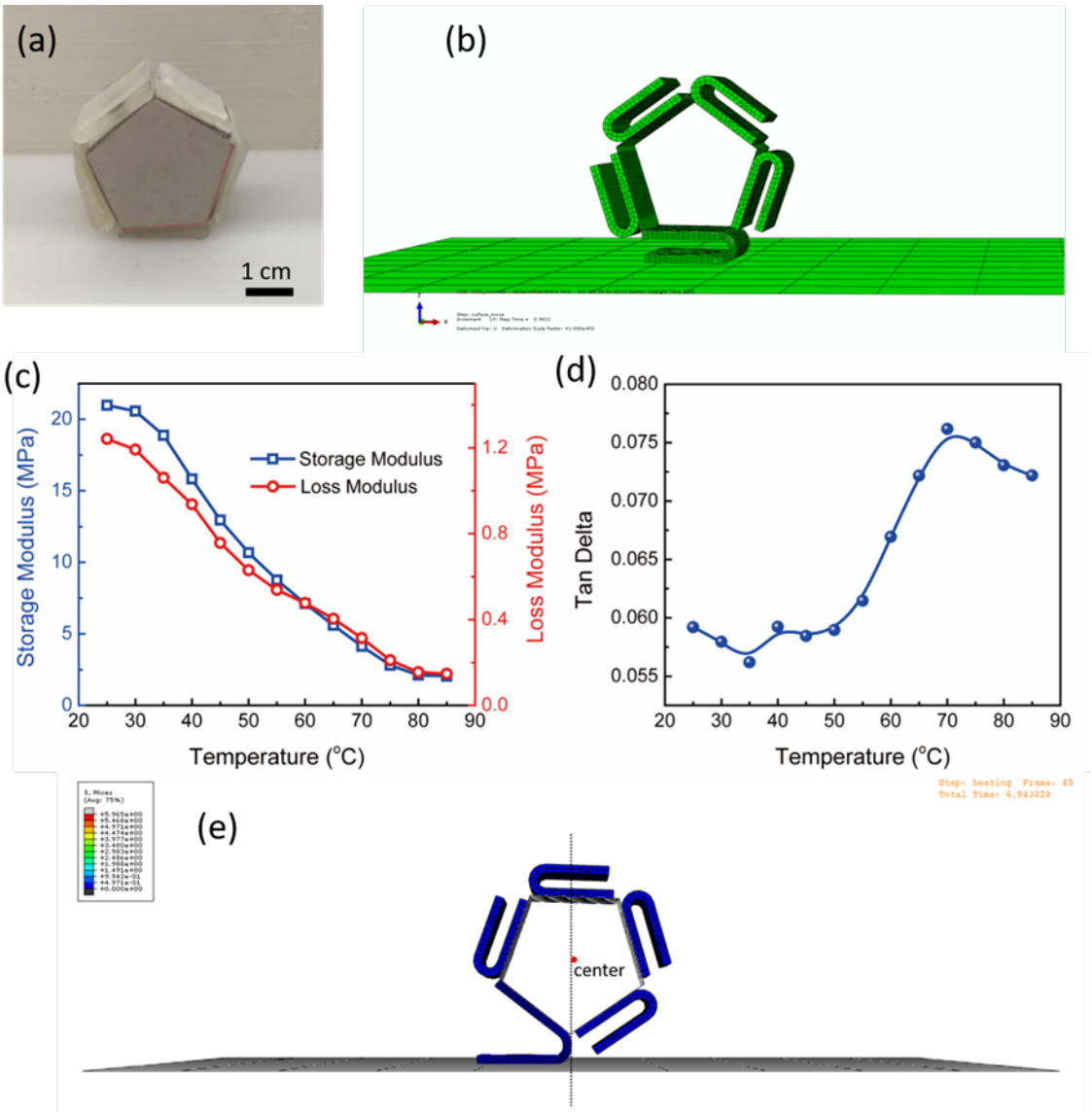

Figure B.5: The digital image (a) and simulation model (b) of the pentagon sample. The sweeping of the storage modulus (blue) and loss modulus (red) of the 6% DCP sample (c), and the Tan Delta (d) with temperatures. (e) The sample center surpasses the reference line (dashed) and the pentagon shape becomes unbalanced.

Bibliography

[1] CT Lim, EPS Tan, and SY Ng. Effects of crystalline morphology on the tensile properties of electrospun polymer nanofibers. *Applied Physics Letters*, 92(14):141908, 2008.

[2] Amrinder S Nain, Metin Sitti, Annette Jacobson, Tomasz Kowalewski, and Cristina Amon. Dry spinning based spinneret based tunable engineered parameters (step) technique for controlled and aligned deposition of polymeric nanofibers. *Macromolecular rapid communications*, 30(16):1406–1412, 2009.

[3] EPS Tan, SY Ng, and CT Lim. Tensile testing of a single ultrafine polymeric fiber. *Biomaterials*, 26(13):1453–1456, 2005.

[4] Amrinder S Nain, Joanna C Wong, Cristina Amon, and Metin Sitti. Drawing suspended polymer micro-/nanofibers using glass micropipettes. *Applied Physics Letters*, 89(18):183105, 2006.

[5] Elmer DF Ker, Amrinder S Nain, Lee E Weiss, Ji Wang, Joseph Suhan, Cristina H Amon, and Phil G Campbell. Bioprinting of growth factors onto aligned sub-micron fibrous scaffolds for simultaneous control of cell differentiation and alignment. *Biomaterials*, 32(32):8097–8107, 2011.

[6] Olga Grinberg, Shengwei Deng, Eyal Zussman, Tsachi Livneh, and Alla Zak. Raman scattering from single ws 2 nanotubes in stretched pvdf electrospun fibers. *Physical Chemistry Chemical Physics*, 19(28):18443–18451, 2017.

[7] Aarushi Bhargava, Kaiyuan Peng, Jerry Stieg, Reza Mirzaeifar, and Shima Shahab.

Focused ultrasound actuation of shape memory polymers; acoustic-thermoelastic modeling and testing. *RSC advances*, 7(72):45452–45469, 2017.

[8] Sezen Buell, Gregory C Rutledge, and Krystyn J Van Vliet. Predicting polymer nanofiber interactions via molecular simulations. *ACS applied materials & interfaces*, 2(4):1164–1172, 2010.

[9] Sezen Buell, Krystyn J Van Vliet, and Gregory C Rutledge. Mechanical properties of glassy polyethylene nanofibers via molecular dynamics simulations. *Macromolecules*, 42(13):4887–4895, 2009.

[10] Arkadii Arinstein and Eyal Zussman. Electrospun polymer nanofibers: mechanical and thermodynamic perspectives. *Journal of Polymer Science Part B: Polymer Physics*, 49(10):691–707, 2011.

[11] Fei Hang, Dun Lu, Russell J Bailey, Ines Jimenez-Palomar, Urszula Stachewicz, Beatriz Cortes-Ballesteros, Martin Davies, Martin Zech, Christoph Bödefeld, and Asa H Barber. In situ tensile testing of nanofibers by combining atomic force microscopy and scanning electron microscopy. *Nanotechnology*, 22(36):365708, 2011.

[12] Shing-Chung Wong, Avinash Baji, and Siwei Leng. Effect of fiber diameter on tensile properties of electrospun poly (-caprolactone). *Polymer*, 49(21):4713–4722, 2008.

[13] Xiang-Fa Wu and Yuris A Dzenis. Size effect in polymer nanofibers under tension. *Journal of Applied Physics*, 102(4):044306, 2007.

[14] Sneha Chawla, Jizhe Cai, and Mohammad Naraghi. Mechanical tests on individual carbon nanofibers reveals the strong effect of graphitic alignment achieved via precursor hot-drawing. *Carbon*, 117:208–219, 2017.

[15] M Naraghi, SN Arshad, and Ioannis Chasiotis. Molecular orientation and mechanical property size effects in electrospun polyacrylonitrile nanofibers. *Polymer*, 52(7):1612–1618, 2011.

[16] Andrea Camposeo, Israel Greenfeld, Francesco Tantussi, Stefano Pagliara, Maria Moffa, Francesco Fuso, Maria Allegrini, Eyal Zussman, and Dario Pisignano. Local mechanical properties of electrospun fibers correlate to their internal nanostructure. *Nano letters*, 13(11):5056–5062, 2013.

[17] Urszula Stachewicz, Russell J Bailey, Wei Wang, and Asa H Barber. Size dependent mechanical properties of electrospun polymer fibers from a composite structure. *Polymer*, 53(22):5132–5137, 2012.

[18] Shan Tang, Ying Li, Wing Kam Liu, and Xiao Xu Huang. Surface ripples of polymeric nanofibers under tension: The crucial role of poisson's ratio. *Macromolecules*, 47(18): 6503–6514, 2014.

[19] Jizhe Cai, Sneha Chawla, and Mohammad Naraghi. Microstructural evolution and mechanics of hot-drawn cnt-reinforced polymeric nanofibers. *Carbon*, 109:813–822, 2016.

[20] Sezen Curgul, Krystyn J Van Vliet, and Gregory C Rutledge. Molecular dynamics simulation of size-dependent structural and thermal properties of polymer nanofibers. *Macromolecules*, 40(23):8483–8489, 2007.

[21] Arkadii Arinstein. Supermolecular structure formation during electrospinning, and its effect on electrospun polymer nanofiber unique features. In *Problems of Nonlinear Mechanics and Physics of Materials*, pages 173–204. Springer, 2019.

[22] Arkadii Arinstein, Michael Burman, Oleg Gendelman, and Eyal Zussman. Effect of

supramolecular structure on polymer nanofibre elasticity. *Nature nanotechnology*, 2 (1):59, 2007.

[23] Shengwei Deng, Arkadii Arinstein, and Eyal Zussman. Size-dependent mechanical properties of glassy polymer nanofibers via molecular dynamics simulations. *Journal of Polymer Science Part B: Polymer Physics*, 55(6):506–514, 2017.

[24] Jian Yao, Cees WM Bastiaansen, and Ton Peijs. High strength and high modulus electrospun nanofibers. *Fibers*, 2(2):158–186, 2014.

[25] Jian Ma, Qian Zhang, Yin Zhang, Lei Zhou, Juekuan Yang, and Zhonghua Ni. A rapid and simple method to draw polyethylene nanofibers with enhanced thermal conductivity. *Applied Physics Letters*, 109(3):033101, 2016.

[26] JCL Hageman, Robert J Meier, M Heinemann, and RA De Groot. Young modulus of crystalline polyethylene from ab initio molecular dynamics. *Macromolecules*, 30(19): 5953–5957, 1997.

[27] Wolfgang Paul, Do Y Yoon, and Grant D Smith. An optimized united atom model for simulations of polymethylene melts. *The Journal of chemical physics*, 103(4):1702–1709, 1995.

[28] N Waheed, MS Lavine, and GC Rutledge. Molecular simulation of crystal growth in n-eicosane. *The Journal of chemical physics*, 116(5):2301–2309, 2002.

[29] Jacob D Davidson. *Multiscale modeling and simulation of crosslinked polymers*. PhD thesis, 2014.

[30] D Hossain, Mark A Tschopp, DK Ward, Jean-Luc Bouvard, P Wang, and Mark F Horstemeyer. Molecular dynamics simulations of deformation mechanisms of amorphous polyethylene. *Polymer*, 51(25):6071–6083, 2010.

[31] Marc S Lavine, Numan Waheed, and Gregory C Rutledge. Molecular dynamics simulation of orientation and crystallization of polyethylene during uniaxial extension. *Polymer*, 44(5):1771–1779, 2003.

[32] Xin Dong, David L McDowell, Surya R Kalidindi, and Karl I Jacob. Dependence of mechanical properties on crystal orientation of semi-crystalline polyethylene structures. *Polymer*, 55(16):4248–4257, 2014.

[33] Shengwei Deng. Tensile deformation of semi-crystalline polymers by molecular dynamics simulation. *Iranian Polymer Journal*, 26(12):903–911, 2017.

[34] Pavan V Kolluru and Ioannis Chasiotis. A master curve for the size and strain rate dependent large deformation behavior of ps nanofibers at room temperature. *Polymer*, 99:544–551, 2016.

[35] Chia-Ling Pai, Mary C Boyce, and Gregory C Rutledge. Mechanical properties of individual electrospun pa 6 (3) t fibers and their variation with fiber diameter. *Polymer*, 52(10):2295–2301, 2011.

[36] R Schellekens and CWMJ Bastiaansen. The drawing behavior of polyvinylalcohol fibers. *Journal of applied polymer science*, 43(12):2311–2315, 1991.

[37] Dimitry Papkov, Yan Zou, Mohammad Nahid Andalib, Alexander Goponenko, Stephen ZD Cheng, and Yuris A Dzenis. Simultaneously strong and tough ultrafine continuous nanofibers. *ACS nano*, 7(4):3324–3331, 2013.

[38] Zhuolei Zhang, Yao Zhao, Haoqi Li, Simona Percec, Jie Yin, and Fei Ren. Nanoparticle-infused uhmwpe layer as multifunctional coating for high-performance ppta single fibers. *Scientific reports*, 9(1):1–9, 2019. ISSN 2045-2322.

[39] Alessandro Polini, Stefano Pagliara, Ripalta Stabile, Giuseppe Stefano Netti, Leonarda Roca, Clelia Prattichizzo, Loreto Gesualdo, Roberto Cingolani, and Dario Pisignano. Collagen-functionalised electrospun polymer fibers for bioengineering applications. *Soft Matter*, 6(8):1668–1674, 2010.

[40] Jay Hoon Park and Gregory C Rutledge. 50th anniversary perspective: Advanced polymer fibers: High performance and ultrafine. *Macromolecules*, 50(15):5627–5642, 2017. ISSN 0024-9297.

[41] Myungshim Kang, Honggang Cui, and Sharon M Loverde. Coarse-grained molecular dynamics studies of the structure and stability of peptide-based drug amphiphile filaments. *Soft matter*, 13(42):7721–7730, 2017.

[42] Yantao Chen, Shan Xue, Qing Xia, Hongkun Li, Qiuming Liu, Bing Shi Li, and Ben Zhong Tang. Surface effect on the self-assembly of nanofibers revealed by in situ afm imaging and molecular simulation. *The Journal of Physical Chemistry C*, 123 (14):9292–9297, 2019. ISSN 1932-7447.

[43] Marie Richard-Lacroix and Christian Pellerin. Orientation and partial disentanglement in individual electrospun fibers: diameter dependence and correlation with mechanical properties. *Macromolecules*, 48(13):4511–4519, 2015. ISSN 0024-9297.

[44] Kaiyuan Peng, Amrinder Nain, and Reza Mirzaeifar. Tracking the origins of size dependency in the mechanical properties of polymeric nanofibers at the atomistic scale. *Polymer*, 175:118–128, 2019. ISSN 0032-3861.

[45] Saeed D Mohan, Geoffrey R Mitchell, and Fred J Davis. Chain extension in electrospun polystyrene fibres: a sans study. *Soft Matter*, 7(9):4397–4404, 2011.

[46] Arkadii Arinstein, Michael Burman, Oleg Gendelman, and Eyal Zussman. Effect of

supramolecular structure on polymer nanofibre elasticity. *Nature nanotechnology*, 2 (1):59, 2007. ISSN 1748-3395.

[47] Dimitry Papkov, Yan Zou, Mohammad Nahid Andalib, Alexander Goponenko, Stephen ZD Cheng, and Yuris A Dzenis. Simultaneously strong and tough ultrafine continuous nanofibers. *ACS nano*, 7(4):3324–3331, 2013. ISSN 1936-0851.

[48] Urszula Stachewicz, Russell J Bailey, Wei Wang, and Asa H Barber. Size dependent mechanical properties of electrospun polymer fibers from a composite structure. *Polymer*, 53(22):5132–5137, 2012. ISSN 0032-3861.

[49] Andrea Camposeo, Israel Greenfeld, Francesco Tantussi, Stefano Pagliara, Maria Moffa, Francesco Fuso, Maria Allegrini, Eyal Zussman, and Dario Pisignano. Local mechanical properties of electrospun fibers correlate to their internal nanostructure. *Nano letters*, 13(11):5056–5062, 2013. ISSN 1530-6984.

[50] Visit Vao-soongnern, Pemra Doruker, and Wayne L Mattice. Simulation of an amorphous polyethylene nanofiber on a high coordination lattice. *Macromolecular theory and simulations*, 9(1):1–13, 2000. ISSN 1022-1344.

[51] Visit Vao-soongnern. Molecular simulation of nanoparticles composed of mono-and bi-dispersed poly (ethylene oxide). *Journal of molecular modeling*, 25(9):271, 2019. ISSN 1610-2940.

[52] Jizhe Cai, Sneha Chawla, and Mohammad Naraghi. Microstructural evolution and mechanics of hot-drawn cnt-reinforced polymeric nanofibers. *Carbon*, 109:813–822, 2016. ISSN 0008-6223.

[53] Dimitry Papkov, Nicolas Delpouve, Laurent Delbreilh, Steven Araujo, Taylor Stockdale, Sergey Mamedov, Kaspars Maleckis, Yan Zou, Mohammad Nahid Andalib, and

Eric Dargent. Quantifying polymer chain orientation in strong and tough nanofibers with low crystallinity: toward next generation nanostructured superfibers. *ACS nano*, 13(5):4893–4927, 2019. ISSN 1936-0851.

[54] Amrinder S Nain, Joanna C Wong, Cristina Amon, and Metin Sitti. Drawing suspended polymer micro-/nanofibers using glass micropipettes. *Applied Physics Letters*, 89(18):183105, 2006. ISSN 0003-6951.

[55] Shengwei Deng, Arkadii Arinstein, and Eyal Zussman. Size-dependent mechanical properties of glassy polymer nanofibers via molecular dynamics simulations. *Journal of Polymer Science Part B: Polymer Physics*, 55(6):506–514, 2017. ISSN 0887-6266.

[56] Shengwei Deng, Arkadii Arinstein, and Eyal Zussman. Size-dependent mechanical properties of glassy polymer nanofibers via molecular dynamics simulations. *Journal of Polymer Science Part B: Polymer Physics*, 55(6):506–514, 2017. ISSN 0887-6266.

[57] Sezen Curgul, Krystyn J Van Vliet, and Gregory C Rutledge. Molecular dynamics simulation of size-dependent structural and thermal properties of polymer nanofibers. *Macromolecules*, 40(23):8483–8489, 2007. ISSN 0024-9297.

[58] David D Hsu, Wenjie Xia, Steven G Arturo, and Sinan Keten. Thermomechanically consistent and temperature transferable coarse-graining of atactic polystyrene. *Macromolecules*, 48(9):3057–3068, 2015. ISSN 0024-9297.

[59] Steve Plimpton, Paul Crozier, and Aidan Thompson. Lammps-large-scale atomic/-molecular massively parallel simulator. *Sandia National Laboratories*, 18:43, 2007.

[60] Pavan V Kolluru and Ioannis Chasiotis. Interplay of molecular and specimen length scales in the large deformation mechanical behavior of polystyrene nanofibers. *Polymer*, 56:507–515, 2015. ISSN 0032-3861.

[61] Pavan V Kolluru and Ioannis Chasiotis. A master curve for the size and strain rate dependent large deformation behavior of ps nanofibers at room temperature. *Polymer*, 99:544–551, 2016. ISSN 0032-3861.

[62] LJ Fetters, DJ Lohse, D Richter, TA Witten, and A Zirkel. Connection between polymer molecular weight, density, chain dimensions, and melt viscoelastic properties. *Macromolecules*, 27(17):4639–4647, 1994. ISSN 0024-9297.

[63] LJ Fetters, DJ Lohse, and RH Colby. *Chain dimensions and entanglement spacings*, pages 447–454. Springer, 2007.

[64] Vagelis A Harmandaris, Vlasis G Mavrantzas, and Doros N Theodorou. Atomistic molecular dynamics simulation of polydisperse linear polyethylene melts. *Macromolecules*, 31(22):7934–7943, 1998. ISSN 0024-9297.

[65] Yiyang Xu, Yanhong Gao, Xiaofeng Wang, Jing Jiang, Jianhua Hou, and Qian Li. Internal structure of amorphous electrospun nanofiber: Oriented molecular chains. *Macromolecular Materials and Engineering*, 302(7):1700054, 2017. ISSN 1438-7492.

[66] Rainer H MuÈller, Karsten MaÈder, and Sven Gohla. Solid lipid nanoparticles (sln) for controlled drug delivery–a review of the state of the art. *European journal of pharmaceutics and biopharmaceutics*, 50(1):161–177, 2000. ISSN 0939-6411.

[67] Kathryn E Uhrich, Scott M Cannizzaro, Robert S Langer, and Kevin M Shakesheff. Polymeric systems for controlled drug release. *Chemical reviews*, 99(11):3181–3198, 1999. ISSN 0009-2665.

[68] SA Martel-Estrada, I Olivas-Armendáriz, CA Martínez-Pérez, T Hernández, EI Acosta-Gómez, JG Chacón-Nava, F Jiménez-Vega, and PE García-Casillas. Chi-

tosan/poly (dl, lactide-co-glycolide) scaffolds for tissue engineering. *Journal of Materials Science: Materials in Medicine*, 23(12):2893–2901, 2012. ISSN 0957-4530.

[69] Tao Xie. Recent advances in polymer shape memory. *Polymer*, 52(22):4985–5000, 2011. ISSN 0032-3861. doi: http://dx.doi.org/10.1016/j.polymer.2011.08.003. URL http://www.sciencedirect.com/science/article/pii/S0032386111006513.

[70] Robert Bogue. Smart materials: a review of recent developments. *Assembly Automation*, 32(1):3–7, 2012. ISSN 0144-5154.

[71] Inderjit Chopra. Review of state of art of smart structures and integrated systems. *AIAA journal*, 40(11):2145–2187, 2002. ISSN 0001-1452.

[72] Mukesh V Gandhi and Brian S Thompson. *Smart materials and structures*. Springer Science Business Media, 1992. ISBN 0412370107.

[73] Victor Giurgiutiu. Review of smart-materials actuation solutions for aeroelastic and vibration control. *Journal of Intelligent Material Systems and Structures*, 11(7):525–544, 2000. ISSN 1045-389X.

[74] Andreas Lendlein and Steffen Kelch. Shape-memory polymers. *Angewandte Chemie International Edition*, 41(12):2034–2057, 2002. ISSN 1521-3773.

[75] Yoshifumi Amamoto, Hideyuki Otsuka, Atsushi Takahara, and Krzysztof Matyjaszewski. Self-healing of covalently cross-linked polymers by reshuffling thiuram disulfide moieties in air under visible light. *Advanced Materials*, 24(29):3975–3980, 2012. ISSN 1521-4095.

[76] Xiangxu Chen, Matheus A Dam, Kanji Ono, Ajit Mal, Hongbin Shen, Steven R Nutt, Kevin Sheran, and Fred Wudl. A thermally re-mendable cross-linked polymeric material. *Science*, 295(5560):1698–1702, 2002. ISSN 0036-8075.

[77] Xiangxu Chen, Fred Wudl, Ajit K Mal, Hongbin Shen, and Steven R Nutt. New thermally remendable highly cross-linked polymeric materials. *Macromolecules*, 36(6): 1802–1807, 2003. ISSN 0024-9297.

[78] Biswajit Ghosh and Marek W Urban. Self-repairing oxetane-substituted chitosan polyurethane networks. *Science*, 323(5920):1458–1460, 2009. ISSN 0036-8075.

[79] Chan e Yuan, Min Zhi Rong, Ming Qiu Zhang, Ze Ping Zhang, and Yan Chao Yuan. Self-healing of polymers via synchronous covalent bond fission/radical recombination. *Chemistry of Materials*, 23(22):5076–5081, 2011. ISSN 0897-4756.

[80] Reza Mirzaeifar. *A multiscale study of NiTi shape memory alloys*. Thesis, 2013.

[81] Reza Mirzaeifar, Reginald DesRoches, and Arash Yavari. Analysis of the rate-dependent coupled thermo-mechanical response of shape memory alloy bars and wires in tension. *Continuum Mechanics and Thermodynamics*, 23(4):363–385, 2011. ISSN 0935-1175.

[82] Reza Mirzaeifar, Reginald DesRoches, Arash Yavari, and Ken Gall. On superelastic bending of shape memory alloy beams. *International Journal of Solids and Structures*, 50(10):1664–1680, 2013. ISSN 0020-7683.

[83] K Uchino. Shape memory ceramics. *Shape Memory Materials*, pages 184–202, 1998.

[84] C Liu, H Qin, and PT Mather. Review of progress in shape-memory polymers. *Journal of Materials Chemistry*, 17(16):1543–1558, 2007.

[85] Harper Meng and Guoqiang Li. A review of stimuli-responsive shape memory polymer composites. *Polymer*, 54(9):2199–2221, 2013. ISSN 0032-3861.

[86] Debdatta Ratna and J Karger-Kocsis. Recent advances in shape memory polymers and composites: a review. *Journal of Materials Science*, 43(1):254–269, 2008. ISSN 0022-2461.

[87] Subbu S Venkatraman, Lay Poh Tan, Joe Ferry D Joso, Yin Chiang Freddy Boey, and Xintong Wang. Biodegradable stents with elastic memory. *Biomaterials*, 27(8): 1573–1578, 2006. ISSN 0142-9612.

[88] Christopher Michael Yakacki, Robin Shandas, Craig Lanning, Bryan Rech, Alex Eckstein, and Ken Gall. Unconstrained recovery characterization of shape-memory polymer networks for cardiovascular applications. *Biomaterials*, 28(14):2255–2263, 2007. ISSN 0142-9612.

[89] Liang Xue, Shiyao Dai, and Zhi Li. Biodegradable shape-memory block co-polymers for fast self-expandable stents. *Biomaterials*, 31(32):8132–8140, 2010. ISSN 0142-9612.

[90] Brent Louis Volk. *Three-dimensional modeling of shape memory polymers considering finite deformations and heat transfer*. Thesis, 2012.

[91] Christian Wischke and Andreas Lendlein. Shape-memory polymers as drug carriers—a multifunctional system. *Pharmaceutical research*, 27(4):527–529, 2010. ISSN 0724-8741.

[92] Joseph Kost and Robert Langer. Responsive polymeric delivery systems. *Advanced drug delivery reviews*, 64:327–341, 2012. ISSN 0169-409X.

[93] Kolin C Hribar, Robert B Metter, Jamie L Ifkovits, Thomas Troxler, and Jason A Burdick. Light-induced temperature transitions in biodegradable polymer and nanorod composites. *Small*, 5(16):1830–1834, 2009. ISSN 1613-6829.

[94] Justin R Kumpfer and Stuart J Rowan. Thermo-, photo-, and chemo-responsive shape-memory properties from photo-cross-linked metallo-supramolecular polymers. *Journal of the American Chemical Society*, 133(32):12866–12874, 2011. ISSN 0002-7863.

[95] Andreas Lendlein, Hongyan Jiang, Oliver Jünger, and Robert Langer. Light-induced shape-memory polymers. *Nature*, 434(7035):879–882, 2005. ISSN 0028-0836.

[96] U Narendra Kumar, K Kratz, W Wagermaier, M Behl, and A Lendlein. Non-contact actuation of triple-shape effect in multiphase polymer network nanocomposites in alternating magnetic field. *Journal of Materials Chemistry*, 20(17):3404–3415, 2010.

[97] Uttamchand Narendra Kumar, Karl Kratz, Matthias Heuchel, Marc Behl, and Andreas Lendlein. Shape-memory nanocomposites with magnetically adjustable apparent switching temperatures. *Advanced Materials*, 23(36):4157–4162, 2011. ISSN 1521-4095.

[98] Yanju Liu, Haibao Lv, Xin Lan, Jinsong Leng, and Shanyi Du. Review of electro-active shape-memory polymer composite. *Composites Science and Technology*, 69(13): 2064–2068, 2009. ISSN 0266-3538.

[99] Kai Yu, Zhichun Zhang, Yanju Liu, and Jinsong Leng. Carbon nanotube chains in a shape memory polymer/carbon black composite: to significantly reduce the electrical resistivity. *Applied Physics Letters*, 98(7):074102, 2011. ISSN 0003-6951.

[100] JE Kennedy, GR Ter Haar, and D Cranston. High intensity focused ultrasound: surgery of the future? *The British journal of radiology*, 2014.

[101] > Gail ter Haar and Constantin Coussios. High intensity focused ultrasound: physical principles and devices. *International Journal of Hyperthermia*, 23(2):89–104, 2007. ISSN 0265-6736.

[102] Marjan Bakhtiari Nejad, Ahmed Elnahhas, Sunghwan Jung, and Shima Shahab. Ultrasound acoustic energy for microbubble manipulation. In *SPIE Smart Structures and Materials+ Nondestructive Evaluation and Health Monitoring*, pages 101642H–101642H–14. International Society for Optics and Photonics.

[103] S Shahab and A Erturk. Contactless ultrasonic energy transfer for wireless systems: acoustic-piezoelectric structure interaction modeling and performance enhancement. *Smart Materials and Structures*, 23(12):125032, 2014. ISSN 0964-1726.

[104] S Shahab, M Gray, and A Erturk. Ultrasonic power transfer from a spherical acoustic wave source to a free-free piezoelectric receiver: Modeling and experiment. *Journal of Applied Physics*, 117(10):104903, 2015. ISSN 0021-8979.

[105] Shima Shahab and Alper Erturk. Contactless ultrasonic energy transfer: Acoustic-piezoelectric structure interaction modeling and performance enhancement. In *ASME 2014 International Design Engineering Technical Conferences and Computers and Information in Engineering Conference*, pages V008T11A095–V008T11A095. American Society of Mechanical Engineers.

[106] H Bruinewoud. *Ultrasound-induced drug release from polymer matrices*. Thesis, 2005.

[107] Bruno G De Geest, Andre G Skirtach, Arif A Mamedov, Alexei A Antipov, Nicholas A Kotov, Stefaan C De Smedt, and Gleb B Sukhorukov. Ultrasound-triggered release from multilayered capsules. *Small*, 3(5):804–808, 2007. ISSN 1613-6829.

[108] J Kost, K Leong, and R Langer. Ultrasound-enhanced polymer degradation and release of incorporated substances. *Proceedings of the National Academy of Sciences*, 86(20): 7663–7666, 1989. ISSN 0027-8424.

[109] Dmitry G. Shchukin, Dmitry A. Gorin, and Helmuth Möhwald. Ultrasonically induced

opening of polyelectrolyte microcontainers. *Langmuir*, 22(17):7400–7404, 2006. ISSN 0743-7463. doi: 10.1021/la061047m. URL http://dx.doi.org/10.1021/la061047m.

[110] Andre G Skirtach, Bruno G De Geest, Arif Mamedov, Alexei A Antipov, Nicholas A Kotov, and Gleb B Sukhorukov. Ultrasound stimulated release and catalysis using polyelectrolyte multilayer capsules. *Journal of materials chemistry*, 17(11):1050–1054, 2007.

[111] Ghaleb A Husseini, Natalya Y Rapoport, Douglas A Christensen, John D Pruitt, and William G Pitt. Kinetics of ultrasonic release of doxorubicin from pluronic p105 micelles. *Colloids and Surfaces B: Biointerfaces*, 24(3):253–264, 2002. ISSN 0927-7765.

[112] Yongwen Li, Rui Tong, Hesheng Xia, Hongji Zhang, and Juan Xuan. High intensity focused ultrasound and redox dual responsive polymer micelles. *Chemical Communications*, 46(41):7739–7741, 2010.

[113] Alexander Marin, Md Muniruzzaman, and Natalya Rapoport. Mechanism of the ultrasonic activation of micellar drug delivery. *Journal of controlled release*, 75(1):69–81, 2001. ISSN 0168-3659.

[114] Jie Wang, Maxime Pelletier, Hongji Zhang, Hesheng Xia, and Yue Zhao. High-frequency ultrasound-responsive block copolymer micelle. *Langmuir*, 25(22):13201–13205, 2009. ISSN 0743-7463.

[115] Bo Liu, Hesheng Xia, Guoxia Fei, Guo Li, and Wenru Fan. High-intensity focused ultrasound-induced thermal effect for solid polymer materials. *Macromolecular Chemistry and Physics*, 214(22):2519–2527, 2013. ISSN 1521-3935.

[116] Jianjun Han, Guoxia Fei, Guo Li, and Hesheng Xia. High intensity focused ultrasound

triggered shape memory and drug release from biodegradable polyurethane. *Macromolecular Chemistry and Physics*, 214(11):1195–1203, 2013. ISSN 1521-3935.

[117] Timothy S Hart and Mark F Hamilton. Nonlinear effects in focused sound beams. *The Journal of the Acoustical Society of America*, 84(4):1488–1496, 1988. ISSN 0001-4966.

[118] Christopher Rowland Hill, Jeff C Bamber, and GR Ter Haar. Physical principles of medical ultrasonics. *The Journal of the Acoustical Society of America*, 116(5):2707–2707, 2004. ISSN 0001-4966.

[119] Walter Summer and Margaret K Patrick. *Ultrasonic therapy: A textbook for physiotherapists*. Elsevier, 1964.

[120] Gail Ter Haar. Therapeutic applications of ultrasound. *Progress in biophysics and molecular biology*, 93(1):111–129, 2007. ISSN 0079-6107.

[121] F. P. Curra, P. D. Mourad, V. A. Khokhlova, R. O. Cleveland, and L. A. Crum. Numerical simulations of heating patterns and tissue temperature response due to high-intensity focused ultrasound. *IEEE Transactions on Ultrasonics, Ferroelectrics, and Frequency Control*, 47(4):1077–1089, 2000. ISSN 0885-3010. doi: 10.1109/58.852092.

[122] G. Barot, I. J. Rao, and K. R. Rajagopal. A thermodynamic framework for the modeling of crystallizable shape memory polymers. *International Journal of Engineering Science*, 46(4):325–351, 2008. ISSN 0020-7225. doi: http://doi.org/10.1016/j.ijengsci.2007.11.008. URL http://www.sciencedirect.com/science/article/pii/S0020722507001309.

[123] L. Volk Brent, C. Lagoudas Dimitris, and Chen Yi-Chao. Analysis of the finite deformation response of shape memory polymers: Ii. 1d calibration and numerical implementation of a finite deformation, thermoelastic model. *Smart Materials and Structures*,

19(7):075006, 2010. ISSN 0964-1726. URL http://stacks.iop.org/0964-1726/19/i=7/a=075006.

[124] Mahesh Khanolkar, Jaskirat Sodhi, and I. Joga Rao. Modeling the behavior of crystallizable shape memory polymers subject to inhomogeneous deformations. (44151): 105–109, 2010. doi: 10.1115/SMASIS2010-3694. URL http://dx.doi.org/10.1115/SMASIS2010-3694.

[125] H. Jerry Qi, Thao D. Nguyen, Francisco Castro, Christopher M. Yakacki, and Robin Shandas. Finite deformation thermo-mechanical behavior of thermally induced shape memory polymers. *Journal of the Mechanics and Physics of Solids*, 56(5):1730–1751, 2008. ISSN 0022-5096. doi: http://doi.org/10.1016/j.jmps.2007.12.002. URL http://www.sciencedirect.com/science/article/pii/S002250960700230X.

[126] Kai Yu and H. Jerry Qi. Temperature memory effect in amorphous shape memory polymers. *Soft Matter*, 10(47):9423–9432, 2014. ISSN 1744-683X. doi: 10.1039/C4SM01816H. URL http://dx.doi.org/10.1039/C4SM01816H.

[127] Gautam Barot. *Constitutive Modeling of the Thermo-mechanics Associated with Crystallizable Shape Memory Polymers*. ProQuest, 2007. ISBN 0549873007.

[128] Guo Li, Guoxia Fei, Bo Liu, Hesheng Xia, and Yue Zhao. Shape recovery characteristics for shape memory polymers subjected to high intensity focused ultrasound. *RSC Advances*, 4(62):32701–32709, 2014.

[129] Carmen Alvarez-Lorenzo, Valerij Y Grinberg, Tatiana V Burova, and Angel Concheiro. Stimuli-sensitive crosslinked hydrogels as drug delivery systems: Impact of the drug on the responsiveness. *International Journal of Pharmaceutics*, page 119157, 2020. ISSN 0378-5173.

[130] Aarushi Bhargava, Kaiyuan Peng, Reza Mirzaeifar, and Shima Shahab. Ultrasound actuated shape-memory polymer based drug delivery containers. In *Active and Passive Smart Structures and Integrated Systems XII*, volume 10595, page 105952H. International Society for Optics and Photonics, .

[131] Aarushi Bhargava, Kaiyuan Peng, Jerry Stieg, Reza Mirzaeifar, and Shima Shahab. Focused ultrasound actuation of shape memory polymers; acoustic-thermoelastic modeling and testing. *RSC advances*, 7(72):45452–45469, 2017.

[132] Ronald A Siegel. Stimuli sensitive polymers and self regulated drug delivery systems: a very partial review. *Journal of controlled release*, 190:337–351, 2014. ISSN 0168-3659.

[133] Stefan Cichosz, Anna Masek, and Marian Zaborski. Polymer-based sensors: A review. *Polymer Testing*, 67:342–348, 2018. ISSN 0142-9418.

[134] Larisa V Sigolaeva, Dmitry V Pergushov, Marina Oelmann, Simona Schwarz, Monia Brugnoni, Ilya N Kurochkin, Felix A Plamper, Andreas Fery, and Walter Richtering. Surface functionalization by stimuli-sensitive microgels for effective enzyme uptake and rational design of biosensor setups. *Polymers*, 10(7):791, 2018.

[135] George Pasparakis and Maria Vamvakaki. Multiresponsive polymers: nano-sized assemblies, stimuli-sensitive gels and smart surfaces. *Polymer Chemistry*, 2(6):1234–1248, 2011.

[136] Clement Appiah, Christine Arndt, Katharina Siemsen, Anne Heitmann, Anne Staubitz, and Christine Selhuber-Unkel. Living materials herald a new era in soft robotics. *Advanced Materials*, 31(36):1807747, 2019. ISSN 0935-9648.

[137] Qiji Ze, Xiao Kuang, Shuai Wu, Janet Wong, S Macrae Montgomery, Rundong Zhang, Joshua M Kovitz, Fengyuan Yang, H Jerry Qi, and Ruike Zhao. Magnetic shape mem-

ory polymers with integrated multifunctional shape manipulation. *Advanced Materials*, 32(4):1906657, 2020. ISSN 0935-9648.

[138] Huanqing Cui, Qilong Zhao, Yunlong Wang, and Xuemin Du. Bioinspired actuators based on stimuli-responsive polymers. *Chemistry–An Asian Journal*, 14(14):2369–2387, 2019. ISSN 1861-4728.

[139] Taylor Ware, Dustin Simon, Keith Hearon, Clive Liu, Sagar Shah, Jonathan Reeder, Navid Khodaparast, Michael P Kilgard, Duncan J Maitland, and Robert L Rennaker. Three-dimensional flexible electronics enabled by shape memory polymer substrates for responsive neural interfaces. *Macromolecular materials and engineering*, 297(12): 1193–1202, 2012. ISSN 1438-7492.

[140] Andreas Lendlein and Robert Langer. Biodegradable, elastic shape-memory polymers for potential biomedical applications. *Science*, 296(5573):1673–1676, 2002. ISSN 0036-8075.

[141] Hao Ma and Zhiting Tian. Effects of polymer topology and morphology on thermal transport: A molecular dynamics study of bottlebrush polymers. *Applied Physics Letters*, 110(9):091903, 2017. ISSN 0003-6951.

[142] Christopher Michael Yakacki, Robin Shandas, Craig Lanning, Bryan Rech, Alex Eckstein, and Ken Gall. Unconstrained recovery characterization of shape-memory polymer networks for cardiovascular applications. *Biomaterials*, 28(14):2255–2263, 2007. ISSN 0142-9612.

[143] Yoshifumi Amamoto, Hideyuki Otsuka, Atsushi Takahara, and Krzysztof Matyjaszewski. Self-healing of covalently cross-linked polymers by reshuffling thiuram disulfide moieties in air under visible light. *Advanced Materials*, 24(29):3975–3980, 2012. ISSN 1521-4095.

[144] Yongkang Bai, Jiwen Zhang, and Xin Chen. A thermal-, water-, and near-infrared light-induced shape memory composite based on polyvinyl alcohol and polyaniline fibers. *ACS Applied Materials Interfaces*, 10(16):14017–14025, 2018. ISSN 1944-8244. doi: 10.1021/acsami.8b01425. URL https://doi.org/10.1021/acsami.8b01425.

[145] Liang Fang, Tianyu Fang, Zhenggang Fang, Chunhua Lu, and Zhongzi Xu. Solar light responsive polymer composites with three shape-memory effects. *Macromolecular Materials and Engineering*, 301(3):267–273, 2016. ISSN 1438-7492.

[146] Biswajit Ghosh and Marek W Urban. Self-repairing oxetane-substituted chitosan polyurethane networks. *Science*, 323(5920):1458–1460, 2009. ISSN 0036-8075.

[147] Kolin C Hribar, Robert B Metter, and Jason A Burdick. Novel nano-composite biomaterials that respond to light. In *Engineering in Medicine and Biology Society, 2009. EMBC 2009. Annual International Conference of the IEEE*, pages 2409–2411. IEEE. ISBN 1424432960.

[148] Duncan J Maitland, Melodie F Metzger, Daniel Schumann, Abraham Lee, and Thomas S Wilson. Photothermal properties of shape memory polymer micro-actuators for treating stroke. *Lasers in Surgery and Medicine: The Official Journal of the American Society for Laser Medicine and Surgery*, 30(1):1–11, 2002. ISSN 0196-8092.

[149] Harper Meng and Guoqiang Li. A review of stimuli-responsive shape memory polymer composites. *Polymer*, 54(9):2199–2221, 2013. ISSN 0032-3861.

[150] Ward Small IV, Thomas S Wilson, William J Benett, Jeffrey M Loge, and Duncan J Maitland. Laser-activated shape memory polymer intravascular thrombectomy device. *Optics Express*, 13(20):8204–8213, 2005. ISSN 1094-4087.

[151] Mohammad Reza Bozorgmehr, Ali Morsali, S Ali Beyramabadi, Farhad Khamchin

Moghaddam, Jamal Pashirepour, and Mitra Shakeri. All atom molecular dynamics simulation study of polyethylene polymer in supercritical water, supercritical ethanol and supercritical methanol. *The Journal of Supercritical Fluids*, 86:124–128, 2014. ISSN 0896-8446.

[152] Jinxing Li, Berta Esteban-Fernández de Ávila, Wei Gao, Liangfang Zhang, and Joseph Wang. Micro/nanorobots for biomedicine: Delivery, surgery, sensing, and detoxification. *Science Robotics*, 2(4), 2017.

[153] Marcus Antonius Jacobs. Measurement and modeling of thermodynamic properties for the processing of polymers in supercritical fluids. *Eindhoven University of Technology, Eindhoven*, 2005.

[154] Bo Liu, Hesheng Xia, Guoxia Fei, Guo Li, and Wenru Fan. High-intensity focused ultrasound-induced thermal effect for solid polymer materials. *Macromolecular Chemistry and Physics*, 214(22):2519–2527, 2013. ISSN 1022-1352.

[155] Hendrikje Bruinewoud. Ultrasound-induced drug release from polymer matrices: the glass transition temperature as a thermo-responsive switch. 2005.

[156] Hao Ma and Zhiting Tian. Effects of polymer chain confinement on thermal conductivity of ultrathin amorphous polystyrene films. *Applied Physics Letters*, 107(7):073111, 2015. ISSN 0003-6951.

[157] Rohit Pillai, Matthew K Borg, and Jason M Reese. Dynamics of nanodroplets on vibrating surfaces. *Langmuir*, 34(39):11898–11904, 2018. ISSN 0743-7463.

[158] KE Frøysa, J Naze Tjøtta, and J Berntsen. Finite amplitude effects in sound beams. pure tone and pulsed excitation. *Advances in nonlinear acoustics*, pages 233–238, 1993.

[159] FM Pestorius and DT Blackstock. Propagation of finite-amplitude noise. *Finite-Amplitude Wave Effects in Fluids*, pages 24–29, 1974.

[160] Ester Chiessi, Francesca Cavalieri, and Gaio Paradossi. Water and polymer dynamics in chemically cross-linked hydrogels of poly (vinyl alcohol): A molecular dynamics simulation study. *The Journal of Physical Chemistry B*, 111(11):2820–2827, 2007. ISSN 1520-6106.

[161] Ester Chiessi, Alice Lonardi, and Gaio Paradossi. Toward modeling thermoresponsive polymer networks: A molecular dynamics simulation study of n-isopropyl acrylamide co-oligomers. *The Journal of Physical Chemistry B*, 114(25):8301–8312, 2010. ISSN 1520-6106.

[162] Marc Behl, Muhammad Yasar Razzaq, and Andreas Lendlein. Multifunctional shape-memory polymers. *Advanced materials*, 22(31):3388–3410, 2010. ISSN 0935-9648.

[163] Andreas Lendlein and Steffen Kelch. Shape-memory polymers. *Angewandte Chemie International Edition*, 41(12):2034–2057, 2002. ISSN 1433-7851.

[164] Changdeng Liu, Haihu Qin, and PT Mather. Review of progress in shape-memory polymers. *Journal of materials chemistry*, 17(16):1543–1558, 2007.

[165] Aishwarya V Menon, Giridhar Madras, and Suryasarathi Bose. Shape memory polyurethane nanocomposites with porous architectures for enhanced microwave shielding. *Chemical Engineering Journal*, 352:590–600, 2018. ISSN 1385-8947.

[166] Zizheng Fang, Ning Zheng, Qian Zhao, and Tao Xie. Healable, reconfigurable, reprocessable thermoset shape memory polymer with highly tunable topological rear-

rangement kinetics. *ACS applied materials interfaces*, 9(27):22077–22082, 2017. ISSN 1944-8244.

[167] Clement Appiah, Christine Arndt, Katharina Siemsen, Anne Heitmann, Anne Staubitz, and Christine Selhuber-Unkel. Living materials herald a new era in soft robotics. *Advanced Materials*, 31(36):1807747, 2019. ISSN 0935-9648.

[168] Qiji Ze, Xiao Kuang, Shuai Wu, Janet Wong, S Macrae Montgomery, Rundong Zhang, Joshua M Kovitz, Fengyuan Yang, H Jerry Qi, and Ruike Zhao. Magnetic shape memory polymers with integrated multifunctional shape manipulation. *Advanced Materials*, 32(4):1906657, 2020. ISSN 0935-9648.

[169] Rui Xiao and Wei Min Huang. Heating/solvent responsive shape-memory polymers for implant biomedical devices in minimally invasive surgery: Current status and challenge. *Macromolecular bioscience*, 20(8):2000108, 2020. ISSN 1616-5187.

[170] Stefan Cichosz, Anna Masek, and Marian Zaborski. Polymer-based sensors: A review. *Polymer Testing*, 67:342–348, 2018. ISSN 0142-9418.

[171] Huan Gu, Sang Won Lee, Shelby Lois Buffington, James H Henderson, and Dacheng Ren. On-demand removal of bacterial biofilms via shape memory activation. *ACS applied materials interfaces*, 8(33):21140–21144, 2016. ISSN 1944-8244.

[172] Aarushi Bhargava, Kaiyuan Peng, Jerry Stieg, Reza Mirzaeifar, and Shima Shahab. Focused ultrasound actuation of shape memory polymers; acoustic-thermoelastic modeling and testing. *RSC advances*, 7(72):45452–45469, 2017.

[173] John G Hardy, Matteo Palma, Shalom J Wind, and Manus J Biggs. Responsive biomaterials: advances in materials based on shape-memory polymers. *Advanced Materials*, 28(27):5717–5724, 2016. ISSN 0935-9648.

[174] Alice Melocchi, Marco Uboldi, Nicoletta Inverardi, Francesco Briatico-Vangosa, Francesco Baldi, Stefano Pandini, Giulia Scalet, Ferdinando Auricchio, Matteo Cerea, and Anastasia Foppoli. Expandable drug delivery system for gastric retention based on shape memory polymers: Development via 4d printing and extrusion. *International journal of pharmaceutics*, 571:118700, 2019. ISSN 0378-5173.

[175] Witold Sokolowski, Annick Metcalfe, Shunichi Hayashi, and Jean Raymond. Medical applications of shape memory polymers. *Biomedical Materials*, 2(1):S23, 2007. ISSN 1748-605X.

[176] Tao Gong, Kun Zhao, Wenxi Wang, Hongmei Chen, Lin Wang, and Shaobing Zhou. Thermally activated reversible shape switch of polymer particles. *Journal of Materials Chemistry B*, 2(39):6855–6866, 2014.

[177] Wei Min Huang, Yuanze Zhao, Chang Chun Wang, Zhaoming Ding, Hendra Purnawali, Cheng Tang, and JL Zhang. Thermo/chemo-responsive shape memory effect in polymers: a sketch of working mechanisms, fundamentals and optimization. *Journal of Polymer Research*, 19(9):9952, 2012. ISSN 1022-9760.

[178] Haibao Lu, Wei Min Huang, Yong Qing Fu, and Jinsong Leng. Quantitative separation of the influence of hydrogen bonding of ethanol/water mixture on the shape recovery behavior of polyurethane shape memory polymer. *Smart materials and structures*, 23 (12):125041, 2014. ISSN 0964-1726.

[179] Mohadeseh Zare, Molamma P Prabhakaran, Nader Parvin, and Seeram Ramakrishna. Thermally-induced two-way shape memory polymers: Mechanisms, structures, and applications. *Chemical Engineering Journal*, 374:706–720, 2019. ISSN 1385-8947.

[180] Tong Zheng, Pei Xiaohan, Shen Zejun, Wei Songbo, Gao Yang, Peng HUANG, Shi Bairu, Sun Fuchao, and Fu Tao. An enhanced thermo-actuated shape memory polymer

composite coupled with elastomer. *Petroleum Exploration and Development*, 43(6): 1097–1106, 2016. ISSN 1876-3804.

[181] Jinghao Yang, Hao Wen, Haitao Zhuo, Shaojun Chen, and Jianfeng Ban. A new type of photo-thermo staged-responsive shape-memory polyurethanes network. *Polymers*, 9(7):287, 2017.

[182] Reza Mirzaeifar, Reginald DesRoches, and Arash Yavari. Analysis of the rate-dependent coupled thermo-mechanical response of shape memory alloy bars and wires in tension. *Continuum Mechanics and Thermodynamics*, 23(4):363–385, 2011. ISSN 0935-1175.

[183] Reza Mirzaeifar, Reginald DesRoches, Arash Yavari, and Ken Gall. On superelastic bending of shape memory alloy beams. *International Journal of Solids and Structures*, 50(10):1664–1680, 2013. ISSN 0020-7683.

[184] ZG Wei, R Sandstroröm, and S Miyazaki. Shape-memory materials and hybrid composites for smart systems: Part i shape-memory materials. *Journal of materials science*, 33(15):3743–3762, 1998. ISSN 0022-2461.

[185] Ken Gall, Christopher M Yakacki, Yiping Liu, Robin Shandas, Nick Willett, and Kristi S Anseth. Thermomechanics of the shape memory effect in polymers for biomedical applications. *Journal of Biomedical Materials Research Part A: An Official Journal of The Society for Biomaterials, The Japanese Society for Biomaterials, and The Australian Society for Biomaterials and the Korean Society for Biomaterials*, 73(3): 339–348, 2005. ISSN 1549-3296.

[186] Christopher Michael Yakacki, Robin Shandas, Craig Lanning, Bryan Rech, Alex Eckstein, and Ken Gall. Unconstrained recovery characterization of shape-memory poly-

mer networks for cardiovascular applications. *Biomaterials*, 28(14):2255–2263, 2007. ISSN 0142-9612.

[187] Andreas Lendlein, Marc Behl, Bernhard Hiebl, and Christian Wischke. Shape-memory polymers as a technology platform for biomedical applications. *Expert review of medical devices*, 7(3):357–379, 2010. ISSN 1743-4440.

[188] Yiqi Mao, Kai Yu, Michael S Isakov, Jiangtao Wu, Martin L Dunn, and H Jerry Qi. Sequential self-folding structures by 3d printed digital shape memory polymers. *Scientific reports*, 5:13616, 2015. ISSN 2045-2322.

[189] Jiangtao Wu, Chao Yuan, Zhen Ding, Michael Isakov, Yiqi Mao, Tiejun Wang, Martin L Dunn, and H Jerry Qi. Multi-shape active composites by 3d printing of digital shape memory polymers. *Scientific reports*, 6:24224, 2016. ISSN 2045-2322.

[190] Matt Zarek, Michael Layani, Ido Cooperstein, Ela Sachyani, Daniel Cohn, and Shlomo Magdassi. 3d printing of shape memory polymers for flexible electronic devices. *Advanced Materials*, 28(22):4449–4454, 2016. ISSN 0935-9648.

[191] Yu Ying Clarrisa Choong, Saeed Maleksaeedi, Hengky Eng, Jun Wei, and Pei-Chen Su. 4d printing of high performance shape memory polymer using stereolithography. *Materials Design*, 126:219–225, 2017. ISSN 0264-1275.

[192] Hongzhi Wu, Peng Chen, Chunze Yan, Chao Cai, and Yusheng Shi. Four-dimensional printing of a novel acrylate-based shape memory polymer using digital light processing. *Materials Design*, 171:107704, 2019. ISSN 0264-1275.

[193] G Jerald Maria Antony, S Raja, ST Aruna, and Chetan S Jarali. Effect of the addition of diurethane dimethacrylate on the chemical and mechanical properties of tba-pegdma

acrylate based shape memory polymer network. *Journal of the Mechanical Behavior of Biomedical Materials*, 110:103951, 2020. ISSN 1751-6161.

[194] A Bhargava, K Peng, and S Shahab. Dynamics of focused ultrasound actuated shape memory polymers. In *Active and Passive Smart Structures and Integrated Systems XIII*, volume 10967, page 1096720. International Society for Optics and Photonics, .

[195] Aarushi Bhargava. *Dynamics of smart materials in high intensity focused ultrasound field*. Thesis, 2020.

[196] Aarushi Bhargava, Kaiyuan Peng, Reza Mirzaeifar, and Shima Shahab. Ultrasound actuated shape-memory polymer based drug delivery containers. In *Active and Passive Smart Structures and Integrated Systems XII*, volume 10595, page 105952H. International Society for Optics and Photonics, .

[197] L Sun, WM Huang, CC Wang, Y Zhao, Z Ding, and H Purnawali. Optimization of the shape memory effect in shape memory polymers. *Journal of Polymer Science Part A: Polymer Chemistry*, 49(16):3574–3581, 2011. ISSN 0887-624X.

[198] Li Sun and Wei Min Huang. Mechanisms of the multi-shape memory effect and temperature memory effect in shape memory polymers. *Soft Matter*, 6(18):4403–4406, 2010.

[199] Kaiyuan Peng, Shima Shahab, and Reza Mirzaeifar. Interaction of high-intensity focused ultrasound with polymers at the atomistic scale. *Nanotechnology*, 32(4):045707, 2020. ISSN 0957-4484.

[200] Steve Plimpton. Fast parallel algorithms for short-range molecular dynamics. *Journal of computational physics*, 117(1):1–19, 1995. ISSN 0021-9991.

[201] Andrew Jewett. Moltemplate manual. *University of California, Santa Barbara Shea Lab (August 2015)*, 2020.

[202] Andrew I Jewett, Zhuoyun Zhuang, and Joan-Emma Shea. Moltemplate a coarse-grained model assembly tool. *Biophysical Journal*, 104(2):169a, 2013. ISSN 0006-3495.

[203] José Mario Martínez and Leandro Martínez. Packing optimization for automated generation of complex system's initial configurations for molecular dynamics and docking. *Journal of computational chemistry*, 24(7):819–825, 2003. ISSN 0192-8651.

[204] Leandro Martínez, Ricardo Andrade, Ernesto G Birgin, and José Mario Martínez. Packmol: a package for building initial configurations for molecular dynamics simulations. *Journal of computational chemistry*, 30(13):2157–2164, 2009. ISSN 0192-8651.

[205] Alexander Stukowski. Visualization and analysis of atomistic simulation data with ovito–the open visualization tool. *Modelling and Simulation in Materials Science and Engineering*, 18(1):015012, 2009. ISSN 0965-0393.

[206] Xue Lian Wu, Wei Min Huang, Hai Bao Lu, Chang Chun Wang, and Hai Po Cui. Characterization of polymeric shape memory materials. *Journal of Polymer Engineering*, 37(1):1–20, 2017. ISSN 0334-6447.

[207] VA Beloshenko, Ya E Beigel'zimer, VN Varyukhin, and Yu V Voznyak. Strain hysteresis of polymers. In *Doklady Physical Chemistry*, volume 409, pages 207–209. Nauka/Interperiodica. ISBN 0012-5016.

[208] Jan W. Gooch. *Tensile Hysteresis Curve*, pages 733–733. Springer New York, New York, NY, 2011. ISBN 978-1-4419-6247-8. doi: 10.1007/978-1-4419-6247-8_11623. URL https://doi.org/10.1007/978-1-4419-6247-8_11623.

[209] Pnina Dauber-Osguthorpe, Victoria A Roberts, David J Osguthorpe, Jon Wolff, Moniqe Genest, and Arnold T Hagler. Structure and energetics of ligand binding to proteins: Escherichia coli dihydrofolate reductase-trimethoprim, a drug-receptor system. *Proteins: Structure, Function, and Bioinformatics*, 4(1):31–47, 1988. ISSN 0887-3585.

[210] Pinar Boyraz, Gundula Runge, and Annika Raatz. An overview of novel actuators for soft robotics. *Actuators*, 7(3), 2018. ISSN 2076-0825. doi: 10.3390/act7030048.

[211] Nazek El-Atab, Rishabh B. Mishra, Fhad Al-Modaf, Lana Joharji, Aljohara A. Alsharif, Haneen Alamoudi, Marlon Diaz, Nadeem Qaiser, and Muhammad Mustafa Hussain. Soft actuators for soft robotic applications: A review. *Advanced Intelligent Systems*, n/a(n/a):2000128, 2020. ISSN 2640-4567. doi: 10.1002/aisy.202000128. URL https://doi.org/10.1002/aisy.202000128.

[212] E. Acome, S. K. Mitchell, T. G. Morrissey, M. B. Emmett, C. Benjamin, M. King, M. Radakovitz, and C. Keplinger. Hydraulically amplified self-healing electrostatic actuators with muscle-like performance. *Science*, 359(6371):61, 2018. doi: 10.1126/science.aao6139. URL http://science.sciencemag.org/content/359/6371/61.abstract.

[213] Yichao Tang, Qiuting Zhang, Gaojian Lin, and Jie Yin. Switchable adhesion actuator for amphibious climbing soft robot. *Soft Robotics*, 5(5):592–600, 2018. ISSN 2169-5172. doi: 10.1089/soro.2017.0133. URL https://doi.org/10.1089/soro.2017.0133.

[214] Yichao Tang, Yinding Chi, Jiefeng Sun, Tzu-Hao Huang, Omid H. Maghsoudi, Andrew Spence, Jianguo Zhao, Hao Su, and Jie Yin. Leveraging elastic instabilities for amplified performance: Spine-inspired high-speed and high-force soft robots. *Sci-*

ence Advances, 6(19):eaaz6912, 2020. doi: 10.1126/sciadv.aaz6912. URL http://advances.sciencemag.org/content/6/19/eaaz6912.abstract.

[215] Hamed Shahsavan, Amirreza Aghakhani, Hao Zeng, Yubing Guo, Zoey S. Davidson, Arri Priimagi, and Metin Sitti. Bioinspired underwater locomotion of light-driven liquid crystal gels. *Proceedings of the National Academy of Sciences*, 117(10):5125, 2020. doi: 10.1073/pnas.1917952117. URL http://www.pnas.org/content/117/10/5125.abstract.

[216] Shu-ting Xing, Ping-ping Wang, Shu-qi Liu, Yong-hang Xu, Rong-min Zheng, Zhi-fu Deng, Ze-fei Peng, Jun-yun Li, Yao-yi Wu, and Lan Liu. A shape-memory soft actuator integrated with reversible electric/moisture actuating and strain sensing. *Composites Science and Technology*, 193:108133, 2020. ISSN 0266-3538. doi: https://doi.org/10.1016/j.compscitech.2020.108133. URL http://www.sciencedirect.com/science/article/pii/S026635381933372X.

[217] Tae-Hyung Kang, Jeong-Min Lee, Woong-Ryeol Yu, Ji Ho Youk, and Hee Wook Ryu. Two-way actuation behavior of shape memory polymer/elastomer core/shell composites. *Smart Materials and Structures*, 21(3):035028, 2012. ISSN 0964-1726 1361-665X. doi: 10.1088/0964-1726/21/3/035028. URL http://dx.doi.org/10.1088/0964-1726/21/3/035028.

[218] Taylor H. Ware, Michael E. McConney, Jeong Jae Wie, Vincent P. Tondiglia, and Timothy J. White. Voxelated liquid crystal elastomers. *Science*, 347(6225):982, 2015. doi: 10.1126/science.1261019. URL http://science.sciencemag.org/content/347/6225/982.abstract.

[219] Donald L. Thomsen, Patrick Keller, Jawad Naciri, Roger Pink, Hong Jeon, Devanand Shenoy, and Banahalli R. Ratna. Liquid crystal elastomers with mechanical properties

of a muscle. *Macromolecules*, 34(17):5868–5875, 2001. ISSN 0024-9297. doi: 10.1021/ma001639q. URL https://doi.org/10.1021/ma001639q.

[220] N. Z. Tomić, B. I. Međo, D. B. Stojanović, V. J. Radojević, M. P. Rakin, R. M. Jančić-Heinemann, and R. R. Aleksić. A rapid test to measure adhesion between optical fibers and ethylene–vinyl acetate copolymer (eva). *International Journal of Adhesion and Adhesives*, 68:341–350, 2016. ISSN 0143-7496. doi: https://doi.org/10.1016/j.ijadhadh.2016.04.012. URL http://www.sciencedirect.com/science/article/pii/S0143749616300872.

[221] Azlin Fazlina Osman, Asna Rasyidah Abdul Hamid, Tuty Fareyhynn Mohammed Fitri, Asfa Amalia Ahmad Fauzi, and Khairul Anwar Abdul Halim. Poly(ethylene-co-vinylacetate) copolymer based nanocomposites: A review. *IOP Conference Series: Materials Science and Engineering*, 864:012121, 2020. ISSN 1757-899X. doi: 10.1088/1757-899x/864/1/012121. URL http://dx.doi.org/10.1088/1757-899X/864/1/012121.

[222] Marc Behl, Karl Kratz, Ulrich Noechel, Tilman Sauter, and Andreas Lendlein. Temperature-memory polymer actuators. *Proceedings of the National Academy of Sciences*, 110(31):12555, 2013. doi: 10.1073/pnas.1301895110. URL http://www.pnas.org/content/110/31/12555.abstract.

[223] Yue Liu, Muhammad Yasar Razzaq, Tobias Rudolph, Liang Fang, Karl Kratz, and Andreas Lendlein. Two-level shape changes of polymeric microcuboids prepared from crystallizable copolymer networks. *Macromolecules*, 50(6):2518–2527, 2017. ISSN 0024-9297. doi: 10.1021/acs.macromol.6b02237. URL https://doi.org/10.1021/acs.macromol.6b02237.

[224] Qianxi Yang, Jizhou Fan, and Guoqiang Li. Artificial muscles made of chiral two-way

shape memory polymer fibers. *Applied Physics Letters*, 109(18):183701, 2016. ISSN 0003-6951. doi: 10.1063/1.4966231. URL https://doi.org/10.1063/1.4966231.

[225] Jin Hui, Hong Xia, Yaqin Fu, Yiping Qiu, and Qing-Qing Ni. Two-way reversible shape memory properties of benzoyl peroxide crosslinked poly(ethylene-co-vinyl acetate) under different stress conditions. *Macromolecular Materials and Engineering*, 305(4):1900825, 2020. ISSN 1438-7492. doi: 10.1002/mame.201900825. URL https://doi.org/10.1002/mame.201900825.

[226] Yuan Gao, Weifeng Liu, and Shiping Zhu. Reversible shape memory polymer from semicrystalline poly(ethylene-co-vinyl acetate) with dynamic covalent polymer networks. *Macromolecules*, 51(21):8956–8963, 2018. ISSN 0024-9297. doi: 10.1021/acs.macromol.8b01724. URL https://doi.org/10.1021/acs.macromol.8b01724.

[227] Ke Wang and Qibo Deng. The thermal and mechanical properties of poly(ethylene-co-vinyl acetate) random copolymers (peva) and its covalently crosslinked analogues (cpeva). *Polymers*, 11(6):1055, 2019. ISSN 2073-4360. doi: 10.3390/polym11061055. URL https://pubmed.ncbi.nlm.nih.gov/31212957https://www.ncbi.nlm.nih.gov/pmc/articles/PMC6631310/.

[228] H. Ghasemi, N. Thoppey, Huang Xiaopeng, J. Loomis, Li Xiaobo, J. Tong, Wang Jianjian, and G. Chen. High thermal conductivity ultra-high molecular weight polyethylene (uhmwpe) films. In *Fourteenth Intersociety Conference on Thermal and Thermomechanical Phenomena in Electronic Systems (ITherm)*, pages 235–239. ISBN 1087-9870. doi: 10.1109/ITHERM.2014.6892287.

[229] Yao Zhao, Haoqi Li, Zhuolei Zhang, Jacob Celli, Simona Percec, and Fei Ren. Nanoindentation study of time-dependent mechanical properties of ultra-high-molecular-weight polyethylene (uhmwpe) at different temperatures. *Polymer Testing*, 91:106787,

2020. ISSN 0142-9418. doi: https://doi.org/10.1016/j.polymertesting.2020.106787. URL http://www.sciencedirect.com/science/article/pii/S0142941820316603.

[230] Arda Kotikian, Connor McMahan, Emily C. Davidson, Jalilah M. Muhammad, Robert D. Weeks, Chiara Daraio, and Jennifer A. Lewis. Untethered soft robotic matter with passive control of shape morphing and propulsion. *Science Robotics*, 4(33):eaax7044, 2019. doi: 10.1126/scirobotics.aax7044. URL http://robotics.sciencemag.org/content/4/33/eaax7044.abstract.

[231] Aarushi Bhargava, Kaiyuan Peng, Jerry Stieg, Reza Mirzaeifar, and Shima Shahab. Focused ultrasound actuation of shape memory polymers; acoustic-thermoelastic modeling and testing. *RSC Advances*, 7(72):45452–45469, 2017. doi: 10.1039/C7RA07396H. URL http://dx.doi.org/10.1039/C7RA07396H.

[232] Kurt Kremer and Gary S Grest. Dynamics of entangled linear polymer melts: A molecular-dynamics simulation. *The Journal of Chemical Physics*, 92(8):5057–5086, 1990.

[233] David D Hsu, Wenjie Xia, Steven G Arturo, and Sinan Keten. Thermomechanically consistent and temperature transferable coarse-graining of atactic polystyrene. *Macromolecules*, 48(9):3057–3068, 2015.